Phase formation processes in the synthesis of boron nitride thin films

Dissertation

zur Erlangung des Doktorgrades
der Mathematisch-Naturwissenschaftlichen Fakultäten
der Georg-August-Universität zu Göttingen

Vorgelegt von
Sören Eyhusen
aus Karlsruhe

Göttingen 2005

D 7

Referent: Prof. Dr. Hans C. Hofsäß

Korreferent: PD Dr. Christian Jooß

Tag der mündlichen Prüfung: 27.10.2005

Contents

Abstract

Research on cubic boron nitride (c-BN) has made tremendous progress over the last decade. Nowadays, both c-BN single crystals and thin films can be rountinely synthesized by means of high pressure high temperature (HPHT) and physical vapor deposition (PVD) techniques, respectively. However, the deposited thin films usually exhibit a rather high defect density such as grain boundaries, dislocations, stacking faults, and impurities. Moreover, thin films of cubic boron nitride most often suffer from a high compressive stress, which causes the film to disintegrate and dilaminate from the substrate at thicknesses exceeding a few hundred nanometer. Much effort has been devoted to the problem of minimizing the compressive stress and to the development of appropriate low-pressure synthesis methods that are able to produce sufficiently thick, adherent, and stress-free films.

Many deposition techniques have been applied to grow c-BN thin films, but it turned out that ion bombardment is absolutely necessary to form the cubic phase. All attempts to grow c-BN directly from the gas phase have failed so far. Hence, c-BN growth takes place far from thermodynamic equilibrium, and the influence of the ion bombardment is subject of active research, however, a satisfactory explanation of the fundamental mechanisms involved is still lacking.

Among the deposition techniques applied, mass separated ion beam deposition (MSIBD) is a very attractive approach for the synthesis of c-BN films. This method offers the advantage of being able to grow isotopically pure films under UHV conditions exhibiting a high cubic phase content and a very low impurity concentration. Furthermore, as only singly charged $^{11}B^+$ and $^{14}N^+$ ions are involved in the deposition process, the ion energy can be precisely adjusted and is thus well-defined. MSIBD is therefore particularly well suited to investigate the influence of the ion bombardment on the nucleation, growth, and microstructure of c-BN films.

In chapter 1, cubic boron nitride will be introduced as a superhard, diamond-like material and its outstanding physical properties will be discussed and compared to other materials present in the B-C-N triangle. A brief overview of the available synthesis techniques will be given. Thin films of c-BN are usually nano-crystalline and embedded between to sp^2-bonded BN layers. This rather complex film structure is a consequence of many parameters involved in the deposition process, and the influence of these parameters will be described.

Chapter 2 gives an overview of the experimental methods and characterization techniques that have been used in this work. The mass separated ion beam deposition (MSIBD) system "ADONIS" is described by placing special emphasis on its application for c-BN film growth.

In chapter 3, the influence of the ion energy on c-BN formation is investigated and discussed. It turns out that c-BN growth can be maintained with ion energies of at least 43 keV, however, the substrate temperature has been found to have a major influence on BN phase formation at ion energies exceeding about 5 keV. Previously, it has been assumed that c-BN growth should be relatively temperature-independent, not at least due to the high energy density transferred to the growing film by the ion bombardment. The experiments presented in this section reveal a characteristic energy-dependent temperature threshold, below which c-BN growth reverts back to sp^2-bonded BN growth.

The most prevalent models developed for and applied to c-BN nucleation and growth will be discussed in chapter 4. It will be shown that none of the existing models is able to give an explanation for the observed energy-dependent temperature threshold for c-BN growth with high ion energies. Therefore, a model based on temperature-driven diffusion processes is proposed as being responsible for a suppression of defect accumulation, which is regarded as being crucial for maintaining cubic phase formation. With the assumption of an Arrhenius diffusion behavior and a combination of SIMS data and SRIM simulations, the critical temperatures below which c-BN growth cannot be maintained were calculated as a function of ion energy. Furthermore, a diffusion constant and migration energy for interstitial

boron diffusion in c-BN have been estimated. The model has been applied to both c-BN growth and nucleation, and its predictions are shown to be in good agreement with the experimental results.

Chapter 5 presents the results obtained during ion irradiation of c-BN films. It will be shown that c-BN is extremely stable against ion bombardment as long as the t-BN/c-BN interface is not irradiated. Cubic BN films are able to withstand irradiation with approximately 1×10^{16} Ar and 1×10^{17} N ions/cm^2, respectively. These fluences generate a defect concentration of about 8 and 20 displacements per atom (dpa), respectively. A substantial release of compressive stress is observed upon ion bombardment, which, however, is accompanied by a significant decrease of grain size and overall crystal quality. On the other hand, if the bombarding ions are able to penetrate the c-BN layer and irradiate the t-BN/c-BN interface, a complete transformation of the cubic phase into sp^2-bonded material can be induced by irradiating the film with an ion fluence that generates an accumulated defect concentration of about 1 dpa.

Chapter 1

Introduction

1.1 Cubic boron nitride: properties and applications

Cubic boron nitride (c-BN) was first produced in 1957 by Robert H. Wentorf, a physical chemicist for the General Electric Company [Wen57], just two years after the first artificial diamonds were synthesized [Bun55]. In analogy to the fabrication of diamond crystals, c-BN was produced from hexagonal boron nitride under high-pressure and high-temperature (HPHT) conditions. It is not only the synthesis process that is similar for c-BN and diamond: c-BN is sometimes referred to as "the better diamond", which is mainly related to the fact that both materials share many extreme properties, but c-BN is superior to diamond in some cases (see table 1.1 for a comparison of selected properties of single-crystalline diamond and c-BN). After diamond, it is one of the hardest materials known, with roughly 50-70 GPa Vickers hardness vs. 70+ GPa for diamond. However, c-BN exhibits a much better chemical inertness and thermal stability. Diamond readily reacts with iron, cobalt, and nickel at temperatures above 1000 °C or is subject to oxidation at $T > 800$ °C, which results into a disintegration of the diamond surface into gaseous CO_2. In contrast, c-BN is chemically inert against iron group metals for temperatures of up to 1800 °C [Vel91], and its high stability against oxidation is a consequence of the formation of liquid or solid B_2O_3, which protects the surface against further oxidation [Bar96]. Thus, c-BN is a promising material for corrosion- and wear-resistant coatings for machinery and cutting tools, particularly in those cases where the reactivity of diamond makes this unsuitable.

	diamond	**c-BN**
lattice constant [nm]	0.3567	0.3615
bond length [nm]	0.1545	0.1565
atomic density [nm^{-3}]	176	170
mass density [$\mathrm{g/cm}^3$]	3.51	3.48
Vickers hardness [GPa]	80-100	50-70
Debye temperature at RT [K]	1860	1700
sound velocity [10^4 m/s]	1.1-1.8	1.5
thermal conductivity at RT [W/cm/K]	20-22	2-13
thermal expansion coefficient [$10^{-6}\ \mathrm{K}^{-1}$]	0.8	4.8
band gap [eV]	5.45	6.4

Table 1.1: Comparison of selected physical properties of single-crystalline diamond and c-BN (taken from refs. [Hof96, Fel02]).

Cubic boron nitride also has the potential to outclass diamond in view of electronic applications. It not only has a high band-gap ($E_g = 6.4$ eV) and the second highest room temperature thermal conductivity after diamond (2-13 W/cm/K), but, in contrast to diamond, it can be easily doped to obtain both n- and p-type conductivities [Wen62, Mis90]. By exploiting this feature, Mishima and co-workers were able to construct a high-temperature p-n junction rectifying diode [Mis87] as well as an ultraviolet light-emitting p-n junction diode [Mis88] based on c-BN HPHT bulk material. However, large scale industrial applications are still not possible, mainly because the c-BN crystals exhibit a rather high defect density and impurity concentration.

The interest in c-BN has increased tremendously since the late 1980's, which is mainly related to the fact that c-BN thin films can be routinely synthesized by means of ion beam assisted deposition methods as of then. The deposition of c-BN films by a large variety of physical and chemical vapor deposition techniques has been extensively studied, and it turned out that ion bombardment is imperative to form the cubic phase. All attempts to grow c-BN by chemical processes alone have failed so far. Thus, it is generally accepted that ion bombardment plays a major role in the formation of cubic BN. Models trying to explain the influence of the ion beam on c-BN growth were developed, but a satisfactory understanding of the mechanisms leading to c-BN formation is still lacking. This is due to the rather complex film structure, which consists of a characteristic layer sequence of hexagonal and cubic phases [Mir97a]: cubic BN is usually never in direct contact with the substrate, but is preceded by a thin layer of sp^2-bonded BN. Only very recently has heteroepitaxial growth of c-BN on specific substrate materials and under certain deposition conditions been achieved [Fel01, Zha03]. As epitaxial growth has proven to be very difficult, the synthesis of phase-pure, highly-crystalline c-BN films has not been accomplished so far. Consequently, the electronic and optical properties of c-BN films are not well investigated.

The deposited c-BN films are usually nanocrystalline and exhibit a large ion-bombardment-induced compressive stress of up to 25 GPa [McK93], which causes the destruction of the film due to delamination at thicknesses above a few hundred nanometer. Much effort has been devoted to the problem of minimizing intrinsic stress, as the limit in film thickness is a serious problem in view of tribologic applications. Nevertheless, c-BN films have already been successfully applied as passivation, insulating and low-dielectric-constant layers in microelectronic devices and as corrision-resistant coatings for x-ray lithography masks [Cot95, Sta99]. Moreover, cutting tools and abrasive components particularly for use with low carbon ferrous metals have been developed using c-BN. In this application the tools behave in a similar manner to polycrystalline diamond tools but can be used on iron and low carbon alloys without risk of reaction. Cubic boron nitride is also used for substrates for mounting high density and high power electronic components where the high thermal conductivity achieved allows efficient heat dissipation. Although enormous progress has been achieved over the last years, a better understanding of the fundamental mechanisms leading to c-BN formation is still needed in order to develop appropriate low-pressure deposition procedures that are able to prepare sufficiently thick, adherent, and stress-free films.

Cubic boron nitride is often classified into the group of superhard diamond-like materials. By definition, *superhard* means materials whose Vickers hardness H_V exceeds 40 GPa [Vep99]. The Vickers technique is used very often when characterizing hard materials; in principle, the indentation left by a diamond stylus is

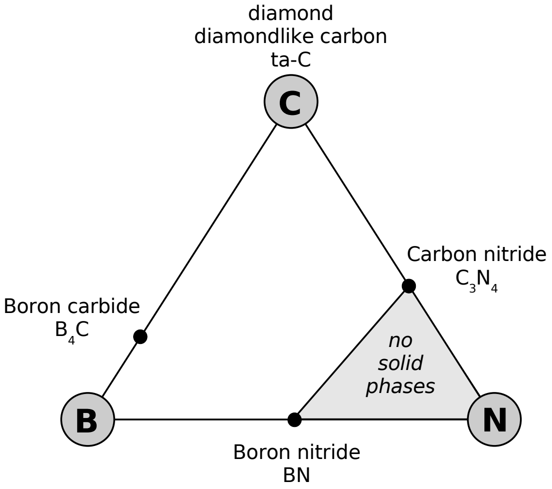

Figure 1.1: B-C-N ternary phase diagram with some diamond-like materials (after ref. [Hof96]).

measured and the hardness is then given by the ratio of applied load to the impression left by the indenter. Superhard materials can be divided into intrinsic (such as c-BN or diamond) and extrinsic (materials based on superlattices or nanocomposite materials). Intrinsically superhard materials derive their hardness solely from their atomic scale characteristics, i.e. small atomic sizes with fourfold covalent bonds and short, strong bond lengths; whereas, extrinsically superhard materials minimize plastic deformation by preventing the main mechanisms involved, i.e. the movement and multiplication of dislocations and the growth of microcracks [Her95].

The only known intrinsically superhard materials are diamond ($V_H = 70-100$ GPa), c-BN ($V_H \approx 60$ GPa), and tetrahedral amorphous carbon (ta-C) films ($V_H \geq 40$ GPa). In addition, Solozhenko *et al.* very recently claimed to have synthesized cubic BC_2N with a Vickers hardness of 76 GPa [Sol00], which is even larger than that of c-BN. This already shows a systematic concept: all intrinsically superhard materials consist of either carbon, boron, and/or nitrogen (see figure 1.1). Only those elements can form a three-dimensional arrangement of directional bonds due to their valancy or oxidation state, and, furthermore, they form mostly covalent bonds and exhibit a high bond energy due to a high electron density between the atoms. This observation has led Cohen [Coh85] and co-workers [Liu89, Coh94, Coh96] to the formulation of a semi-empirical formula for the bulk modulus B [GPa] of purely covalent and partially covalent/ionic compounds formed from elements near the center of the periodic table:

$$B = \frac{N_C}{4}(1971 - 220\lambda)a_0^{-3.5}, \tag{1.1}$$

where N_C is the average coordination number, a_0 is the bond length in Å, and λ is a parameter describing the ionicity of the chemical bonds ($0 < \lambda < 2$, $\lambda = 0$ for a covalent bond, $\lambda = 1$ for the covalent/ionic bond in c-BN). Hence, a high bulk modulus B requires the material to consist of atoms with a high coordination number N_C, which should be covalently bonded ($\lambda = 0$) and exhibit short bond lengths a_0. It is thus not surprising that the hardest known intrinsically superhard materials can be found in the vicinity of carbon in the periodic system.

In 1985, based on this concept and Cohen's formula, Cohen and Liu theorised that carbon and nitrogen atoms could form a particularly short and strong bond in a stable lattice in a ratio of 1:1.3 (β-C_3N_4) [Coh85]. That this material would be harder than diamond was first proposed in 1989 [Liu89]. However, despite a tremendous world-wide effort, the reproducible synthesis of single-crystalline β-C_3N_4 has not been achieved [Ron98, Vep99]. This is probably related to the fact that its preparation is extremely difficult, especially the synthesis of stoichiometric films has proven to be very challenging. Energetic ion bombardment during the growth is seen to be necessary to promote the carbon into the metastable fourfold coordination (sp^3 hybrid), but it has also led to the loss of nitrogen from the films in many experiments carried out so far [Vep99]. Apart from the technical difficulties in preparing high-quality β-C_3N_4 films, the Vickers hardness reported for stoichiometric amorphous films reached only about 30 GPa, which is much less than that of diamond or other superhard materials. In addition, the predicted shear modulus for β-C_3N_4 is only 60% of that of diamond. In view of the fact that the shear modulus has been shown to be a better atomistic predictor of hardness than bulk modulus for a wide variety of materials [Tet98, Heb00], β-C_3N_4 will probably not even reach the hardness of diamond or c-BN.

Although the B-C-N system offers a large variety of hard and superhard materials, most of them are only metastable under ambient conditions. In addition, with the exception of diamond, they can only be synthesized under HPHT or highly non-equilibrium conditions, i.e. by using ion bombardment, and within a narrow window of process parameters.

1.2 BN phase system

1.2.1 BN crystal structures

Analogous to carbon, boron nitride forms both hard, diamond-like sp^3-bonded phases and softer, graphite-like sp^2-bonded phases. In contrast to the carbon phases, which can be found in nature, all BN modifications are only synthetic materials. Cubic boron nitride (c-BN) crystallizes like diamond in a zinc-blende structure, in which the atoms are bonded to four nearest neighbors of the alternate species through sp^3-hybridization in a three-dimensional tetrahedral framework. The {111} planes consist of corrugated six-membered rings of alternating B and N atoms, and are arranged in a three-layer (ABCABC...) stacking sequence (see figure 1.2d). Hexagonal boron nitride (h-BN) is a layered structure that is similar to graphite with the exception that hexagonal rings of the basal planes in h-BN are positioned directly above each other and rotated by 180° between alternate

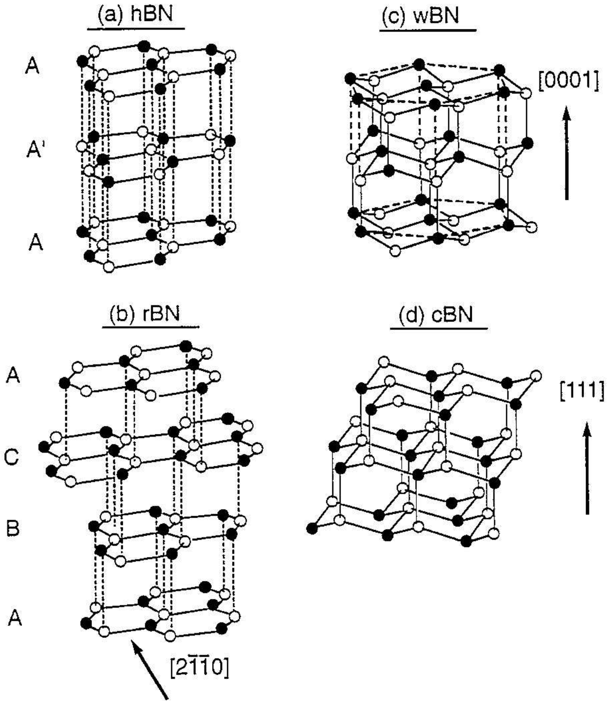

Figure 1.2: Structures of the sp^3-bonded phases c-BN and w-BN and the sp^2-bonded phases h-BN and r-BN with respective stacking sequences (taken from [Mir97a]).

layers (figure 1.2a). The two-layer (0002) stacking sequence for h-BN can thus be described as (AA'AA'...).

A change of the stacking sequence for both the sp^2- and sp^3-bonded phases produces additional sp^2- and sp^3-bonded polytypes. Rhombohedral BN (r-BN) is structurally identical to rhombohedral graphite, i.e. all layers are oriented in the same rotational sense but are successively displaced relative to each other by a vector of a/3 in $<01\bar{1}0>$ direction. This results in the (ABCABC...) layer sequence displayed in figure 1.2b. Similarly, the stacking sequence of wurtzite boron nitride (w-BN) corresponds to that of Lonsdaleite, i.e. hexagonal diamond. Wurtzite BN consists of a two-layer (AA'AA'...) stacking of the (0002) planes, which are structurally identical to the $\{111\}$ planes of the c-BN structure (figure 1.2c).

In h-BN and r-BN, the atoms within the basal planes are bonded to three nearest neighbors through strong in-plane sp^2-hybridization, but the hexagonal planes are bonded to each other through weak van der Waals interaction only. This bonding anisotropy leads to different physical properties depending on the crystal direction. For example, the compressibility is much higher along the c-axis than along the a-axis. Both BN polymorphs exhibit a density comparable to graphite ($\rho_{h-BN} =$ 2.25 g/cm^3, $\rho_{gra} = 2.26$ g/cm^3, see also table 1.2), and they generally share many properties with graphite. In fact, h-BN is sometimes referred to as "white graphite", which accounts for both the similarities and differences between these two materials: graphite is a soft, black, and conducting material whereas h-BN is soft, white, and insulating. This discrepancy in electrical properties is a consequence of the partly ionic bond in h-BN that is caused by the greater electronegativity of nitrogen as compared to boron. The distribution of the relatively weakly bounded π-electrons (between the basal planes) is strongly perturbed, with a 0.5:1.5 division of the π charge between B and N [Teg79]. This induces a division of the π-electron band into two sub-bands separated by an energy gap of 4-5 eV.

In c-BN and w-BN, on the other hand, the atoms are bonded to four nearest neighbors of the alternating species through sp^3-hybridization. This results in a very short bond length, which, together with the small atomic size, leads to a high mass density ($\rho_{c-BN} = 3.48$ g/cm^3) and hardness that are comparable to those of diamond (see table 1.2). Similar to the h-BN case, the heteropolar effect in c-BN splits

	cubic phases		*hexagonal phases*	
	c-BN	diamond	h-BN	graphite
lattice constant	a=3.62 Å	a=3.51 Å	a=2.50 Å c=6.66 Å	a=2.46 Å c=6.70 Å
bond length	a=1.57 Å	a=1.54 Å	a=1.45 Å c=3.30 Å	a=1.42 Å c=3.35 Å
hybridization	sp^3	sp^3	sp^2	sp^2
band gap	6.4 eV	5.45 eV	~ 5 eV	-0.04 eV
mass density	3.48 g/cm^2	3.51 g/cm^2	2.25 g/cm^2	2.26 g/cm^2

Table 1.2: Comparison of the properties of the crystalline modifications of carbon and boron nitride (Data has been taken from refs. [Chr74, Mad91, Vel91, Hof96]).

the valence band into two sub-bands separated by a band gap of 6.4 eV [Chr74], which is larger than the 5.45 eV found for diamond.

1.2.2 Equilibrium (p,T) phase diagram

Up to date, the only technique available to produce c-BN under equilibrium conditions is the High Pressure–High Temperature (HPHT) synthesis. The use of HPHT methods to establish a phase diagram for boron nitride has proven to be difficult because of several reasons: First, the experimentally accessible (p,T) values are restricted to a narrow region characteristic for each individual experimental setup. The respective h-BN/c-BN equilibrium line then has to be extrapolated based on previous experimental results or on thermodynamical calculations. Second, the c-BN to h-BN transformation (and vice-versa) depends strongly on parameters like grain size, defect concentration, and purity of the starting material [Wil00]. Therefore, the equilibrium (p,T) phase diagram for boron nitride, especially the equilibrium line between h-BN and c-BN, are controversially discussed in the literature.

Immediately after the first successful synthesis of c-BN in 1957 by Wentorf [Wen57], attempts to establish a pressure-temperature phase diagram for boron nitride were initiated. A first version of a (p,T) phase diagram was introduced by Bundy and

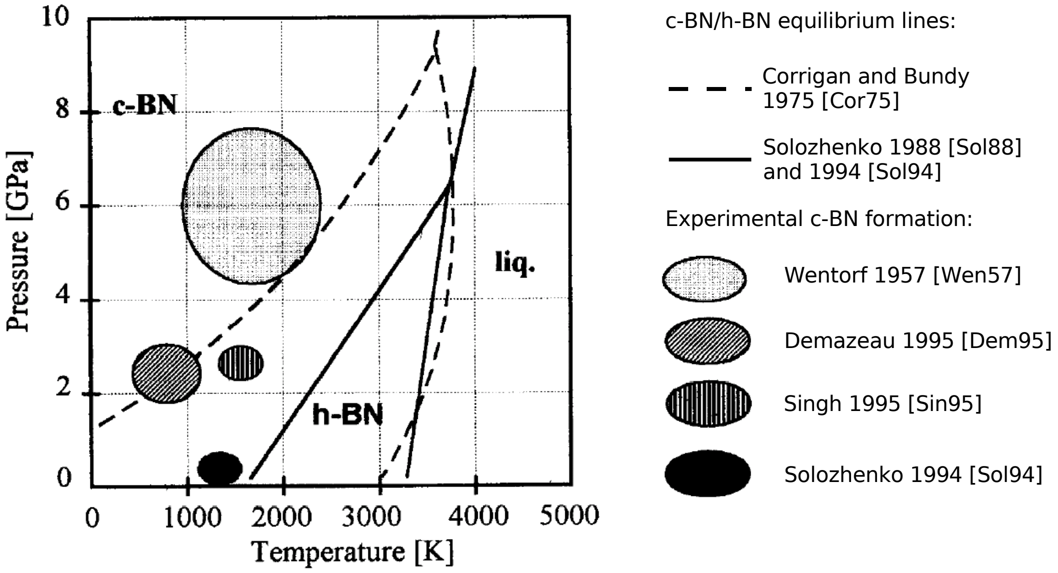

Figure 1.3: Equilibrium (p,T) phase diagram of boron nitride showing the equilibrium lines as proposed by Corrigan and Bundy [Cor75] and more recently by Solozhenko [Sol88, Sol93, Sol94]. Additionally some experimentally observed regions for c-BN formation are displayed. This compilation was taken from ref. [Bar96].

Wentorf in 1963 [Bun63] based on Wentorf's experimental data on conversion of graphite-like hexagonal BN into the cubic form [Wen57, Wen61a, Wen61b] and data on h-BN melting under high pressures [Wen59]. Interestingly, cubic BN was found to be the stable phase at ambient conditions, which, however, was changed a few years later in an ensuing publication. In 1975, Corrigan and Bundy [Cor75] modified the phase diagram of 1963 by extrapolating the measured h-BN/c-BN boundary line to the low-temperature region by analogy to the graphite/diamond equilibrium curve [Nas79]. This way, they found that h-BN was the thermodynamically stable phase under standard conditions, while c-BN was metastable. This version of the phase diagram was generally accepted up to the late 80s. Figure 1.3 shows the equilibrium lines as suggested by Corrigan and Bundy (dashed line) together with some of the experimentally observed regions for c-BN formation. In 1988, Solozhenko suggested a revised version of the phase diagram based on new experimental data on thermodynamic properties of all BN modifications [Sol88]. The h-BN/c-BN equilibrium line as calculated by Solozhenko is also shown in figure 1.3 (solid line). Its position differs drastically from the one proposed by Corrigan and Bundy, since the new equilibrium line intersects the temperature axis at around 1500 K, so that the thermodynamically stable BN modification at ambient pressure is the cubic and not the hexagonal one. The previously assumed parallels between the phase diagrams of carbon and boron nitride were thereby disproved.

It is now generally accepted that c-BN is the stable phase under standard conditions. Various experiments have been performed after Solozhenko published the revised version of the phase diagram that support his calculations. For example, Singh *et al.* [Sin95], Sachdev *et al.* [Sac97] and Will *et al.* [Wil00] synthesized c-BN at pressures and temperatures far from the equilibrium line proposed by Corrigan and Bundy. Furthermore, Solozhenko was able to show that the threshold pressure for spontaneous c-BN crystallization can be lowered even down to atmospheric pressure in the presence of diamond seed crystals [Sol94]. Finally, various theoretical calculations were carried out as well [Alb97a, Alb97b, Ker99] and were found to be in good agreement with the phase diagram published by Solozhenko.

Both w-BN and r-BN have no thermodynamically stable region in the equilibrium (p,T) phase diagram of boron nitride over the whole range of pressures and temperatures. However, w-BN can be synthesized by a transformation of h-BN or r-BN under high pressure. In general, the similar stacking between h-BN and w-BN (AA'AA'...) and between r-BN and c-BN (ABCABC...) plays an important role in bulk-phase transformations. A transition from h-BN to w-BN and r-BN to c-BN, respectively, involves two deformation processes: a lattice compression along the c axis and splitting of flat basal layers [Kur96]. These changes result in an increase of density from 2.2 up to 3.5 g/cm^3 and in a formation of sp^3 hybridized tetrahedral bonds [Fur94, Kur96]. On the other hand, a direct transition from h-BN to c-BN and from r-BN to w-BN is unlikely, since it would require both breaking and changing the nature of chemical bonds [Vel91]. Thus, the direct transformation from h-BN to c-BN requires the simultaneous application of very high temperatures and pressures in order to overcome the activation barrier for the conversion.

1.3 Boron nitride synthesis techniques

1.3.1 High pressure – high temperature (HPHT) synthesis

The HPHT technique is to date the only method that allows for the growth of c-BN single crystals. Cubic BN is usually produced from h-BN powder as the starting material in contact with a flux precursor within a high-pressure cell [Vel91]. Different kinds of catalyst material have been used by many researchers, e.g. alkali metals, alkali earth metals, and other metallic alloys as well as their fluorides, nitrides, and oxides. The crystals obtained are generally small in size (submicron to approx. 1 mm in diameter), and are often between amber and yellow in color, which is due to inclusions of the precursor material. Recently, Taniguchi and co-workers were able to synthesize well-faceted, 1 mm transparent and 3 mm colored c-BN crystals by using a temperature-gradient method under high pressure [Tan01]. Moreover, by using a specific Ba-BN solvent system, they obtained colorless crystals showing high optical transmittance as well as a low impurity concentration [Tan04].

1.3.2 Non-energetic chemical vapor deposition

The fact that cubic boron nitride is the stable BN modification at standard conditions (see section 1.2.2) has motivated the search for a way to grow c-BN directly from the vapor phase in a low-pressure, near-equilibrium process. Up to now, all efforts to form c-BN by means of ”classical” chemical vapor deposition (CVD) have remained unsuccessful. In the reports of c-BN synthesis by thermal or non-highly energetic processes, either phase characterization was performed by an insufficient number of complementary techniques or the characterization data contain irregularities or inconsistencies [Mir97a]. Furthermore, none of the experiments presented could be reproduced. Consequently, a low-pressure synthesis process permitting the formation of pure and well-crystallized c-BN films by a CVD method does not exist so far.

Contrary to this, pure polycrystalline, adherent diamond coatings and thick free-standing layers can be produced quite easily on various substrates [Bar96]. This seems surprising in view of the fact that diamond is the metastable carbon modification at standard conditions, and graphite is the stable one. In the case of boron nitride, the cubic phase is stable while h-BN is metastable. Yet, under normal and low-pressure experiments always the metastable h-BN forms. A qualitative explanation for this behavior was given by Bohr and co-workers [Boh95] by referring to the two empirical principles of Ostwald and Ostwald-Volmer, which are general rules of thumb for the kinetic behavior of chemical reactions. The Ostwald rule states that if energy is withdrawn from a system with several energy states, the system will reach the stable ground state not directly, but instead it will gradually pass through all intermediate metastable states. The Ostwald-Volmer rule says that the less dense phase is formed first. When the two rules contradict each other, the Ostwald-Volmer rule has priority over the Ostwald rule.

Both rules have successfully been applied to the diamond/graphite system. During normal CVD from a gas atmosphere carrying a carbon-containing precursor such as methane or carbon dioxide, the graphite phase is commonly formed. Although the Ostwald rule predicts the formation of the metastable diamond phase, this behavior is in agreement with the stronger Ostwald-Volmer rule, which says that the less denser phase, i.e. graphite, is nucleated first. Thus, in order to grow diamond films, the Ostwald-Volmer rule has to be suppressed. This is usually accomplished by adding atomic hydrogen to the gas phase, which permanently stabilizes the growth sites at the diamond surface by avoiding the formation of sp^2 bonds, thus stopping the graphite growth [Kon99, Kul00]. Hence, the Ostwald rule becomes dominant and the metastable diamond nucleates and can grow to pure diamond crystals.

For the boron nitride system the preferred formation of h-BN in a CVD process is a consequence of both rules. The Ostwald rule predicts the formation of the metastable h-BN and according to the Ostwald-Volmer rule, the less dense h-BN phase is also nucleated first. Therefore, *both* rules must be circumvented in order to grow c-BN directly from a gas phase. Seeding with c-BN is one possible way to overcome the preferred nucleation of h-BN and should support the onset of c-BN growth. Furthermore, a high mobility of the B and N atoms and appropriate atomic attachment kinetics are needed for the continous growth of the stable c-BN phase in order to form large and pure c-BN crystals [Bar96]. The use of elevated temperatures could be a way to provide the necessary mobility, but –regarding the phase diagram (section 1.2.2)– the temperature still has to be within the thermodynamic c-BN stability regime at atmospheric pressure. Moreover, additional complications are expected in the CVD synthesis of c-BN, as BN is a binary compound. Care must be taken that the BN stoichiometry is maintained during deposition, avoiding the relative loss of nitrogen from the solid.

1.3.3 Energetic chemical vapor deposition

Recently, enormous progress in c-BN thin film growth was achieved by the work of Matsumoto and Zhang. Using a DC plasma-jet CVD process and microwave plasma CVD with an Ar-N_2-BF_3-H_2 mixture and biased substrates, up to 20 μm thick c-BN films could be grown at a rate of up to 0.3 μm/min (see figure 1.4) [Mat00, Mat01]. The deposited films showed a high phase purity, with a c-BN content of over 90%. Columnar growth was observed, and each column was found to be nearly a single crystal with a lateral size of up to 0.5 μm and the length across the film thickness. However, large amounts of defects such as stacking faults and twins were found within the crystals. Nevertheless, the films showed good adhesion to the substrates, which was attributed to very low stress values of about 1–2 GPa. These values are much lower than the values of 4–20 GPa typically observed in

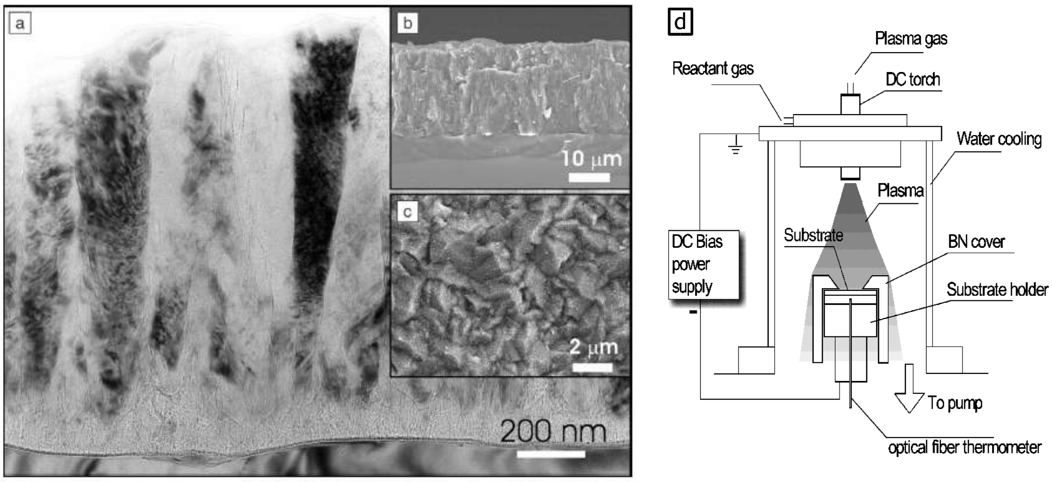

Figure 1.4: SEM cross-sectional (a,b) and plan-view (c) images of c-BN films deposited using a DC plasma-jet CVD process. (d) schematic diagram of the DC jet plasma chemical vapor deposition reactor (taken from refs. [Mat00, Mat01]).

c-BN films [Mir97a].

Although the deposition conditions chosen by Matsumoto and Zhang approach those of diamond CVD, there are still striking differences to a "classical" CVD method. Three factors were reported to be essential for c-BN deposition: (i) the use of fluorine-containing gas, (ii) negative substrate bias, and (iii) high density plasma [Mat00]. The use of fluorine was found to be crucial for c-BN growth; substituting BF_3 by B_2H_6 or BCl_3 has led to no cubic phase formation. Furthermore, even with fluorine, if no bias voltage was applied, no deposition of c-BN occured, but the substrate was etched or only thin h-BN films were deposited. This implies that ion bombardment induced by substrate bias must be indispensible for the formation of sp^3 bonds, a feature similar to PVD methods (see section 1.3.4).

Since it is know from a number of studies that fluorine effectively etches BN [Kal98, Fel02], Zhang and Matsumoto suggested that fluorine plays a predominant role in the formation of c-BN by preferentially etching h-BN [Zha00]. Furthermore, not only the amount of fluorine in the gas phase phase was found to be important for c-BN growth, but the hydrogen/fluorine ratio as well. When hydrogen was added into the reactant gas, the following reaction

$$2BF_3 + N_2 + 3H_2 \rightarrow 2BN + 6HF$$

is favored [Kal98] and the amount of BN is calculated to increase with the increase in H_2. Additionally, the formation of HF reduces the etching of BN by fluorine due to the stability of HF [Zha00]. It was therefore concluded that the flow rate of hydrogen controls the formation of solid BN from the gas phase while the ratio of hydrogen to fluorine is responsible for maintaining equilibrium between formation and etching. The substrate bias may then be necessary to establish a sensitive balance between fluorine and hydrogen surface chemistry, resulting in either etching, c-BN growth or h-BN growth [Hof04b]. This assumption is further supported by the experiments performed by Zhang *et al.* [Zha04a], who deposited c-BN films on diamond substrates by using plasma-enhanced chemical vapor deposition (PECVD). They were able to grow high-quality c-BN films even with bias voltages as low as -20 V (in contrast to -40 V needed for c-BN growth on silicon with the same method) and suggested that the ion bombardment here is required to break B-F bonds in order to allow further B-N bonding [Zha04a].

In summary, c-BN growth in a thermal CVD process has not been accomplished yet. Although the method introduced by Matsumoto and Zhang is able to produce almost stress-free, thick and adherent c-BN films, it has certain drawbacks such as the need of very high temperatures during deposition (T≈ 1100 °C), which should be further reduced in view of applications.

1.3.4 Ion-beam- and plasma-assisted deposition

Boron nitride thin films can be grown with a variety of PVD (*physical vapor deposition*) synthesis techniques. In order to form the cubic phase, the substrate must be heated (usually up to several 100 °C) during the deposition process, while the growing film must be irradiated with energetic particles at the same time. Thus, the synthesis methods differ primarily in the sources of B and N and how the energetic-particle bombardment is provided. Usually the films are irradiated with energetic ions, but it has been shown that c-BN film growth can also be accomplished by using energetic *neutrals* instead of ions [Lu94]. Figure 1.5 shows a simplified schematic illustration of the two basic processes commonly applied for c-BN film synthesis: ion-assisted deposition and plasma-assisted deposition.

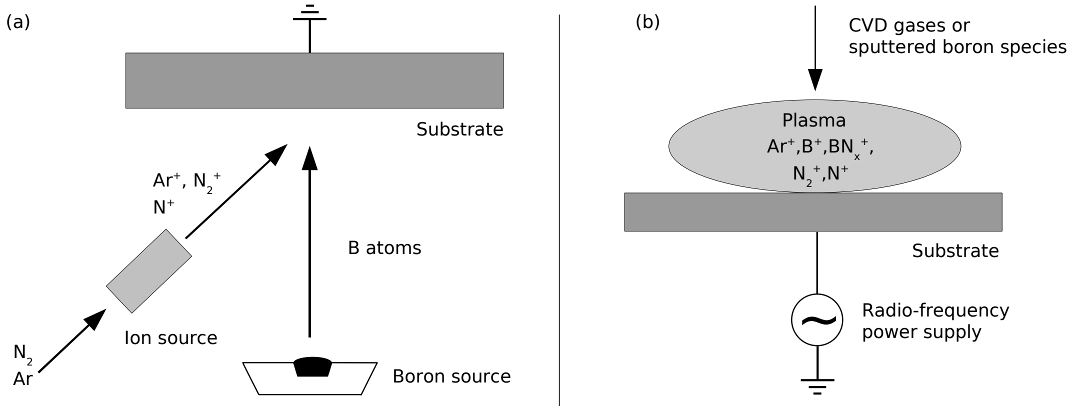

Figure 1.5: Schematic illustration of (a) an ion-assisted deposition process. Boron is evaporated, while energetic Ar or N_2 ions are provided by an ion source. (b) In a plasma-assisted process, ions are extracted from a plasma discharge and accelerated towards the substrate (taken from ref. [Mir97a]).

Plasma-assisted processes employ a high density plasma source and a low processing gas pressure under high vacuum (HV) conditions. The substrate is usually biased at several 100 eV to extract the ions from the plasma (see figure 1.5b). The plasma can be generated using a variety of source materials, e.g. *plasma-assisted chemical vapor deposition (PACVD)* methods use gaseous B-containing species such as diborane or borazine as plasma sources. In PVD-like processes the material is often provided by sputtering a B, BN or B_4C target, either by using radio frequency (r.f.) or direct current (d.c.) magnetron sputtering. Direct current sputtering is only possible with conducting targets like B_4C, but it is usually accompanied by a higher growth rate as compared to r.f. sputtering. The latter, however, does work with insulating targets like h-BN or pure B. This technique has been extended and modified in the past, e.g. applying a negative bias voltage to the sample has been shown in several cases to enhance the onset of c-BN nucleation [Mir97a]. Furthermore, the use of magnetic fields can increase the ion flux, thus allowing for a higher deposition rate, and both unbalanced magnetron sputter sources as well as conventional magnetron sources combined with external magnets or coils have been used to extend the plasma.

In ion-assisted processes the boron-containing species is provided by either electron beam evaporation *(ion beam assisted deposition, IBAD)*, laser ablation *(pulsed laser deposition, PLD)* or ion beam sputtering (IBS) of a solid h-BN or B target (figure 1.5a). Boron atoms and/or BN molecules are then deposited with thermal energies onto the substrate. Simultaneously, the growing film is bombarded with nitrogen and (most often) noble gas ions with typical energies of several 100 eV. The growth process is therefore rather complex and different effects such as condensation and thermal desorption, implantation of ions, recoil implantation of atoms deposited on the surface and sputtering have to be considered. Moreover, the interpretation of the obtained data within the existing c-BN growth models is difficult, because the substrate is not only irradiated with ions (which have well-defined energies) but also with neutral atoms, molecules and clusters.

These problems do not exist for a specific type of PVD method, namely the *Mass-Separated Ion Beam Deposition (MSIBD).* In contrast to all other PVD techniques, thin films are prepared solely by deposition of alternating cycles of energetic B^+ and N^+ ions under ultra-high vacuum (UHV) conditions [Hof95]. In this case, the deposition parameters, like ion energy, ion flux ratio of different ion species and the substrate temperature are well-defined and independently controllable. As opposed to IBAD, both nitrogen and boron are deposited as singly charged energetic ions and no noble gas or other ions nor neutral atoms or molecules are involved. Figure 1.6 shows a schematic diagram of the MSIBD process. The ions are created in an appropriate ion source, accelerated to a high energy in order to create an intense beam and magnetically mass separated. The isotopically pure ion beam is then guided into the deposition chamber, where the ions are decelerated down to energies between 10 eV and several keV and impact onto the heatable substrate. The amount of deposited ions can be accurately determined by measuring the ion charge. This relatively simple deposition process makes MSIBD to the ideal tool to study the influence of the deposition parameters on c-BN growth. However, its deposition rate is only in the order of several 10 nm/h, which makes an industrial application almost impossible.

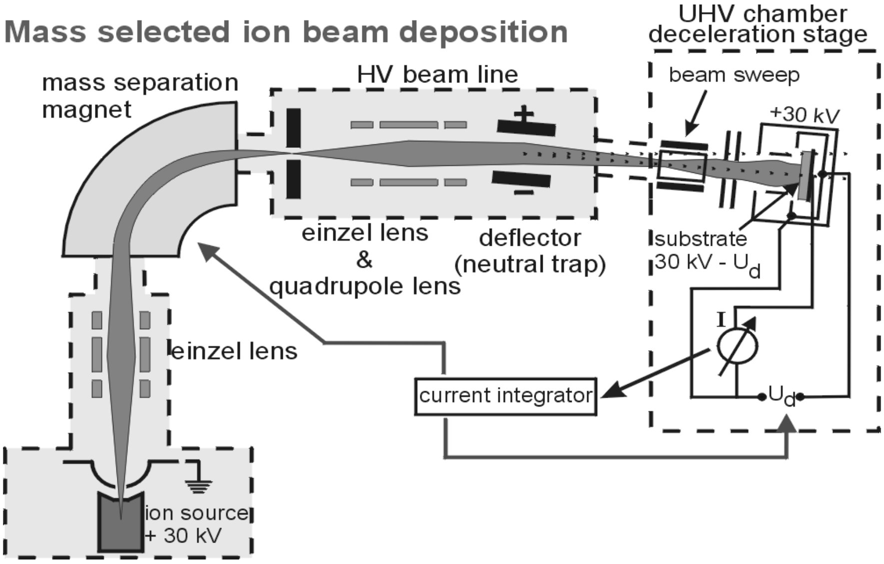

Figure 1.6: Schematic diagram of the mass separated ion beam deposition technique. The ions are created in a Sidenius-type ion source, accelerated to 30 keV and magnetically mass separated. The isotopically pure ion beam is then guided into the deposition chamber, where the ions are decelerated down to energies between ≈10 eV and several keV. The amount of deposited ions is accurately measured by the ion charge.

1.4 Microstructure of c-BN films

C-BN films have been deposited on a variety of substrate materials, but the vast majority of studies have employed silicon substrates. On silicon and almost all other types of substrates, c-BN films are never in direct contact with the substrate. Instead, a characteristic layer structure is usually observed, consisting of an amorphous layer containing substrate and deposited atoms followed by a textured graphitic BN phase. Cubic BN then nucleates on top of this sp^2-bonded layer while following a specific crytallographic relation to the underlying material. Finally, the c-BN film surface is usually covered with a thin layer of sp^2-bonded material. Although this film structure is observed for almost all types of substrates, deposition parameters and synthesis techniques, it can be significantly altered by choosing specific substrates and/or deposition conditions. This will be further discussed in section 1.5.

Figure 1.7a shows a high-resolution transmission electron microscopy (HRTEM) image of a c-BN film in cross-section. The sample was grown on a silicon substrate using mass separated ion beam deposition (MSIBD) within the framework of this thesis. The Si(100) substrate is followed by an amorphous or highly disordered region that is a few nm thick. This layer is often referred to as "amorphous boron nitride" [Kes94a, Mir97a] or has been described as an ion-mixing layer containing substrate and deposited atoms [Hof96]. The latter is further supported by the fact that the layer thickness scales with the ion energy and corresponds very well to the ion range [Hof97]. Additionally, in a recent study this region was revealed by energy dispersive x-ray spectroscopy (EDX) to be composed of a mixture of B, N, Si and O atoms [Yan03]. Although the initial layer is most likely caused by the ion beam since silicon is easily amorphized by low-energy ion bombardment [Kim99], it seems not to be a necessary precursor to the microstructural evolution of c-BN. Yang and co-workers were able to eliminate the amorphous region by using a 1200 K heat treatment in a H_2 atmosphere followed by N_2 plasma etching prior to deposition [Yan03].

The initial layer is followed by a textured, yet disordered sp^2-bonded BN layer, which has its (0002) planes (i.e. its basal planes) perpendicular to the substrate surface. Although this interlayer is often labeled as "hexagonal BN" (h-BN), it in

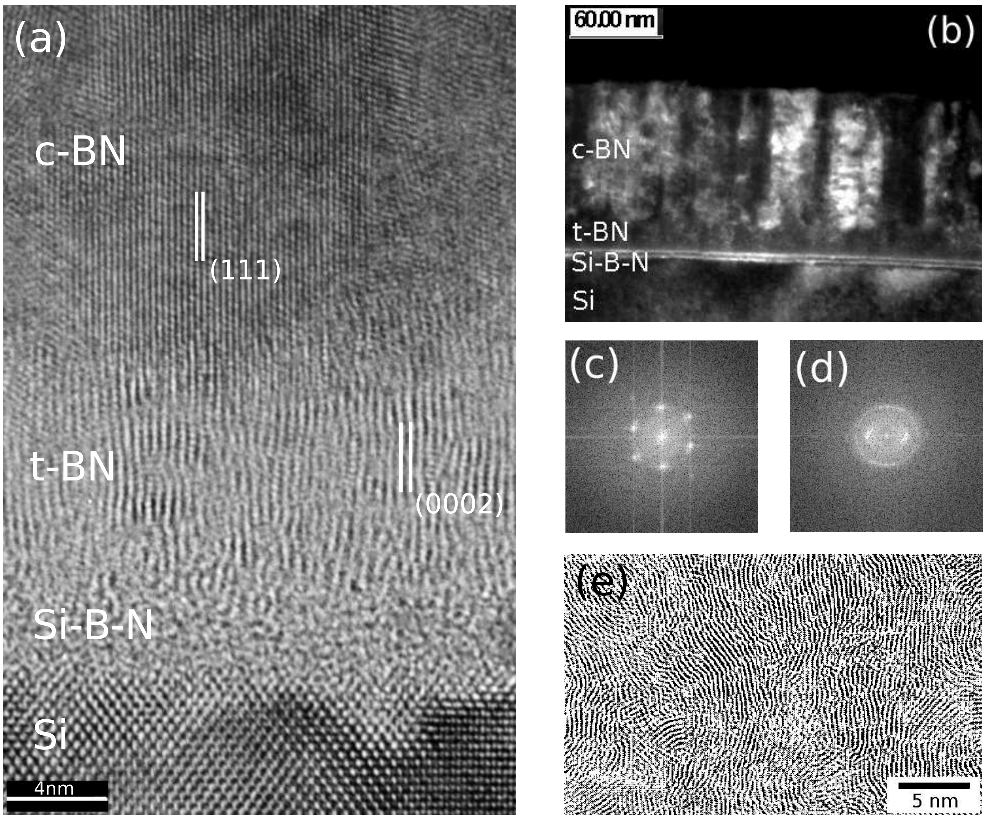

Figure 1.7: (a) High resolution cross-sectional TEM image of a c-BN film showing the typical layer sequence consisting of an interfacial layer containing substrate and deposited atoms, followed by a textured layer of turbostratic BN (t-BN). Cubic BN nucleates on top of the t-BN layer with a 3:2 lattice matching between its {111} planes and the (0002) t-BN planes. (b) Dark field micrograph of the entire film in cross-section. The image was obtained from the c-BN (111) reflections and shows columnar c-BN grains extending to the film surface. (c,d) Typical FFT image showing the cubic (111) (c) and t-BN (0002) (d) reflections. (e) HRTEM image of a t-BN film in plan view showing highly distorted basal planes (taken from Ref. [McC96]).

fact consists of parallel h-BN and r-BN lamaella obeying specific orientation relationships [Sht00]. In h-BN the basal planes are stacked in a periodic (AA'AA'...) sequence (see section 1.2.1), but in this case they are rotated randomly around the c-axis and only roughly parallel to each other. Additionally, the orientations of the [0002] directions about the film normal are random, too (figure 1.8d). In figure 1.7e, a plan view HRTEM image of this layer is displayed. Although the basal planes remain continuous, they are highly distorted and bend through different orientations. Such a structural modification is known as turbostratic in the case of graphite, and this term has been transferred to the BN case as well [Tho63, Med94]. Turbostratic BN (t-BN) is often identified by means of selective area diffraction (SAD), and a typical SAD image is displayed in figure 1.7d. The two bright diffraction spots exhibit a d spacing of 0.315–0.385 nm, which can be associated with the $(0002)_{\mathrm{t-BN}}$ planes [Sht00].

The origin of the observed *in-plane c-axis* texture (i.e. the basal t-BN planes are perpendicular to the substrate surface) is still not clear. It is unambiguously related to the ion irradiation, though, since in its absence the orientation of the c-axis is random or has an out-of-plane texture as has been observed for BN as well as graphitic C and CN_x films [McC97]. McKenzie *et al.* proposed that the texture of the t-BN layer results from compressive stress induced by ion irradiation during BN film growth [McK93]. They calculated the Gibbs energy for an elastically strained graphitic material, and it was found to be smaller if the basal planes were perpendicular rather than parallel to the substrate surface. Therefore, of the two orientations, the in-plane c-axis texture is favoured because of its lower Gibbs free energy. Cardinale *et al.* extended this analysis by examining all possible orientations of the stress plane relative to the crystallographic directions [Car97], and they found that the configuration with the lowest Gibbs free energy is that with the basal planes tilted about 45° from the substrate. As this is contrary to the experimentally observed texture, they proposed that it is instead produced when the graphitic BN plastically deforms to relieve the ion-induced stress. McCarty and Medlin followed this idea and suggested a mechanism based on plastic deformation modes (i.e. basal-plane slip[1] and kinking[2] processes) as being responsible for rotating the c-axis towards the plane of biaxial compressive stress [McC97]. Once the c-axis has rotated to lie in the plane of the substrate, further deformation by basal-plane slip cannot occur. Without any other stress-reduction pathways, the

---

[1] Slip causes relative movement of two parts of the crystal parallel to certain crystallographic planes (the slip planes) along one of the crystallographic directions that lie in the slip plane. Slip occurs when the component of stress that lies in the slip plane and along the slip direction exceeds a critical value.

[2] Kinking is a form of deformation caused through basal-plane slip and is commonly observed in materials with only one slip plane, such as graphite or hexagonal BN.

stress level will rise if further strain (e.g. through additional ion irradiation) is introduced into the material. This has led McKenzie *et al.* to the formulation of a ”stress model” for the formation of c-BN thin films [McK93].

If the deposition parameters are within certain limits (see section 1.5), the cubic BN phase will nucleate on top of the t-BN layer. Although the transition from t-BN to c-BN is quite sharp, the interface region is uneven and has a width of several nm (see figures 1.7a and 1.8a). In contrast, the surface is generally very smooth, with reported root-mean-square (rms) roughnesses of around 1 nm [Yos96]. The c-BN layer itself consists mostly of columnar grains with a diameter of a few to several 10 nm that often extend from the interface to the top of the film, as can be seen in the dark-field TEM image in figure 1.7b [Mir97a]. The grains most often exhibit high twin and stacking fault densities [Zho95a, Sht00], whereas the atomic structure of a grain boundary seems to depend on the orientation relationship between adjacent c-BN grains and the boundary inclination [Sht00]. The presence of 1-2 nm h-BN [Zho95a], sp^2-bonded BN as well as c-BN twin boundaries [Sht00] between individual c-BN crystallites has been reported.

As with the graphitic t-BN layer, the cubic phase is also textured and exhibits preferential crystallographic orientation. The individual crystallites have at least one [111] direction lying in the plane of the film but are otherwise randomly oriented about the substrate normal as well as the in-plane c-BN [111] axis [Mir97a] (see figure 1.7c). Furthermore, the crystallographic relations in c-BN are such that the c-BN {111} planes form parallel to the t-BN (0002) planes [Med96], which is most likely due to the structural similarities of the two types of planes (figures 1.7a and 1.8a). Both the c-BN {111} and the graphitic boron nitride basal planes consist of sixfold rings of alternating boron and nitrogen atoms with similar projected dimensions. The relative spacings of the $(0002)_{\mathrm{t-BN}}$ (around 3.3 Å) and $\{111\}_{\mathrm{c-BN}}$ (2.09 Å) planes at the interface approach a 2:3 ratio, so that every third c-BN (111) plane (stacked in a three-layer ABCABC... sequence) is almost perfectly matched with every alternate t-BN (0002) plane (stacked in a two-layer AA’AA’... sequence) [Med96, Hof97, Sht00]. However, in order to obtain a perfect matching, the t-BN planar distance has to be compressed from 3.3 Å to 3.15 Å, i.e. by about 4% [Hof97], which is conceivable under the large compressive stresses typical in c-BN films. Also, because of the large bulk modulus of c-BN, it is unlikely that the (111) planar distance is expanded [Hof97].

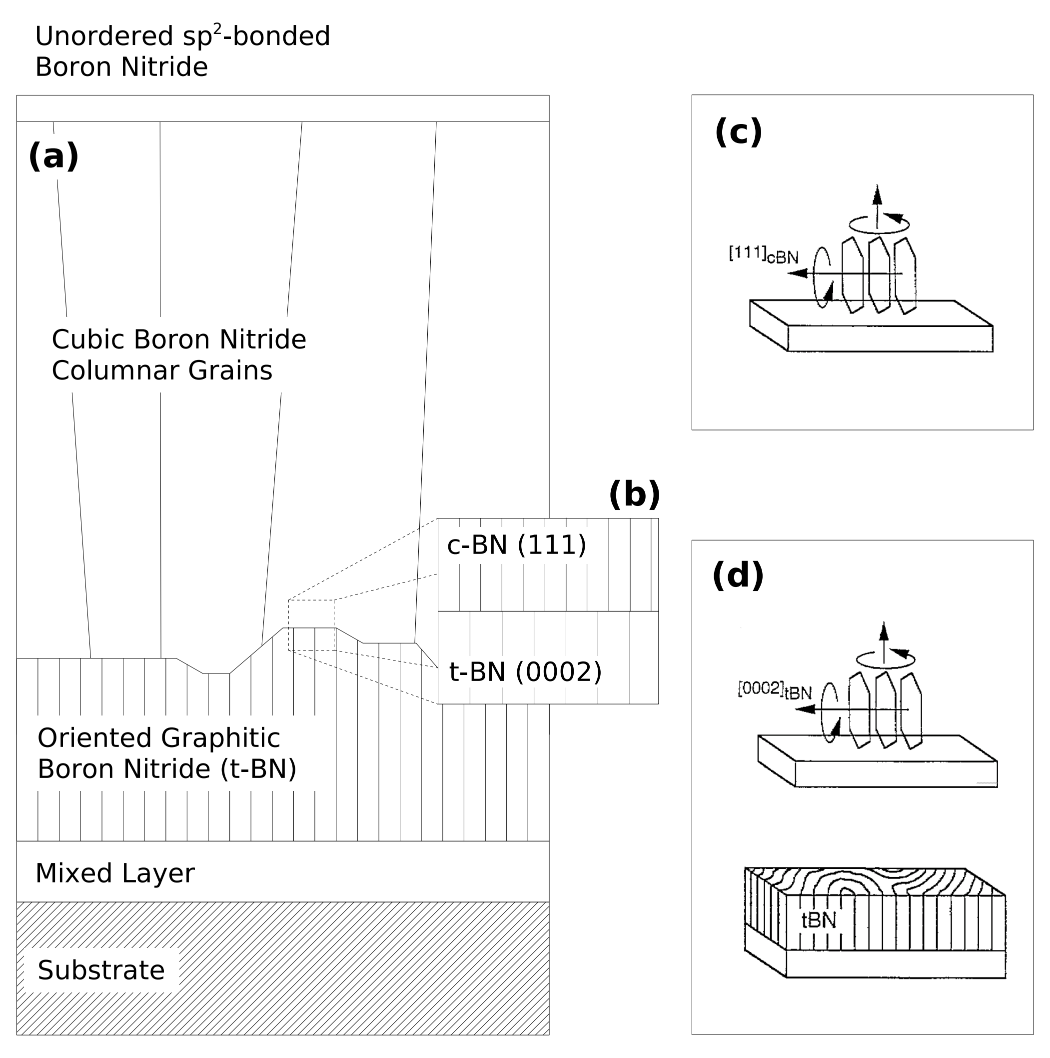

Figure 1.8: (a) Schematic diagram summarizing microstructural features of c-BN films. The mixed layer, which is most likely caused by the incident ion beam, is followed by a layer of turbostratic boron nitride. Cubic BN forms on top of the t-BN layer and grows in a textured, albeit nanocrystalline manner. (b) Magnification of the c-BN/t-BN interface. The c-BN (111) planes are parallel to the t-BN (0002) planes while following a 3:2 lattice match. (c) Possible orientations of the $[111]_{\mathrm{c-BN}}$ directions in relation to the film plane. The $\{111\}_{\mathrm{c-BN}}$ planes are perpendicular to the surface but are otherwise randomly oriented about the surface normal and about the in-plane $[111]_{\mathrm{c-BN}}$ axis. (d) Possible orientations of the $[0002]_{\mathrm{t-BN}}$ directions. The (0002) planes are roughly perpendicular to the substrate surface, but randomly rotated around the c-axis (taken from Ref. [Mir97a]).

Finally, the surface of a c-BN film is usually covered with an sp^2-bonded BN layer. Since it is generally too thin (< 1 nm) to be detectable by TEM, it has been analyzed by many groups using surface-sensitive techniques like electron energy loss spectroscopy (EELS) [Bou94, Hof97, Fel98], Auger electron spectroscopy (AES) [Fri94] or x-ray photoelectron spectroscopy (XPS) [Par97]. The thickness of the sp^2-bonded layer corresponds quite well to the ion range and the transition region between this layer and the bulk c-BN is regarded as the actual growth region of c-BN, where part of the surface layer is transformed into c-BN upon ion impact [Fel98]. The surface layer is usually unordered, but a textured t-BN phase covering the c-BN film has been reported as well [Hof02].

1.5 Parameters controlling cubic phase formation

Most of the c-BN deposition studies have been carried out by applying ion beam assisted synthesis techniques (IBAD). As mentioned before, film growth using IBAD techniques is very complex, particularly due to the fact that at least part of the energy input into the film is indirect. While boron atoms typically have thermal energies when they reach the substrate, Ar^+ and N^+ ions with energies of several 100 eV are commonly used to supply supplemental energy. Consequently, c-BN nucleation and growth is governed by a number of interdependent parameters, i.e. ion/neutrals flux ratio, ion energy, ion mass, ion angle of incidence and substrate temperature. In this section, the role of these parameters in the microstructural evolution of c-BN films will be discussed. Additionally, a brief review on the influence of the substrate material on c-BN film formation will be presented.

1.5.1 Substrate effects

The use of materials other than silicon as substrates for deposition of cubic boron nitride thin films was mainly motivated by the fact that none of the low-pressure synthesis methods ever succeeded in the epitaxial growth of c-BN on any substrate. Instead, the typical layer sequence as described in section 1.4 has always been found. It has been suggested before that the geometric similarities at the t-BN/c-BN interface might be the reason for the nucleation of c-BN in analogy to the nucleation of diamond on graphite [Mir97a, Med96, Zho95b, Wat95, Li93]. However, the role of the t-BN interface layer in the nucleation of c-BN is not well understood and the mechanisms leading to the distinct interlayer texture remain unclear. Specifically, the question whether c-BN nucleates *from* or *on* the graphitic interlayer was and is still under active discussion. In the first view, this layer is seen as a precursor for the cubic phase where the t-BN basal planes become the c-BN $\{111\}$ planes due to a direct, pressure-induced solid state t-BN to c-BN phase conversion [Med96, Sht00]. In the second view, the t-BN layer is regarded as a preferential nucleation site rather than a direct precursor, which would provide the boundary conditions necessary for the formation of the cubic phase [Kes93, Med96]. The latter would explain the semicoherent interface and crystallographic alignment observed between both phases. If this is indeed true, the nucleation of c-BN as the initial phase should be possible on crystalline substrates with a suitable lattice match.

In pursuit of c-BN thin film heteroepitaxy, Kester and co-workers used ion beam assisted deposition to grow BN films on nickel, copper, and single crystalline diamond substrates [Kes94b]. It was thought that those materials would be better suited as substrates for c-BN growth as compared to Si, because they all have lattice spacings very close to that of c-BN. While the Si/c-BN lattice mismatch is about 33%, it is only 2.6% for Ni, 1.45% for diamond and less than 0.05% in the case of Cu [Kes94b]. However, on diamond and Ni, deposition has led to the same sequence of amorphous, turbostratic and cubic layers that is observed on silicon substrates. Moreover, when using a Cu substrate, the films were completely sp^2-bonded, with no evidence of c-BN at all.

In the following years, many other materials have been used as substrates for the growth of c-BN films. This included different metals like aluminum [Mir96, Pai93, Lue95], gold or silver [Mir96] as well as compound semiconductors such as silicon carbide [Mir95] or titanium nitride [Mir96]. An extensive overview is given in Ref. [Mir97a]. Although in some cases films with high c-BN content (i.e. $> 85\%$) were synthesized, heteroepitaxial growth had not been accomplished. Mirkarimi *et al.* observed that the c-BN content in the films decreased with decreasing metal substrate hardness [Mir95], a behavior, which was explained within the stress-induced c-BN formation models. The stresses generated in the growing film are supposed to be absorbed better by more ductile metals, delaying or even impeding c-BN nucleation [Kes94b, Mir96]. Since data on the microstructure of

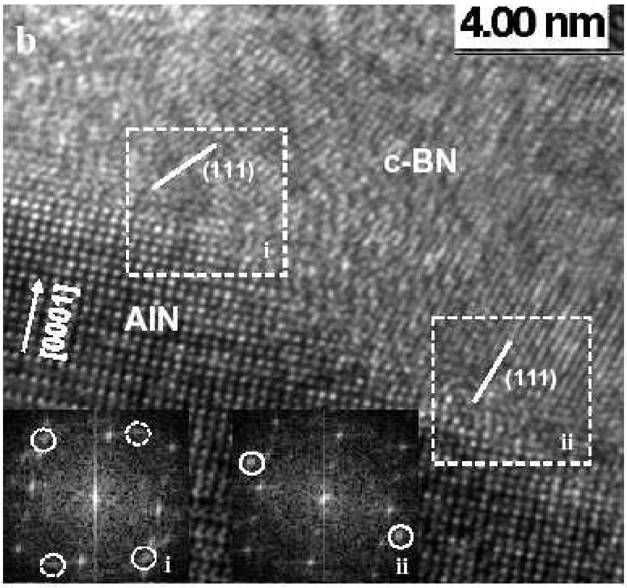

Figure 1.9: HRTEM image of the BN/AlN interface area at AlN grain tips showing c-BN growth directly on the substrate. The FT images inserted correspond to the framed areas. The orientation of the c-BN (111) planes depends on the exposed AlN facet. Spots corresponding to c-BN (111) planes are marked by circles in the inset (from Ref. [Fel01]).

the substrate-film interface are sparse, little is known about the suitability of one metal or the other for heteroepitaxy. However, Desrosiers and co-workers examined BN growth on Ni substrates, and they found the formation of nickel boride on the substrate due to diffusion of boron into the substrate [Des97]. That way, the lattice information cannot be transmitted from the substrate to the growing BN film and epitaxial growth becomes impossible. Hence, the formation of alloy interface layers might a possible explanation why heteroepitaxial c-BN growth on metallic substrates has not been observed so far.

In 2001, Feldermann and co-workers investigated the possibility of nucleating c-BN films directly onto monocrystalline w-AlN substrates [Fel01]. They stated three reasons why AlN was chosen as substrate: First, it provides a reasonably good lattice compatability to c-BN in several different orientations. Second, in order to retain the lattice structure, the substrate must not amorphize upon ion irradiation that is imperative for c-BN growth. AlN has proven to be very stable during ion bombardment due to efficient dynamic annealing. And third, the formation of a heterogenous B/Al/N interface layer as observed for metal substrates is unlikely because of significant structural differences between BN and AlN.

A detailed HRTEM study of the grown films indeed revealed successful c-BN nucleation directly on top of the AlN substrate, i.e. without any amorphous or turbostratic interlayer (figure 1.9). The predominant orientation relationships found at the AlN/BN interface are $(111)_{\mathrm{c-BN}} \approx\parallel (10\bar{1}0)_{\mathrm{AlN}}$, while the orientation of the c-BN (111) planes depend on the exposed AlN facet. However, the c-BN film was found to be nanocrystalline, and on some areas the usual sequence of amorphous, turbostratic and cubic layers was observed. Nevertheless, the study proved that the initial amorphous as well as the t-BN layer are not a necessary precursor for the onset of c-BN nucleation. The t-BN interlayer is presumably a preferred nucleation site providing the boundary conditions necessary to form c-BN, but can be avoided by chosing a substrate with a structure compatible to c-BN.

The first "large scale" heteroepitaxial c-BN growth was achieved by Zhang and co-workers in 2003 [Zha03], who applied the IBAD technique to grow c-BN films directly on highly (001)-oriented CVD diamond films and single crystal diamonds. This is surprising in the view of the fact that, although heteroepitaxial c-BN growth on diamond has been demonstrated using high pressure–high temperature (HPHT) synthesis [Lux99], the use of low-pressure methods so far always resulted in amorphous and turbostratic interlayers before c-BN nucleation [Kes94b]. This was related to the stability of a non-metallic crystalline structure against ion impact, which has been shown to decrease along with the degree of the ionicity of the interatomic bonds [Nag74]. Since diamond is covalently bonded, it is subject to amorphization by the low-energy ion bombardment during c-BN growth. This was confirmed by Reinke *et al.*, who indeed observed amorphization of a diamond surface upon prolonged low-energy Ar^+ irradiation [Rei96a]. With the diamond structure destroyed during ion impact, the lattice information cannot be transmitted to the growing film and epitaxial growth is not possible.

In contrast to preliminary experiments utilizing diamond substrates, Zhang *et al.* have used very high substrate temperatures during BN deposition, and they observed epitaxial c-BN growth only at temperatures of 900 °C or more [Zha04b]. By applying electron energy loss spectroscopy (EELS), they were able to show that ion bombardment at low substrate temperatures (i.e. below 900 °C) leads to a deterioration of the epitaxial c-BN growth due to a significant amount of radiation damage at the diamond surface. At higher temperatures radiation damage can be annealed out thereby maintaining an ordered substrate surface, hence allowing epitaxial growth of c-BN.

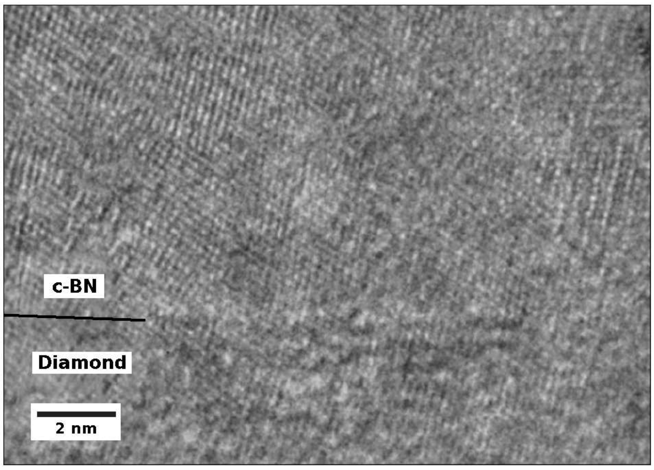

Figure 1.10: HRTEM image of a c-BN/diamond interface for a 20-nm-thick c-BN film on a 200-nm-thick CVD diamond film (from Ref. [Zha03]). Although the transition region is barely visible in the image, it was determined separately by applying EELS.

Figure 1.10 shows a typical HRTEM image of a c-BN film grown epitaxially on a (001)-oriented diamond. The actual c-BN/diamond interface is barely visible, but has been determined separately by applying EELS and examining the specific B,N and C absorption edges. The orientation relationship was found to be $(001)_{\mathrm{c-BN}} \parallel (001)_{\mathrm{diamond}}$. Additionally, the compressive stress in the film, which was calculated from the peak shift in the infrared absorption spectrum (see section 2.2.1), was reported to be much lower than the values commonly observed in c-BN films grown on Si substrates.

In summary, c-BN can be grown on a variety of substrate materials, while the cubic phase content in the film seems to be related to the substrate hardness. Heteroepitaxial growth of c-BN has been achieved on AlN and diamond so far, proving that the initial amorphous layer is not an intrinsic and necessary stage of the microstructural evolution of c-BN films. It is a by-product of the ion bombardment necessary for c-BN film formation and can be avoided by choosing a substrate with a high proportion of ionic bonds (e.g. AlN) or by using high substrate temperatures during growth, so that radiation damage caused by the incident ion beam can be annealed out and an ordered substrate surface can be maintained. Furthermore, the t-BN layer presumably acts as a preferential nucleation site for c-BN, but is not a structural precursor. By using a crystalline substrate with a structure compatible to c-BN, this layer can be avoided as well.

1.5.2 Ion energy / ion flux

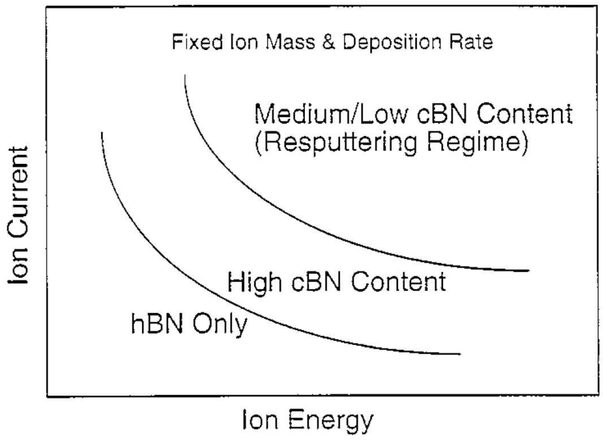

Figure 1.11: Schematic diagram showing c-BN content as a function of ion current/energy at constant ion mass and deposition rate (from [Mir97a]) The transition to low/medium c-BN content with increased ion current and energy is known to result from increased sputtering, which gives a thinner film, and ultimately a no-growth condition.

Besides high pressure–high temperature (HPHT) synthesis, c-BN thin films can be prepared with a variety of deposition techniques, but only if energetic ions or atoms are involved. It is therefore generally accepted that ion bombardment is necessary for c-BN nucleation and growth. In 1987, Inagawa *et al.* [Ina87] observed that c-BN film formation only occured in a specific range of ion current (*flux*) and substrate bias (i.e. *ion energy*) values, as shown in figure 1.11. Furthermore, the process-parameter boundaries as well as maximum c-BN percentage attained was found to be influenced by the ratio of Ar^+ to N_2^+ ions, indicating a dependence of the *ion mass* on cubic phase formation. The parameter-space plot of Inagawa and co-workers was later extended and refined by Reinke *et al.* [Rei95] and very recently by Kulisch *et al.* [Kul03] based on the data published by several other groups. In summary, the c-BN growth regime was found to be dependent on 4 parameters: (i) ion mass m_{ion} (i.e. most often the ratio of Ar to N ions) , (ii) ion energy E_{ion}, (iii) flux J (ions $cm^{-2}s^{-1}$) of the arriving ions, and (iv) deposition flux a (atoms $cm^{-2}s^{-1}$), which is generally defined as the total flux of boron and nitrogen atoms that arrive at the surface. The ion flux J and deposition flux a are usually combined to the so-called ion-to-atom ratio $F = J/a$, however, the term boron flux is often referred to as the deposition flux a in the literature.

Figure 1.12 displays BN phase formation as a function of ion energy and ion-to-atom ratio J/a as compiled by Kulisch and co-workers [Kul03]. Apparently, c-BN formation is possible only within a well-defined, sharply delimited region between the upper and lower solid lines. Above the upper line no net film growth takes place

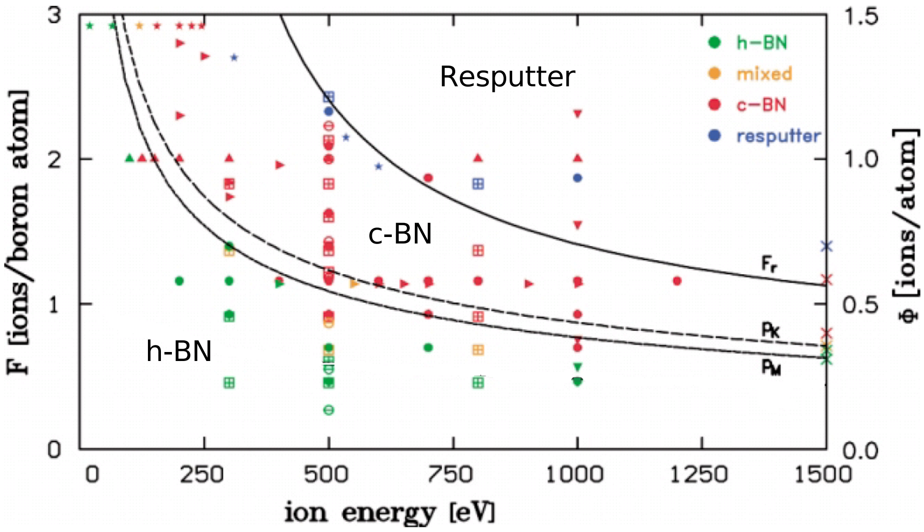

Figure 1.12: Dependence of the structure of IBAD BN films on ion energy E_{ion} and ion/boron flux F. The data has been compiled by Kulisch *et al.* [Kul03] from various IBAD inestigations. c-BN formation is possible only between the upper and lower solid lines. F_r indicates the resputter limit, p_k and p_m are the momentum thresholds as given by equations (1.2) and (1.4).

because the deposited film is completely resputtered by the stronger ion bombardment. Ion flux and ion energy were found to be interdependent, i.e. a low flux F can be compensated by a higher ion energy and vice-versa.

To be able to describe the c-BN growth process independently of the current values of flux ratio $F = J/a$, ion energie E_{ion}, and ion mass m_{ion}, Kester and Messier [Kes92] introduced a universal parameter p/a, which describes the momentum transferred by the ions into the film per deposited atom assuming a single, head-on elastic collision [Tar88]. This momentum related parameter is:

$$p/a = \sum_i (J_i/a)\sqrt{2m_i E_i \gamma_i} \tag{1.2}$$

where m_i is the mass of the ith ionic species, E_i its energy, and γ_i is the efficiency of kinetic energy transfer as given by

$$\gamma_i = \frac{4m_i M_{atom}}{(m_i + M_{atom})^2} \tag{1.3}$$

where M_{atom} is the average mass of the film atoms. The sum must be performed over all types of ions present in the ion beam. Kester and Messier, using a mixture of N and either Ar, Kr or Xe ions, respectively, in an IBAD process to grow c-BN films [Kes92], observed that cubic phase formation only occured above a critical value of $(p/a) \approx 200$ (eV·amu)$^{1/2}$ independent of the particular values of J, a, m and E. Complete resputtering, i.e. no film growth at all, was found for (p/a) exceeding about 300–400 (eV·amu)$^{1/2}$. Mirkarimi *et al.* found an $E^{1/2}$ dependence for the growth of c-BN as well [Mir94], however, they reported that the c-BN formation threshold could be better described by the *total* momentum of the bombarding ions (p_{tot}/a) transferred to the film per deposited atom, i.e.

$$(p_{tot}/a) = \sum_i (J_i/a)\sqrt{2m_iE_i}. \tag{1.4}$$

It was argued that the assumption of the momentum transferred in a single, binary collision between ions and film atoms is not realistic. Instead, the interaction of a several hundred electronvolt ion with the substrate material is a complicated cascade involving many separate collisions for which the total ion momentum is ultimately transferred to the film.

Both parameters, p/a (eq. 1.2) and p_{tot}/a (eq. 1.4), are frequently used in the literature for comparison and discussion. Although the c-BN formation thresholds as predicted by those parameters were confirmed by many groups, the $\sqrt{mE}$ scaling seems to break down for low ion energies [Mir97a]. For example, Ulrich and co-workers [Ulr96] used ions from sputter-source plasmas and reported critical J/a values of 13–66 for ion energies of 140–60 eV. The respective momentum transfer values calculated from these results by using either equation (1.2) or (1.4) are significantly larger than the reasonably consistent values reported by other groups for ion energies above 200 eV [Mir94, Bou94, Gan94]. Although some of those differences may result from processing or measurement differences, they indicate that the c-BN growth process is not solely controlled by the momentum transfer.

It is of importance to note that one has to discriminate between c-BN *nucleation* (i.e. the initial formation) and *subsequent growth.* The data sets and phase diagrams (such as displayed in figure 1.12) were initially compiled in order to establish a parameter space for c-BN nucleation, thus they do not necessarily apply to c-BN growth, too. In fact it has been found that all parameters described above can be reduced after nucleation, at least down to certain new thresholds. McKenzie *et al.*

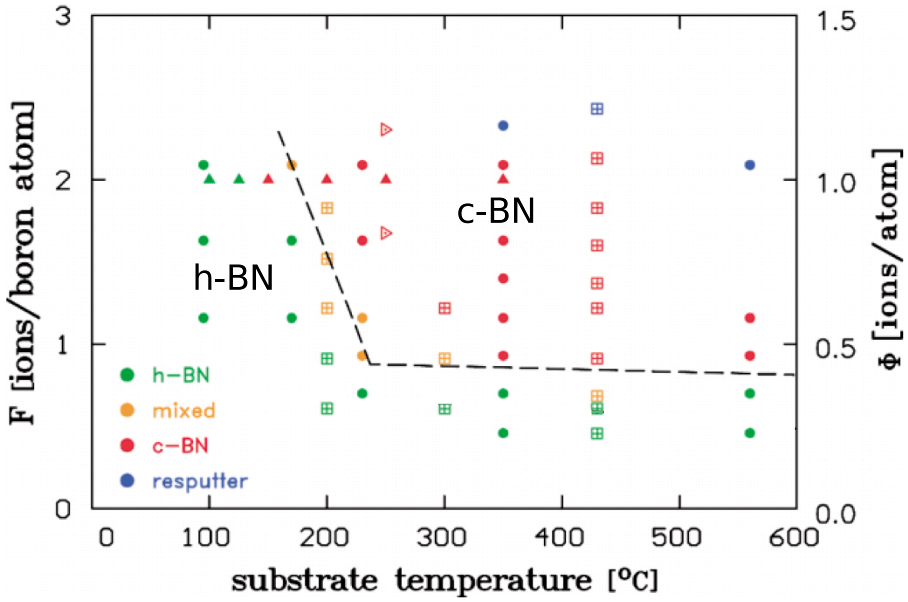

Figure 1.13: Deposited BN modification as a function of the flux ratio F and the substrate temperature T_S as compiled by Kulisch *et al.* [Kul03].

[McK95] and Hahn *et al.* [Hah97] were able to reduce the ion energy significantly after c-BN nucleation without interrupting cubic film growth. Additionally, Hahn and co-workers [Hah97] also reported that a larger ion momentum per deposited atom is necessary to initiate c-BN formation than to subsequently grow c-BN. This probably indicates that both processes are based on different mechanisms, although they both require energetic particle bombardment.

1.5.3 Substrate temperature

Besides ion energy or flux, the substrate temperature has been identified as another important parameter for the formation of c-BN films. In contrast to the rather narrow range of ion-to-atom ratio for which c-BN nucleation is possible (see figure 1.12), films with a high cubic phase content can both be nucleated and grown at a wide range of temperatures extending from about 100–200 °C [Tan92, Fri94, Hof97] up to over 1000 °C [Mir97a, Lit99, Mat00]. Figure 1.13 shows the c-BN growth regime as a function of flux ratio and substrate temperature. The lower temperature

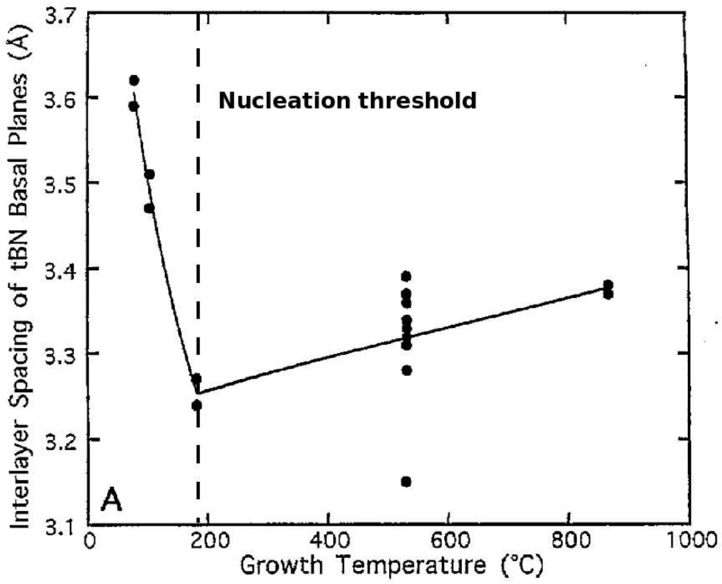

Figure 1.14: Interlayer spacing of the t-BN basal planes as a funtion of substrate temperature (taken from ref. [McC96]).

threshold of about 200 °C is clearly visible below which no c-BN can be formed. In the region of this threshold a low temperature can be compensated by a high flux ratio F, but above $T_S \approx 250$ °C the threshold for F is almost independent of the temperature. For example, Mirkarimi *et al.* could readily produce c-BN films at $T_S = 130$ °C, but could not synthesize c-BN below $T_S \approx 100$ °C, although the flux ratio was increased up to the resputter limit [Mir95].

The existence and significance of a temperature threshold T_T is not obvious. The region of c-BN stability in the equilibirum (p,T) BN phase diagram (figure 1.3) extends from room temperature to temperatures far above T_T, so the observed threshold cannot be explained from a thermodynamical point of view. Furthermore, Mirkarimi *et al.* pointed out that the energy transferred to the film atoms by the bombarding ions is sufficient to displace each film atom from its binding site on the order of ten times [Mir94]. Hence, it is difficult to understand why such a low temperature and a difference of only several ten °C should determine the growth of either c-BN or t-BN. McCarty *et al.* therefore suggested that the temperature threshold is related to the initial nucleation of c-BN, and not necessarily its growth [McC96]. Although they as well observed a process-dependent threshold temperature below which c-BN films cannot be nucleated, they were able to continue c-BN growth at temperatures below the threshold by depositing on an initial c-BN seed layer. Furthermore, by examining the structure of the t-BN layer as a function of substrate temperature, they found that the local order within the t-BN basal planes deteriorates with decreasing substrate temperature. At the same time the separation of the basal planes increases suddenly and sharply just below the threshold temperature (figure 1.14). The authors stated that the order of the basal planes is also influenced by ion irradiation, but the observed increase in graphitic-plane separation below the temperature threshold is larger than can be accounted for exclusively by ion-induced stress effects. It was therefore concluded that both ion-induced compressive stress and substrate temperature play an essential role in ordering the t-BN interlayer structure. Hence, the effect of substrate temperature is most likely related to the establishment of the boundary conditions necessary for c-BN nucleation (see sections 1.4 and 1.5.1).

Not only can the deposition parameters described in section 1.5.2 be reduced after c-BN nucleation without interrupting its growth, but also the substrate temperature. McCarty *et al.* [McC96] and Ye [Ye00] reported minimum substrate temperatures in the order of 80 °C, and Feldermann *et al.* were able to maintain c-BN growth even at room temperature using the MSIBD technique [Fel99]. In summary, there is strong evidence that the temperature threshold is related to c-BN nucleation, while the growth itself seems to be temperature independent. More insight into the role of the substrate temperature is given in section 3.3.

Chapter 2

Experimental methods and characterization techniques

2.1 Boron nitride thin film deposition

All boron nitride films investigated in this work have been prepared using the mass separated ion beam deposition system ADONIS (see section 1.3.4 for a general description of the MSIBD technique), which has been described in detail in refs. [Hof94] and [Hof96]. Its current status is shown in figure 2.1. The ions are created in a Sidenius-type ion source, which is usually operated using Ar as carrier gas. Nitrogen is introduced as N_2 gas whereas boron is evaporated from B_2O_3 powder. After acceleration to 30 keV, the ions are mass-separated in a 90° sector magnet and guided into the deposition chamber. Several einzel lenses, condensators, and quadrupoles allow for focussing of the ion beam, and an additional condensator is used to deflect the beam by 5° in order to eliminate possible neutralized atoms.

Before impacting onto the substrate, a beam-sweep and additional lenses in front of the substrate ensure that the ions arrive perpendicular to its surface and are homogenously distributed over a wider, adjustable area. Furthermore, low energy electrons, which could falsify the measurement of the deposited charge, are filtered out of the beam by a lens at negative voltage. Deceleration of the ions down to the desired energy is realized by setting the ion source to a positive voltage of $U_{acc} = 30$ kV and adjusting the substrate bias with respect to U_{acc}, hence keeping the final ion energy independent of the stability and the actual value of the acceleration voltage. Moreover, the total path length from entering the deceleration

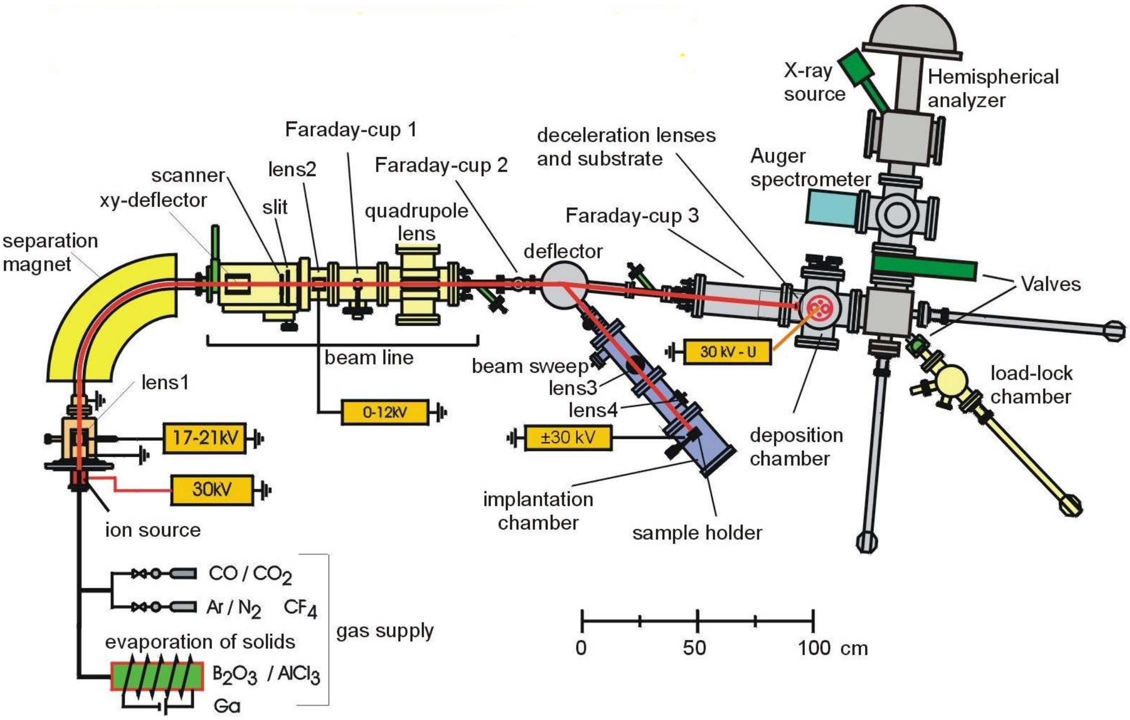

Figure 2.1: Schematic diagram of the MSIBD system ADONIS, with ion source, separation magnet, beam line and deposition chamber. Available *in-vacuo* analysis methods include photoelectron spectroscopy (XPS, UPS), Auger electron spectroscopy (AES), electron energy loss spectroscopy (EELS) as well as field emission energy distribution (FEED).

unit to the substrate surface is only a few centimeters so that losses due to space charge defocusing can be avoided. The number of deposited ions can be precisely determined by measuring the ion charge directly on the substrate. After a certain, adjustable amount of ions (i.e. a specific charge) has been deposited, the separation magnet is automatically switched by a computer to a different magnetic field strength, thus allowing for the deposition of films containing more than one atomic species. Currently, up to four elements can be preset, which makes the growth of even quaternary compounds possible.

In the case of boron nitride film growth, $^{11}B^+$ and $^{14}N^+$ ions are deposited in alternating cycles, where each cycle consists of 10^{15} ions (see figure 2.2a) with a ratio of B:N=1. An ion energy of typically 500 eV then results in an implantation profile with a mean ion range of about 2 nm and a straggle of $\approx$1 nm, while the peak positions of the B and N profiles within one cycle are less than 0.1 nm apart

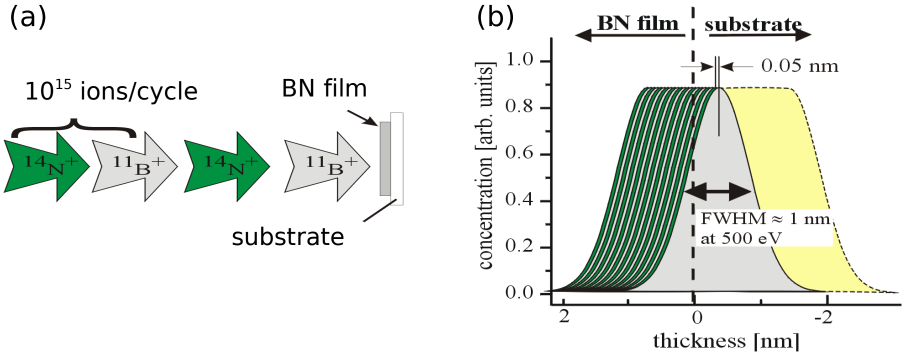

Figure 2.2: Schematic diagram of the deposition process with MSIBD. (a) $^{14}N^+$ and $^{11}B^+$ ions are deposited in alternating cycles, where each cycle consists of typically 10^{15} ions. (b) Deposition of alternating cycles of ions leads to an almost perfect overlap of the implantation profiles, thus to a "quasi-simultaneous" B and N deposition.

(figure 2.2b). Thus, the almost perfect overlap of the implantation profiles ensures a homogenious and stoichiometric film growth, while the film thickness increases by about one monolayer per deposition cycle. Since the synthesis of c-BN films requires the use of elevated temperatures (see section 1.5), the substrate holder can be heated by a tungsten filament, while the temperature is accurately measured using a thermocouple in direct contact with the substrate.

All films investigated in this work have been prepared exclusively on p-type silicon (100) substrates. Prior to deposition, the substrate has been cleaned with Aceton, transferred into the deposition chamber via a load-lock mechanism and preheated to about 250 °C for several hours in order to desorb possible adsorbants from the surface. It was then sputter-cleaned with 1 keV $^{40}Ar^+$ ions for about 10 minutes, which further removes residual contaminants and the customary SiO_2 surface layer. The deposition itself was started directly afterwards with typical ion currents of about 20 μA on an area of 0.5-1.5 cm^2 and deposited charges of 0.15-0.6 C, leading to film thicknesses of about 30-150 nm. The base pressure in the deposition chamber during film growth was with 2×10^{-8} mbar in the ultra-high vacuum (UHV) range.

ADONIS is equipped with several analysis instruments, which allow for an *in-vacuo* characterization of the grown film immediately after deposition. These include two electron guns used for Auger electron spectroscopy (AES) and electron energy loss spectroscopy (EELS). Additionally, x-ray and UV light sources are installed, which are used for photoelectron spectroscopy (XPS and UPS, respectively). The application of these methods for BN thin film characterization is described in the following sections.

2.2 Characterization methods

The characterization of c-BN films is non-trivial and requires the use of several complementary techniques. This is mainly related to the fact that c-BN thin films are usually nanocrystalline, highly-defective and embedded between two sp^2-bonded layers. Therefore, a variety of analysis methods has been applied by many researchers, and those that have been used in this work will be described in the next section.

2.2.1 Fourier transform infrared spectroscopy (FTIR)

Fourier transform infrared spectroscopy (FTIR) is commonly applied for identification and characterization of the phases contained in the bulk of BN films. It offers the advantages of being very fast and non-destructive, and can be done both in reflection and transmission geometry. In general, FTIR is used to determine the frequencies of the infrared-active transverse optical (TO) and longitudinal optical (LO) vibrational modes (i.e. those with a time-varying dipole moment) near the center of the Brillouin zone (i.e. phonon wavevector ≈ 0) in crystalline solids. A similar technique is Raman spectroscopy, which is often used instead of or in addition to FTIR.

c-BN with its zinc-blende structure (two atoms in each primitive unit cell) has a triply degenerate phonon that is both IR- and Raman-active (see figure 2.3a,b). It is split into a TO component at ∼1065 cm^{-1} and a LO component at ∼1340 cm^{-1} due to the bonding ionicity of the crystal [Gie67]. For near-normal incidence, IR spectroscopy gives a peak near the frequency of the TO phonon mode, since for light with a frequency between ω_{TO} and ω_{LO} the real part of the dielectric funtion $\epsilon(\omega)$ becomes negative, hence preventing the light from being transmitted through the lattice. If the film thickness is much smaller than the wavelength of the incident IR light, its intensity decreases exponentially while traveling through the film, and reflection occurs mainly for frequencies near ω_{TO}. This behavior is called

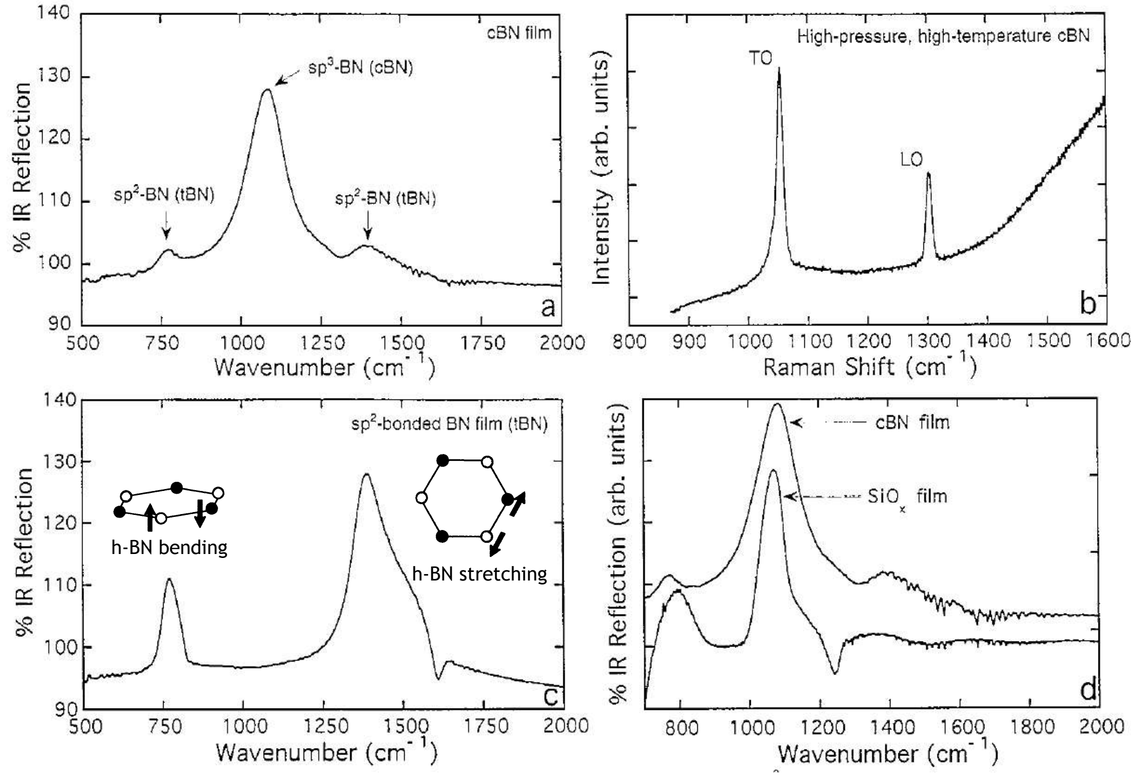

Figure 2.3: Vibrational spectroscopy of BN films. (a) FTIR spectra taken in reflection geometry from a ~100 nm thick c-BN film. (b) Raman spectrum of a single-crystalline c-BN sample, prepared by means of HPHT synthesis. (c) FTIR spectrum taken in reflection geometry from a pure h-BN film. (d) Comparison of FTIR spectra of a mainly c-BN film and a SiO_x sample, taken in reflection geometry (taken from ref. [Mir97a]).

reststrahlen band and produces a peak near ω_{TO} in both reflection- and absorption FTIR spectra.

For h-BN, the two IR-active phonons have TO frequencies at about 780 cm^{-1} and 1380 cm^{-1} (figure 2.3c) [Gei66]. These correspond to a bending of the B-N-B bond *between* the basal planes and stretching of the B-N bond *within* the basal plane, respectively. Very similar frequencies are observered for t-BN as well, only with broadened peaks. Since the vibrational frequencies are sensitive to the bonding type, FTIR is suitable to distinguish between sp^2- and sp^3-bonded phases. However, it is very difficult to discriminate h-BN from r-BN and c-BN from w-BN, respectively. r-BN has two vibration modes, both of which are Raman- and IR-active. These modes are closely related to the IR-active modes of h-BN and have been found by

Raman analysis at essentially the same frequencies as the IR-active modes of h-BN [Liu95]. Therefore, the spectra of r-BN and h-BN are expected to be quite similar. Although w-BN is not very well investigated, phonon frequencies at 1085, 1125 and 1250 cm^{-1} have been reported, with the first one producing the most intense peak [Kes87]. Therefore, it might be possible to distinguish w-BN from c-BN by examining the secondary peaks and 1125 and 1250 cm^{-1}, however, the vibrational properties of w-BN are not well known.

In summary, a reasonably symmetric peak at around 1065 cm^{-1} is the vibrational fingerprint of c-BN, while sp^2-bonded BN can be identified by the two peaks at around 780 and 1380 cm^{-1}, respectively. Broad peaks usually indicate disordered or poorly crystalline phases, since the selection rules that allow only the near-zone-center phonons to be observed break down when the crystallinity is reduced, thus leading to a broadening and shifting of the peaks [Mir97a].

FTIR spectroscopy is not only used to identify the phases present in a BN film, it is also suitable to quantify the c-BN volume fraction, for which it is commonly assumed that

$$\mathrm{c-BN\ volume\ fraction} = \frac{\mathrm{I}_{1065}}{\mathrm{I}_{1065} + \mathrm{I}_{1380}},$$

where I_{1065} and I_{1380} are the normalized reflected or transmitted intensities of the IR absorbances at approximately 1065 and 1380 cm^{-1}, respectively [Kuh95, Ich94]. However, application of this formula gives only a very rough approximation due to the highly complex and defective bond environment present in a c-BN film [Mir97a]. Moreover, the optic properties of h-BN (or sp^2-bonded BN in general) are not isotropic (see figure 2.4). The intensity ratio of both sp^2-BN peaks changes with the orientation of the basal planes, since only those modes with the vibration axis parallel to the electric field vector can be excited by unpolarized IR light in near-normal incidence. As the t-BN interlayer that is present in almost all ion-beam deposited c-BN films has its basal planes perpendicular to the substrate surface, the out-of-plane 780 cm^{-1} mode is enhanced in relation to the in-plane 1380 cm^{-1} mode, and the c-BN content is most often overestimated [Fri93]. Last but not least, there are many examples in the literature where the existence of c-BN has been wrongly concluded because the IR spectra have been misinterpreted, most often because non-BN features near 1065 cm^{-1} have been assigned to c-BN [Mir97a]. For example,

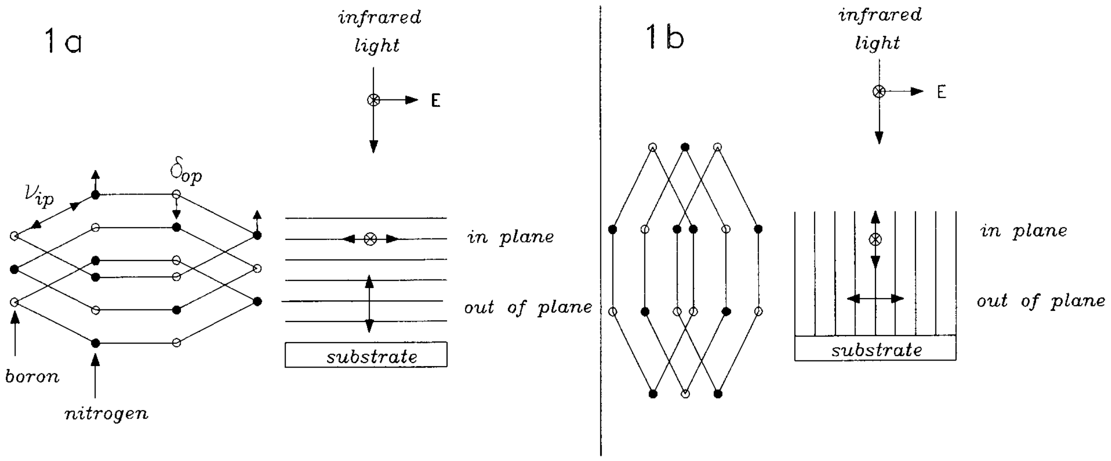

Figure 2.4: Schematic diagram of the IR active modes in hexagonal boron nitride and the relationship of the vibration axis of these modes to the electric field vector of unpolarized light for horizontal and vertical arrangements of the h-BN layers. Only those modes with the vibration axis parallel to the electric field vector are seen (taken from ref. [Kuh95]).

as can be seen from figure 2.3d, SiO_x shows a pronounced IR absorption between about 1100 and 1050 cm^{-1}. As most BN films are deposited on Si substrates, care must be taken when interpreting the IR spectra, especially when the deposition takes place under non-UHV conditions.

Finally, FTIR spectroscopy can also be used to give an estimation of the compressive stress present in a c-BN film, since the FTIR peaks of c-BN films are generally shifted to wavenumbers above the single crystal value of about 1060 cm^{-1} [Mir97a]. If a solid body is subject to mechanical strain, it will react with a decrease of the bond length and thus with a decrease of its volume. Within the harmonic oscillator model commonly used to describe the bonding (i.e. a linear chain of mass points connected by Hookian springs), a decrease in bond length will at first not lead to a change of the resonance frequency. The restoring force is proportional to the amplitude, but not to the initial tension of the spring. Instead, a change of the resonance frequency is due to inharmonic fractions of the lattice potential, which lead to a steeper increase of the potential around the equilibrium state of the charge carriers when the body is subject to compression [Sch02]. Consequently, an increase in pressure results in a shift of the resonance frequency to higher wavenumbers. It is, however, very difficult to exactly quantify the stress value of a c-BN film, again because of the complex bonding environment. Experiments performed by Sanjurjo *et al.* [San83] with c-BN single crystals and *ab initio total energy calculations* by Fahy *et al.* [Fah95, Fah96, Fah97] have revealed a frequency shift of about 4 cm^{-1}/GPa, and those values have been used by many researchers to calculate the compressive stress of c-BN films in the past. However, it has to be mentioned that a frequency shift is not exclusively related to compressive stress. Several other processes can shift the IR peaks, too, including film thickness, the degree of crystallinity, the optical properties of the substrate, and deviations in film stoichiometry [Mir97a]. Therefore, FTIR spectroscopy is often suitable to give a qualitative overview of the stress evolution in c-BN films, but quantitative results obtained with this method have to be taken with care.

2.2.2 Electron energy loss spectroscopy (EELS)

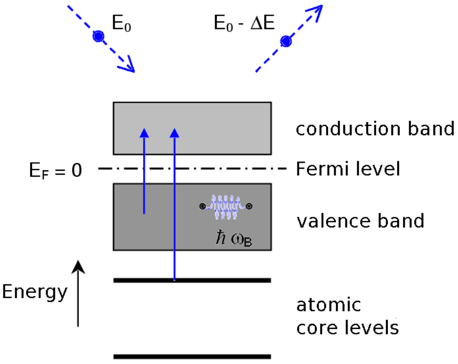

Figure 2.5: Schematic diagram of the excitation mechanisms for EELS. An incident electron either excites a volume plasmon with a frequency ω_B or initiates an interband transition. It is then inelastically back-scattered with a reduced energy (taken from ref. [Nie00]).

EELS has been widely used to discriminate between sp^2- and sp^3-bonded phases in the surface region of BN films [Mir97a, Wid98, Wid99]. In brief, an electron with a defined energy E_0 interacts with the electrons in the solid by either exciting a plasmon (i.e. longitudinal, collective oscillations of the valence electrons) or inducing an interband transition before it is inelastically back-scattered with a reduced energy $E_0 - \Delta E$ (see figure 2.5). According to the free electron gas model, the plasmon frequency is given by $\omega_B^2 = ne^2/m_{\text{eff}}$, where n is the density of the valence electrons in the sample, e the electron charge and m_{eff} the effective electron mass [Kas88]. As n is a function of the mass density (and the valence state), the plasmon frequency can be used to distinguish between sp^2- and sp^3-bonded phases. In the case of the carbon system, the sp^3 bond fraction of amorphous carbon films is approximately determined by a linear interpolation between the plasmon energies of $\hbar\omega_{pl,G} \approx 24$ eV for graphite and $\hbar\omega_{pl,D} \approx 33$ eV for diamond, i.e. $f_{sp^3} \approx (\omega_{pl} - \omega_{pl,G})/(\omega_{pl,D} - \omega_{pl,G})$ [Hof98]. A quantitative determination of the phase contents for BN films is, however, somewhat problematic. It has been shown that the plasmon loss line of c-BN is continuously shifted towards the corresponding line of h-BN by introducing lattice defects, e.g. produced by prolonged ion bombardment [Wid98]. Additionally, as the primary electron energy used is typically in the order of 100-2000 eV, EELS is only capable of examining the surface region of a BN film, since the mean free path of the back-scattered electrons is only a few nanometers at best [Tok85]. Figure 2.6 shows the plasmon energy as a funtion of the primary electron energy (PEE) for a t-BN and a c-BN film, respectively, as measured by EELS in reflection geometry. As the penetration depth of the scattered electrons depends on the PEE, it is thus possible to obtain a depth profile of the plasmon energy value. This clearly shows that the surface of the c-BN is sp^2-bonded (see section 1.4), since the plasmon energies for both the c-BN and the t-BN films are similar for PEE values below approximately 400 eV. For energies exceeding 500 eV, plasmon energies at around 30 eV for c-BN and 25-26 eV for t-BN are measured. This in good agreement with the calculated plasmon energies for both BN polytypes. A comparison of measured and calculated EEL spectra is given in figure 2.7. The theoretical spectrum of c-BN exhibits its most prominent features at 27.3 eV, 32.5 eV, and 38.5 eV (volume plasmons), while the theoretical h-BN spectrum shows a strong peak at 23.7 eV [Wid99]. Compared to the theoretical results, experimentally observed EEL spectra often display wider peaks, which can be shifted by several eV, smearing out all characteristic features.

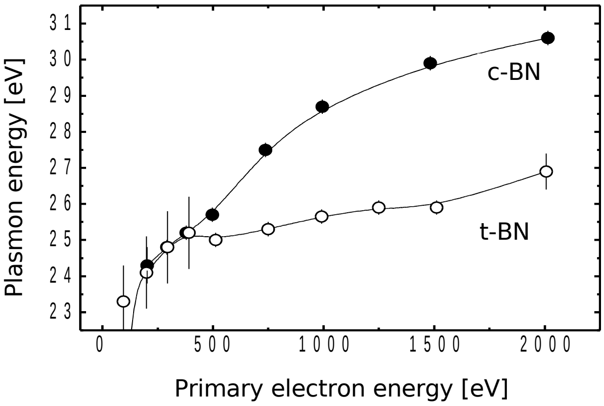

Figure 2.6: Plasmon energy as a function of the primary electron energy for a typical c-BN and a t-BN film as measured by EELS in reflection geometry (taken from ref. [Fel02]).

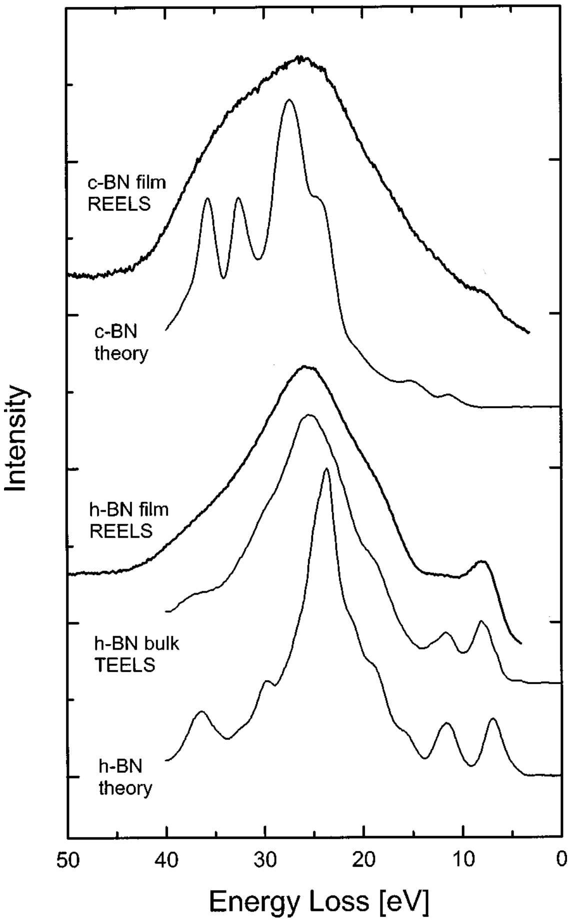

Figure 2.7: Comparison of a measured and calculated EEL spectrum for c-BN (top) and for h-BN (bottom). The spectra have been obtained with a concentric hemispherical analyer (CHA) at 2.5 keV PEE. (from ref. [Wid99]).

This effect is even more pronounced for turbostratic BN or nanocrystalline c-BN films, particularly due to the existing superficial bond disorder.

The possibility of an interband transition in h-BN can also be used to identify the phases present in a BN sample. Since h-BN is sp^2-hybridized, an electron can induce a direct $\pi - \pi^*$ interband transition, which leads to a characteristic energy loss of the back-scattered electron of 6.9 eV or 11.6 eV [Xu91] (see also figure 2.7). As for entirely sp^3-bonded c-BN the $\pi - \pi^*$ transition vanishes, this feature is another well suited fingerprint to distinguish the cubic from the hexagonal phase.

ADONIS is equipped with an electron gun that allows for EELS measurements in reflection geometry with PEE values of 100-3000 eV. The back-scattered electrons are detected in a cylindrical mirror analyzer (CMA) from Perkin-Elmer. Since the energy resolution of the CMA is about $\Delta E/E \approx 0.5\%$ (which leads to a line width of 10 eV at a primary energy of 2 keV), it is not possible to observe h-BN interband transitions. However, the plasmon loss peaks are clearly visible and typically $E_p \approx 30$ eV for c-BN and $E_p \approx 26$ eV for t-BN are measured.

2.2.3 Transmission electron spectroscopy (TEM)

TEM has proven to be very useful for validating phase information and providing detailed microstructural information about boron nitride films. It can be used to determine the phase distribution, morphology, texture, grain size and boundary structure, orientation relationships, and individual fringe spacings and angles within the different layers and at the interfaces inside of the film. However, since the sample preparation for a TEM analysis is quite difficult and time-consuming, only selected samples have been prepared and analyzed by means of TEM. The preperation usually consists of sectioning and sandwiching of the initial sample, which is then mechanically thinned and polished, glued on a supporting Cu washer and ion-milled as the final stage in order to obtain a specimen that is electron-transparent within a region representative of the material to be studied.

Most often, dark-field (DF) images of the sample are obtained by positioning a small objective apperture to select a specific diffracted beam, which is then used to form the image. Segments of the t-BN (0001) ring and the c-BN (111) ring are commonly used (see figure 1.7), which results in regions of high electron intensities that correspond to grains of the phase of interest. The DF technique is therefore very useful to determine the phase distribution, grain size, and morphology of BN films.

High-resolution TEM (HRTEM) is indispensible for the microstructural studies of BN films because of the nanocrystalline dimensions of the ordered regions of both the sp^2- and sp^3-bonded phase. Fringe spacings and angles can either be measured directly from images or in reciprocal space using Fourier transform methods, while the most commonly identified fringes correspond to the c-BN $\{111\}$ planes and the t-BN (0002) planes.

Selected samples were prepared for TEM analysis and have been investigated using a Philips CM200-FEG-UT microscope operating with an acceleration voltage of 200 kV.

2.2.4 Auger electron spectroscopy (AES)

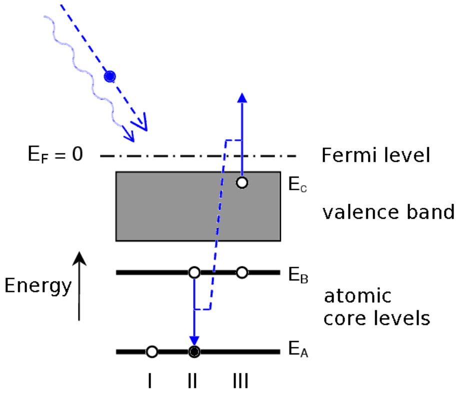

Figure 2.8: Excitation mechanisms for AES. Following the ionisation of a core level A, the created hole is occupied by an electron from level B. The energy is transferred to an electron in level B or C, which then is emitted from the sample (taken from ref. [Nie00]).

AES allows for both a quantitative and qualitative determination of the chemical composition of the surface region of a sample. With this method, characteristic Auger electrons are emitted when the sample is irradiated with energetic electrons, following the ionization of an atomic core level and the subsequent recombination of the created hole with an electron from a higher level (see figure 2.8). The energy is absorbed by an electron, which is then emitted from the sample. The sampling depth is determined by the mean free path of the Auger electrons, which is only in the order of a few atomic layers for primary electron energies of typically 3 keV. Most of the samples investigated in the present work have been analyzed by AES immediately after deposition using the electron gun (PEE=3 keV) and CMA installed at ADONIS. The weighted intensity ratios of the Auger electron peaks have then been used to determine the surface element composition [Dav76]. The AES spectra prove that all BN films are mostly free of contamination with a stoichiometry of B:N=1.

2.2.5 X-ray photoelectron spectroscopy (XPS)

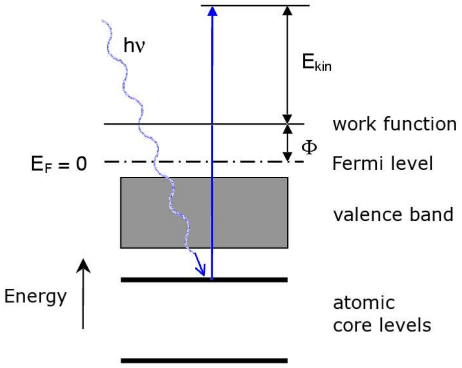

Figure 2.9: XPS excitation diagram. Ionization of an atomic core level occurs due to x-ray photon irradition with energies hν. An electron is then emitted from the sample; its energy is dependent on the photon energy, the binding energy and the work function Φ (taken from ref. [Nie00]).

XPS is a powerful, albeit highly surface-sensitive technique. The sample is irradiated with energetic x-ray photons, which leads to an ionization of an atomic core level (see figure 2.9). This causes the emission of an electron from the sample, whose energy is composed of the photon energy, the binding energy and the work function of the material. The core level spectra obtained by XPS can thus be used for a quantitative analysis of the elemental composition within the 0.3-3 nm sampling depth. Moreover, Auger electrons are also emitted from the sample, and their detection and analysis further enhance a proper identification of the elements present in the film. XPS can also be used to probe the local chemical state, i.e. the ratio of sp^2 to sp^3 bonding, since electrons frequently sustain an energy loss due to plasmon excitation before leaving the material. This makes it possible to measure the plasmon energy of the sample and to conclude on the phase composition.

In this work, XPS has been used in addition to AES and EELS, mainly to analyze the elemental composition of the samples, but also to measure the plasmon frequencies. ADONIS is equipped with an x-ray source emitting Mg-Kα radiation at 1253.6 eV. The electrons are detected in an EA125R concentric hemispherical analyzer (CHA) from Omicron.

2.2.6 Secondary ion mass spectroscopy (SIMS)

SIMS is a very versatile analysis technique and provides a powerful combination of capabilities for molecular detection and trace element determination, imaging and microanalysis, and shallow depth profiling. Usually, a focused ion beam, the primary beam, with an energy up to some keV, is rastered over an area significantly larger than the beam size, in order to form a well-defined sputtered crater with a flat crater bottom. The secondary ions emitted from a small central region of this crater are analysed with respect to their mass. The analysis of an area within the crater bottom can also be performed with a separate analysis beam, and this so-called *dual beam depth profiling* is commonly used in time-of-flight (ToF-SIMS) measurements. ToF-SIMS offers the advantage of being able to detect all masses in parallel, in contrast to the traditional dynamic SIMS instruments, which use sector magnets or quadrupoles for mass separation and can therefore analyze only one mass at a time. Figure 2.10 shows the instrumental layout and corresponding timing diagram for a ToF-SIMS setup operating in dual beam mode. After the very short pulse of the analysis gun, the secondary ions are typically extracted within a few μs and travel through the ToF analyser for a time of up to 100 μs depending on the highest mass to be recorded. During this time, the extraction field can be switched off and a low-energy sputter beam is switched on for the erosion. Therefore, the analysis gun can be operated with the maximum repetition rate without an interruption by the sputtering, which ensures high data rates and optimum detection limits. For insulating samples, a low-energy electron gun is switched on during the sputtering to compensate the charging by the analysis and sputter beam.

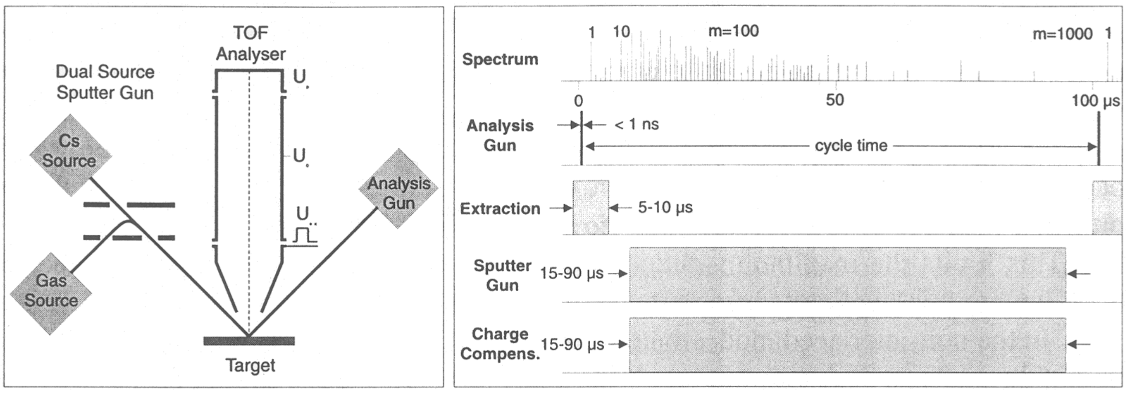

Figure 2.10: Timing diagram and instrumental layout for ToF-SIMS setup in dual beam mode (taken from ref [Nie01]).

In the present work, ToF-SIMS was applied to selected samples in order to measure boron depth profiles (see section 4.5.1) using a TOF-SIMS IV from ION-TOF GmbH. The instrument operates in dual beam mode, with an Ar gun for sputtering (with a voltage of 2 kV and a current of typically 13 nA on an area of 500×500 μm^2) and a Ga beam for analysis (25 kV, 2 pA, 200×200 μm^2).

Chapter 3

Growth regime of ion-beam-deposited c-BN films

In this chapter, the influence of the ion energy on c-BN formation is investigated and discussed. Section 3.1 summarizes the present state of research on boron nitride film growth by means of MSIBD, thereby placing special emphasis on the observed threshold values for ion energy and substrate temperature [Hof95, Hof97, Fel97]. While c-BN can be nucleated only at ion energies in excess of 125 eV and substrate temperatures above 150 °C, its growth regime covers a broader range of both ion energy and substrate temperature [Eyh01, Fel02, Hof02]. In a preliminary study, a high energy threshold above which c-BN growth reverts back to t-BN growth has been found to exist between an ion energy of 5 and 10 keV [Fel02, Eyh03]. However, it will be shown that the data is not unambiguous, which was the driving motivation for the investigations carried out in this work. The experiments are described in section 3.2, and new results on the role of ion energy and substrate temperature on the growth of c-BN films will be presented.

3.1 Summary of foregoing results

3.1.1 Nucleation regime for MSIB deposited c-BN films

In 1992, Kester and Messier found that, for a given temperature, the controlling factor in the resulting BN thin film phase is the momentum transferred into the film per depositing boron atom (see section 1.5.2) [Kes92]. A sharp threshold value of momentum-per-ion exists below which films are hexagonal and above which they are cubic, and this threshold occured at

$$(p/a) = 200\ (\mathrm{eV} \cdot \mathrm{amu})^{1/2}.$$

Furthermore, it was shown that c-BN growth can be accomplished by using only boron vapor and nitrogen ions, i.e. no further particle bombardment (e.g. noble gas ions) is required, although the window of momentum-per-atom values for nitrogen is very narrow. In conformity with these findings, Hofsäß *et al.* demonstrated the successful deposition of c-BN using only energetic B^+ and N^+ ions in an MSIBD process in 1995 [Hof95]. The resulting films exhibit the same layer sequence and microstructure as the ones prepared by other, more complex ion-beam- or plasma-assisted techniques (see sections 1.3 and 1.4), indicating that the nucleation and growth processes are most likely identical.

The first systematic study of c-BN film growth by direct ion beam deposition was done by Feldermann *et al.* in 1997 [Fel97, Hof97]. By using ADONIS (section 2.1), the authors were able to establish an unadulterated phase diagram for boron nitride film growth based on studies on the influence of the ion energy and substrate temperature on the phase formation. Stoichiometric and clean BN films were prepared at temperatures between room temperature (RT) and 350 °C and with ion energies between 25 eV and 2500 eV. The results of subsequent EELS and FTIR phase identification are displayed in figure 3.1 as a function of both ion energy (E_{ion}) and substrate temperature (T_S). In this figure, films containing a significant amount of c-BN are represented by solid circles, whereas entirely sp^2-bonded samples are indicated by hollow symbols. Apparently, sharp thresholds for both ion energy and substrate temperature exist, which seem to be independent on each other. In order to form c-BN, the temperature must be kept above $T_S = 150$ °C while the ion energy needs to be higher than $E_{ion} = 125$ eV at the same time. However, as the deposition conditions were not changed during the entire synthesis process for all films, the thresholds are only valid for c-BN nucleation but not necessarily its continued growth.

When comparing the phase digrams for MISBD and ion-beam- or plasma-assisted-deposition methods, several striking differences can be noticed (see figures 1.12 and 1.13):

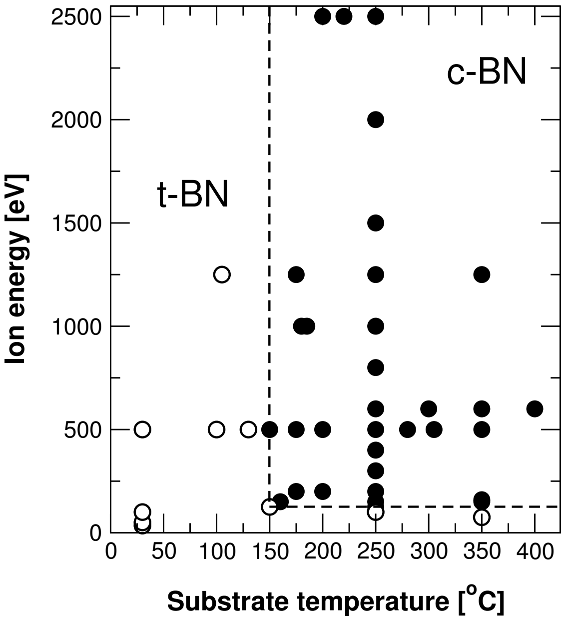

Figure 3.1: c-BN nucleation regime as a function of ion energy and substrate temperature for MSIB deposited BN films. Filled symbols represent films containing c-BN, hollow symbols indicate sp^2-bonded films only (after refs. [Fel97, Hof97, Eyh01]).

1. As a consequence of the direct energy input into the film by both depositing species, the ion-to-atom flux ratio F and the ion mass m_{ion} are fixed. Therefore, the grown phase depends solely on the ion energy and substrate temperature.

2. The threshold values for E_{ion} and T_S are comparatively sharp and no mixed t-BN/c-BN growth regime exists.

3. The observed ion energy threshold value is much lower than the one found in IBAD diagrams. If one defines *ion flux F* as *number of ions per deposited boron atom* (a definition that is commonly used in the literature), a value of $F = 2$ is obtained for MISBD. For $F = 2$, the ion energy threshold for IBAD methods is about 200 eV as can be seen from figure 1.12, i.e. higher than the 125 eV obtained with MSIBD. By using equation 1.4, the latter corresponds to an ion momentum per incident boron atom of about $(p/a) = 110$ (eV·amu)$^{1/2}$, i.e. only about half the value found in IBAD processes. This difference can be accounted for by the more effective energy transfer processes in direct ion beam deposition.

4. In contrast to ion-beam-assisted methods, which use significant fluxes of Ar^+

and N_2^+ ions, a resputter limit does not exist for MISBD. Sputter losses due to ion bombardment can be calculated by the SRIM program [Zie99] and a maximum sputter yield of $s \approx 0.5 - 0.6$ for ion energies between 1 and 3 keV has been obtained [Hof97]. In contrast, IBAD growth takes place at conditions close to the resputter limit, and no net film growth is possible at (p/a) values above 400 $(\mathrm{eV}\cdot\mathrm{amu})^{1/2}$ (section 1.5.2), corresponding to an ion energy of about 600-700 eV (see figure 1.12). Therefore, the corresponding phase diagrams are unavoidably influenced by sputtering processes.

3.1.2 Temperature thresholds for the growth of c-BN films

As already mentioned in section 1.5, the temperature threshold of $T_S = 150$ °C is most likely related to c-BN nucleation, but not necessarily its growth. McCarty *et al.* [McC96] and Ye [Ye00] observed that, once nucleated, the temperature can be decreased to about 80 °C without interrupting c-BN growth. Although Lin *et al.* [Lin90] and Yan *et al.* [Yan95] claimed to have grown c-BN at room temperature, their results are ambiguous, because the actual growth temperature was most likely higher than assumed due to heating from the high-energy, high-density energetic particle bombardment used [Mir97a].

However, by using the MISBD method, Feldermann *et al.* were able to show that c-BN growth is indeed possible at room temperature [Fel99]. With this technique, self-heating of the substrate is negligible because of the comparatively low flux of exclusively light ions. In a first step, a c-BN film was grown at conditions well within the c-BN growth regime, i.e. at a substrate temperature of 200 °C and an ion energy of 500 eV (see figure 3.1). After this, deposition was continued with the same E_{ion}, but at reduced temperatures and without breaking the UHV. One film was grown without interruption, i.e. the heater was switched off and deposition was maintained while the substrate cooled down until eventually RT was reached. For a second film, the heater was again switched off after deposition of the nucleation layer, but the substrate was allowed to cool down to RT before a second layer was grown on top of the first one. The FTIR absorption spectra of these samples are shown in figure 3.2. Both samples grown at RT show no difference in their IR absorption as compared to the reference sample (BN#306), and the spectra are dominated by the strong

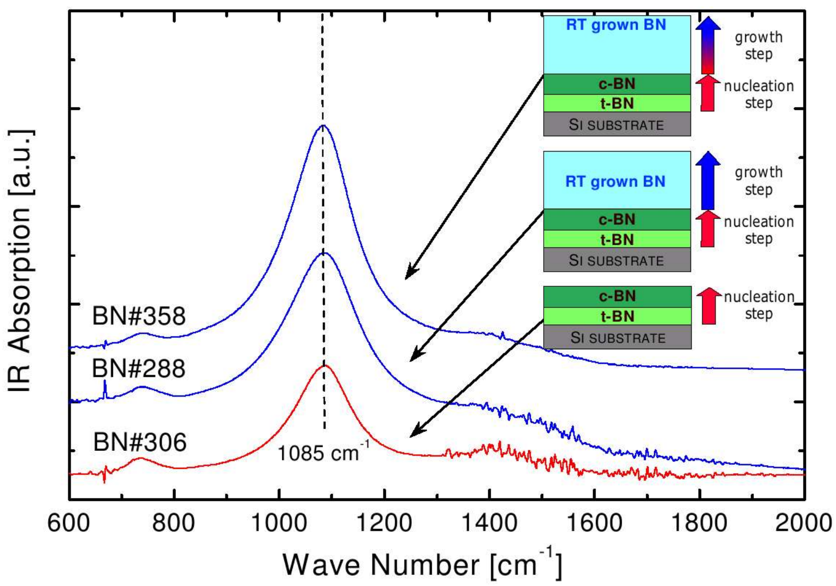

Figure 3.2: FTIR spectra of BN films, grown at a reduced temperature after the initial nucleation step. All films were prepared on Si (100) substrates with E_{ion} = 500 eV. For sample BN#288, the heater was switched off after the nucleation step and deposition was maintained while the substrate cooled down until RT was reached. BN#358 was deposited with a 12h interruption between nucleation and growth step to allow the substrate to cool down to RT. BN#306 is a reference sample, prepared at 200 °C. c-BN growth has continued in all cases (taken from ref. [Fel01]).

c-BN absorption at 1085 cm^{-1}. Although the authors noticed a decrease of about 1-2 eV in the plasmon energies of the RT-grown samples, which was attributed to a temperature-dependent microstructural change within the c-BN layer, the FTIR results clearly indicate continued c-BN growth at RT. This was further confirmed by a careful TEM analysis of the grown films [Fel99, Fel01]. Thus, it has been proven that consecutive growth of the cubic BN phase on a previously nucleated c-BN film is possible at room temperature, i.e. about 125 °C below the nucleation threshold, at least with an ion energy of 500 eV.

3.1.3 Energy thresholds for the growth of c-BN films

Although a threshold for the ion energy exists below which c-BN cannot be nucleated, its growth can be maintained with reduced ion energies. Depending on the

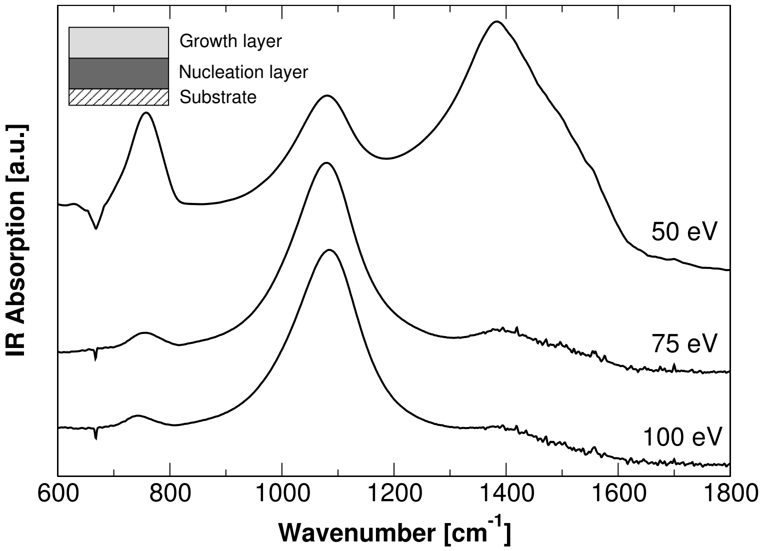

Figure 3.3: IR absorption spectra of BN films, grown with ion energies of 100, 75 and 50 eV, respectively, on a previously nucleated c-BN sample. Cubic phase formation has continued for ion energies down to 75 eV, but $E_{ion} = 50$ eV results in t-BN growth only (after ref. [Eyh03]).

deposition technique used, an ion energy[1] of $70 - 200$ eV is necessary to initiate cubic phase formation; for MSIBD this threshold is $E_{ion} = 125$ eV. In 1995, McKenzie *et al.* observed that the ion energy can be significantly lowered after c-BN nucleation without interrupting its growth [McK95]. This was later confirmed by other researchers [Sch96, Ama97, Lit97, Hah97, Khi01]. As MSIBD is the only technique for which the ion energy is precisely adjustable and well defined, it was used in the framework of my diploma thesis to establish the low energy growth limit for c-BN [Eyh01]. After deposition of an initial nucleation layer at conditions that are well within the c-BN nucleation regime ($T_S = 250$ °C, $E_{ion} = 500$ eV), a second BN layer was grown on top of the first one while keeping the substrate temperature unchanged. The ion energy was reduced to 100, 75 and 50 eV, respectively, and the samples were characterized with EELS and FTIR. The results of the FTIR measurements are shown in figure 3.3. Apparently, c-BN growth has continued even

---

[1] for most ion-beam- and plasma-assisted-depositon methods it is often assumed that the ion energy is given by the applied bias voltage, i.e. $E_{ion} = e \cdot U_{bias}$. However, as those techniques usually work with a mixture of Ar/N ions and evaporated B atoms, the film is bombarded with a variety of singly or doubly charged ions, clusters and molecules as well as thermal boron atoms and clusters. Thus, the actual ion energy is difficult to quantify.

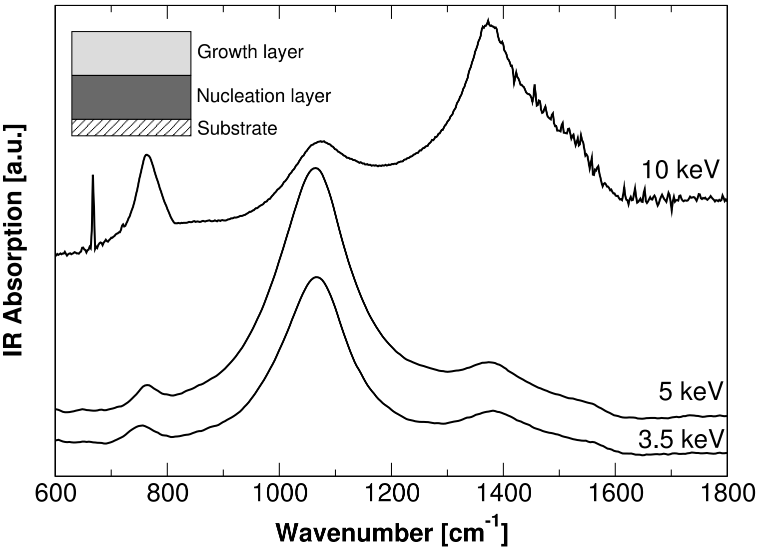

Figure 3.4: FTIR spectra of BN films, deposited with energies of 3.5, 5 and 10 keV, respectively, on a previously grown c-BN sample. Using an energy of 5 keV does not interrupt cubic phase formation, but E_{ion} = 10 keV resulted in t-BN growth in this case (after ref. [Eyh03]).

with an ion energy of 75 eV, as for this sample the corresponding IR spectrum is still dominated by the strong c-BN absorption at around 1085 cm^{-1}. A further decrease of the energy down to 50 eV interrupts cubic phase formation and results in sp^2-bonded BN growth only. Therefore, the low energy growth threshold for c-BN films is between 75 and 50 eV, i.e. about 60 eV below the nucleation threshold.

Since the energy regime above approx. 1 keV is not accessible with IBAD methods due to the resputter limit, little is known about the influence of high ion energies on both nucleation and growth of c-BN thin films. In fact, MSIBD is the only technique available that allows for examining boron nitride phase formation as a function of the ion energy above $E_{ion} \approx 1$ keV, as deposition with this method is not hindered by resputtering (see section 3.1.1). Consequently, Hofsäß and coworkers studied BN growth with ion energies exceeding the previously used values by using the same approach as described above [Eyh01, Fel01, Hof02]: a c-BN film was prepared with E_{ion} = 600 eV, T_S = 250 °C, and a total deposited charge of $Q = 0.2$ C, leading to a film thickness of about 40 nm. A second BN layer was then deposited on the first one, with unchanged substrate temperature but increased ion

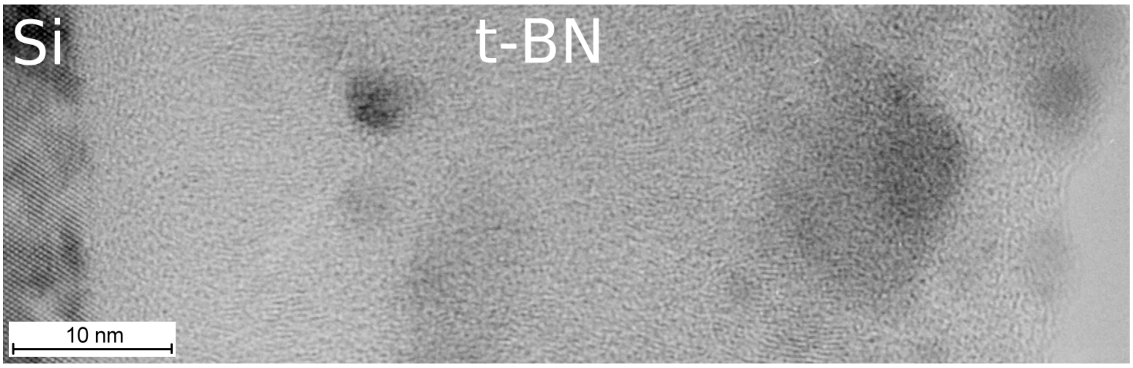

Figure 3.5: TEM micrograph showing the entire cross-section of a BN film, grown with an ion energy of 10 keV on a c-BN substrate. The entire sample contains exclusively textured t-BN (after refs. [Eyh01, Fel02]).

energies of 3.5, 5, and 10 keV, respectively. The FTIR results are displayed in figure 3.4. While it is obvious that deposition with 3.5 keV and 5 keV did not interrupt c-BN growth (which was also confirmed by a TEM analysis), the use of 10 keV ion energy clearly led to t-BN growth. The c-BN absorption peak at 1080 cm^{-1} is very weak, while the strong t-BN peaks at 1380 and 780 cm^{-1} dominate the spectrum. Moreover, as revealed by TEM (figure 3.5), deposition with 10 keV has led to a complete transformation of the sp^3-bonded nucleation layer into sp^2-bonded t-BN in some cases. It was speculated that the initial layer was probably not thick enough, since an SRIM calculation indicated a maximum range of 10 keV B$^+$ and N$^+$ ions larger than the thickness of the sp^3-bonded part of the nucleation layer. Thus, it is plausible that a substantial amount of ions came to rest beyond the c-BN layer after the growth step was started, which would then resemble a c-BN nucleation and not growth process.

The existing data were then summarized into the diagrams presented in figure 3.6, which display the parameter spaces for c-BN nucleation and its consecutive growth. The initial formation of c-BN requires the use of an ion energy of at least 125 eV and a substrate temperature of 150 °C. These thresholds are comparatively sharp and seem to be independent on each other. The energy regime extends to 2500 eV, however, this may not be the actual limit. As reported by Feldermann, the thickness of the t-BN interlayer increases with increasing ion energy, so that the c-BN nucleation process is delayed more and more [Fel01]. Thus, ion energies above 2500 eV would require the preparation of sufficiently thick samples in order to be able to detect c-BN within the film.

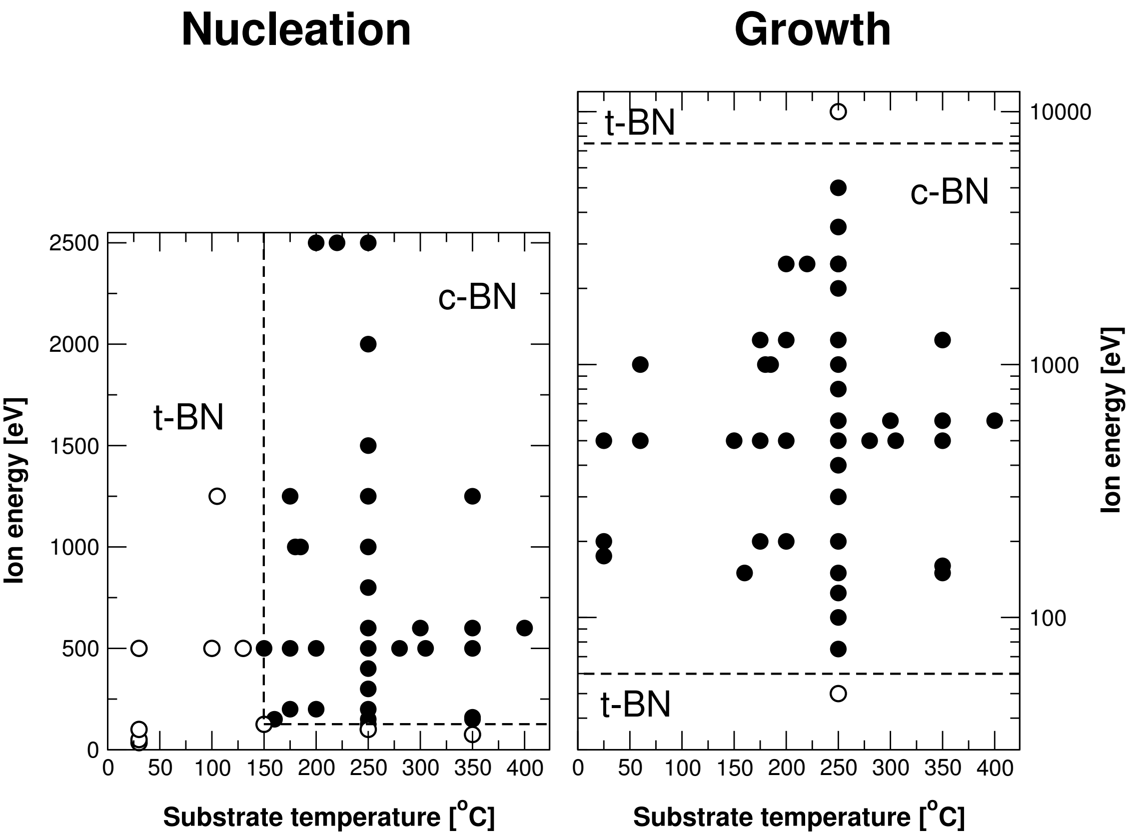

Figure 3.6: Deposition parameter spaces for nucleation and growth of ion-beam-deposited c-BN films. Solid data points represent samples that have been found to contain c-BN, hollow symbols indicate sp^2-bonded films only. Nucleation of c-BN is possible with ion energies above 125 eV and substrate temperatures exceeding 150 °C (left diagram). For consecutive growth of c-BN, the ion energy must be kept between 60 eV and around 7 keV, while the growth process seems to be temperature-independent (after refs. [Eyh01, Fel02]).

C-BN growth on the other hand seems to be mostly temperature-independent, since it is possible between RT and about 1100 °C, above which the films disintegrate and evaporate from the substrate [Ron97a]. The ion energy threshold value found for c-BN nucleation is not valid for its growth, instead, a new low-energy threshold exists between 50 and 75 eV, below which c-BN growth reverts back to t-BN growth. Finally, a high-energy threshold may exist between 5 and 10 keV, although, as mentioned previously, the data is not unambiguous.

3.2 c-BN growth by high-energy deposition

3.2.1 t-BN/c-BN interface instability

In order to clarify whether the transformation back to t-BN growth with 10 keV ion energy as described in the last section is a result of the thin c-BN nucleation layer, the following experiment was conducted: two c-BN films were grown on p-type Si (100) with an ion energy of 500 eV and a substrate temperature of 250 °C. For the first sample, the total deposited charge was $Q = 0.2$ C, which results in a film thickness of about 50 nm, including an approx. 15-20 nm thick t-BN interlayer. For the second sample, the charge was increased to $Q = 0.3$ C, resulting in a film thickness of about 75 nm. After this, the ion energy was set to 10 keV for both B^+ and N^+ ions while the substrate temperature was kept constant at 250 °C, and an additional 0.2 C was deposited onto the initial nucleation layer. Both samples were kept under UHV conditions during the whole deposition process.

The results of the following FTIR analysis is displayed in figure 3.7. It is obvious that 10 keV B^+/N^+ irradiation has led to t-BN growth in sample a, since the two absorption lines at about 766 and 1380 cm^{-1}, respectively, are very strong as compared to the c-BN peak at 1077 cm^{-1}. Sample b, however, shows a pronounced c-BN reststrahlen absorption at 1066 cm^{-1}.

An estimate of the B^+ and N^+ mean ion range in c-BN by the SRIM program [Zie99] using the input parameters proposed in ref. [Hof98] yields 22 nm for B^+ and 16 nm for N^+ ions, with a straggling of 8 and 6 nm, respectively. As a consequence of the ion lens configuration and the focusing of the ion beam, thin films deposited with ADONIS customarily exhibit a thicker brim region and a thinner central area. Hence, it is reasonable that the c-BN layer thickness in the latter region was smaller than the ion range of 10 keV B^+ and N^+ ions and a substantial amount of ions came to rest beyond the c-BN layer after the growth step was started. This situation is indicated in the schematic diagram in figure 3.7 and is further supported by the fact that the TEM image displayed in figure 3.5 was obtained from the central region of the sample and shows no indication of c-BN at all, whereas the FTIR spectrum clearly exhibits a c-BN absorption. Since the infrared beam typically analyzes a sample area of about 30 mm^2, the c-BN signal in the spectrum most likely originates from the initial nucleation layer that has not been completely transformed into t-

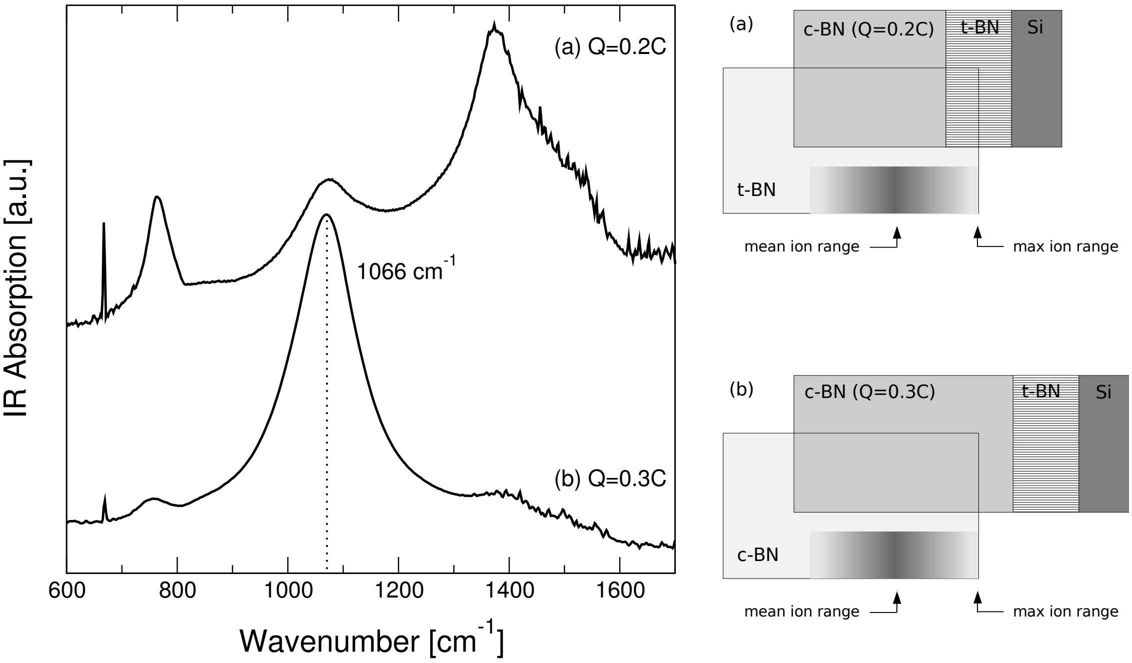

Figure 3.7: FTIR spectra of two BN films that were grown with 10 keV B^+ and N^+ ions at $T_S = 250$ °C on a previously nucleated c-BN film. For sample *a*, the total deposited charge of the nucleation layer was $Q = 0.2$ C, which resulted in a film thickness of about 50 nm, including an approximately 20 nm thick t-BN interlayer. High-energy deposition has led to t-BN growth only, most likely because the maximum ion range of 10 keV B^+ and N^+ ions is larger than the thickness of the c-BN nucleation layer, as indicated by the schematic on the right. Cubic phase formation could be maintained by increasing the thickness of the c-BN initial layer to about 75 nm (corresponding to a charge of $Q = 0.3$ C), i.e. larger than the penetration depth of the high-energy ions (sample *b*).

BN at the thicker brim region of the film. On the other hand, the nucleation layer of the second sample was thicker than the ion range over the entire area, and no transformation to t-BN growth has occured. Moreover, continued c-BN growth in this case is further supported by examining the position of the reststrahlen peak. Its maximum is positioned at about 1066 cm^{-1}, i.e. about 11 wavenumbers below the value of 1077 cm^{-1} obtained for sample *a*. The latter is usually observed for c-BN films deposited with ion energies of 500-800 eV, thus, it is quite safe to assume that this peak is caused by remnants of the initial nucleation layer. Since the peak position is related to the internal stress present in the film (see section 2.2.1), one can also conclude that deposition with high ion energies not only leads to cubic phase formation, but also allows for growth of c-BN films with relatively low stress values.

Additionally, the peak width, which has been regarded as an indicator for the grain size and structural defect density within c-BN films [Lit97], is comparable to the ones observed at lower energies and similar substrate temperatures (full width at half maximum (FWHM) $\approx$ 130 cm^{-1}), indicating that the crystalline quality does not deteriorate by using 10 keV ions.

In summary, c-BN growth on a previously nucleated c-BN film is indeed possible with an ion energy of 10 keV and a substrate temperature of 250 °C. Furthermore, irradiation of the t-BN/c-BN interface must be avoided, as this would most likely lead to a complete transformation of the entire c-BN film into sp^2-bonded BN. An analysis of the FTIR spectrum revealed a shift of the c-BN reststrahlen absorption to lower wavenumbers, while the peak width remains nearly unchanged. Hence, the film exhibits lower stress values but a similar crystalline structure as compared to samples prepared with lower energies.

Successful c-BN growth with an ion energy of 10 keV has not been reported before, and furthermore, none of the existing models for c-BN growth is able to explain cubic phase formation with energies exceeding about 5 keV (see section 4). Consequently, the mechanisms leading to c-BN growth at high energies as well as the actual energy limit is unknown. The aim of the work presented in this chapter is therefore directed to the investigation of the influence of the ion energy on boron nitride phase formation, which will eventually give more insight into the processes leading to c-BN growth.

3.2.2 Sample preparation

All films investigated in the present work have been prepared using the two-step approach as described above (see figure 3.8). P-type silicon (100) has been used as substrate, which was cleaned with Aceton and sputtered with 1 keV $^{40}Ar^+$ ions for about 10 minutes immediately before the deposition was started. This has proven to be an effective way to remove residual contaminants and the customary SiO_2 surface layer. A c-BN film was then grown by using B^+ and N^+ ion energies of 500 eV and a substrate temperature of 250 °C. These settings are well within the c-BN nucleation regime (section 3.1.1), and furthermore, using an energy of 500 eV allows for the growth of c-BN films with comparatively low stress [Hof97]. Although

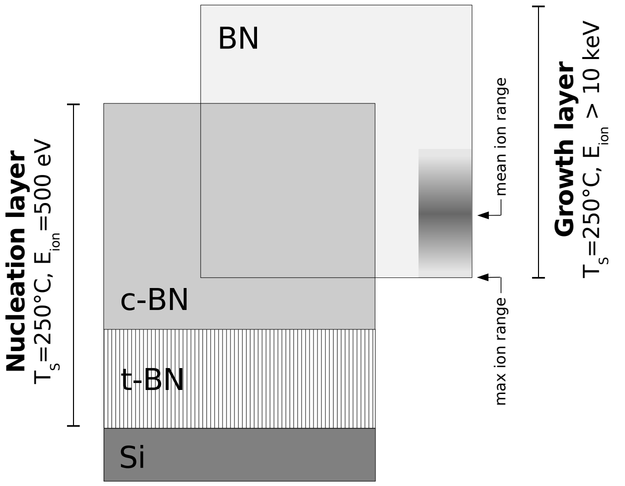

Figure 3.8: Schematic diagram of the BN growth sequence. After the formation of a sufficiently thick nucleation layer (prepared at E_{ion}=500 eV, T_S=250 °C), the ion energy was increased while the substrate temperature was kept constant. The thickness of the initial c-BN layer was larger than the maximum ion range of the high energy B^+ and N^+ ions.

lower ion energies support the onset of c-BN nucleation, i.e. the thickness of the t-BN interlayer decreases with decreasing ion energy [Fel01], they also lead to high internal stress values that limit the achievable film thickness to only about 100 nm [Hof97]. An ion energy of 500 eV has proven to allow for the growth of 100-150 nm thick c-BN films that show no sign of delamination. The thickness of the initial c-BN layer is of major importance regarding the following growth step: While keeping the substrate temperature unchanged at 250 °C, the ion energy was increased to values of up to 43 keV and an additional charge of $Q = 0.2 - 0.4$ C was deposited on an area of 2 cm^2, thereby increasing the total film thickness by about 20-35 nm. This already includes sputter losses, which are about 40% as calculated by SRIM. As the t-BN/c-BN interface was found to be unstable upon ion irradiation, the c-BN nucleation layer thickness has to be larger than the maximum ion range of B^+ and N^+ ions used during the growth step. 43 keV $^{14}N^+$ ions have a maximum range of about 80 nm in c-BN (as calculated by SRIM), thus, the initial nucleation layer thickness has to be greater than 100 nm, which already includes an about 15 nm thick t-BN interlayer. Therefore, the deposited charge for the nucleation layer has been carefully adjusted in order to ensure that its thickness notably exceeds the ion range and the t-BN/c-BN interface is not bombarded.

Deposition during the growth step was carried out without breaking the vacuum and the samples were kept under UHV conditions ($p \approx 2 \times 10^{-8}$ mbar) all the time. Most films were characterized *in-vacuo* by AES and EELS and all samples were analyzed *ex-situ* by FTIR spectroscopy in transmission mode. Additionally,

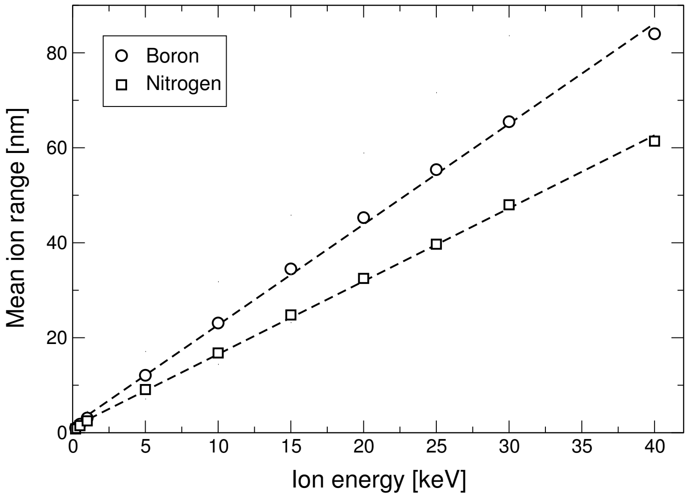

Figure 3.9: Projected mean range of $^{11}B^+$ and $^{14}N^+$ ions in c-BN as calculated by the SRIM program package. At a given energy the N implantation profile has its maximum closer to the surface as compared to B, which is a consequence of the larger atomic mass of N with respect to B. The straggling (i.e. the width of the implantation profile) has also been calculated by SRIM, but has not been included in the figure for the sake of simplicity. However, for 40 keV, it can be as large as 22 nm for boron and 17 nm for nitrogen ions, respectively.

selected samples were also examined by conventional and high-resolution TEM after cross-sections were prepared using the standard sandwich technique.

When using ion energies above approximately 5 keV, an important effect has to be taken into consideration. Formation of c-BN is known to be very sensitive on stoichiometric changes, i.e. the particles incorporated in the film have to fulfill the stoichiometry condition B:N≈1 [Mir97a, Kul03], otherwise the c-BN content in the sample will decrease dramatically until eventually only t-BN films are obtained. As with MSIBD the energetic species are deposited in alternating cycles, care has to be taken in order to (a) provide a stoichiometry of B^+:N^+=1 and (b) ensure a sufficient overlap of the N and B implantation profiles. The ion ranges of $^{11}B^+$ and $^{14}N^+$ in c-BN differ because of their different masses, i.e. when using the same energy for both species, the N depth profile will have its maximum closer to the surface as compared to B. The ranges of $^{11}B^+$ and $^{14}N^+$ in c-BN can be calculated by using the SRIM program package and are displayed in figure 3.9. Both data sets show a linear behavior with respect to the ion energy, but due to

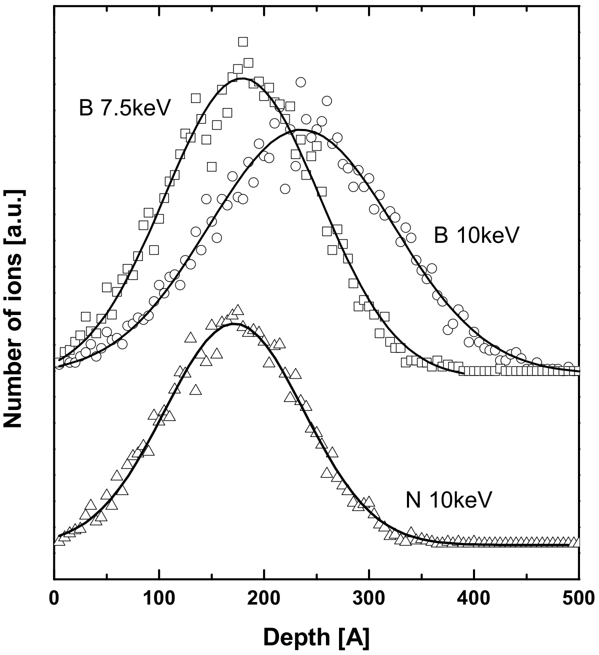

Figure 3.10: Projected range of B^+ and N^+ ions in c-BN as calculated by SRIM (assuming a target density of 3.5 g/cm^3). As a consequence of their different atomic masses, the maxima of the depth profiles of B^+ and N^+ ions are about 6 nm apart when using an ion energy of 10 keV. To ensure overlapping implantation profiles and stoichiometric film growth with MSIBD, the energies for B and N have to be adjusted. In this case, using 7.5 keV B^+ and 10 keV N^+ ions would produce an almost perfect overlap.

their mass difference the B^+ range exhibit a steeper increase with increasing ion energy. Therefore, using the same high energy for both boron and nitrogen ions would result in a significant difference between their mean range and most likely to a non-stoichiometric film growth. Investigations on the influence of the ion energy on BN phase formation could then be severely hampered due to stoichiometric effects. It has to be mentioned that the data displayed in figure 3.9 only represents the *mean* ion range, i.e. the maximum of the depth profile. SRIM is also able to calculate the straggling, i.e. the width of the profile, however, this has not been included in the figure for simplicity reasons. An example for this is given in figure 3.10. When using an ion energy of 10 keV, the mean ion range is about 23 nm for $^{11}B^+$ and 17 nm for $^{14}N^+$ ions, respectively. Although this results in a difference of about 6 nm, deposition with 10 keV B^+ and N^+ ions has obviously not led to stoichiometric problems, since successful c-BN growth with this energy has been confirmed. This is most likely a consequence of a substantial ion straggling, which is about 9 nm for the case of B^+, and 6 nm for N^+ ions, respectively, which apparently still results in a sufficient overlap of the profiles.

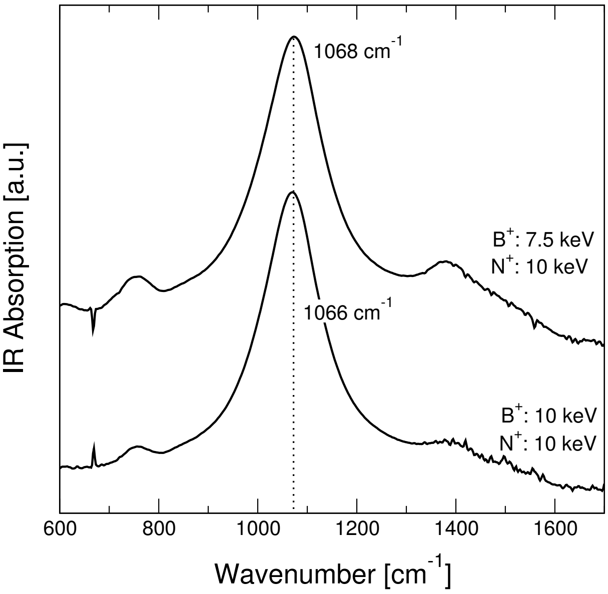

Figure 3.11: IR absorption spectra of two c-BN films, grown with 10 keV ion energy for both B$^+$ and N$^+$ (bottom) and adjusted energies of 7.5 keV and 10 keV, respectively (top).

ADONIS allows for an independent setting of the ion energy for each energetic species participating in the deposition process. Thus, by using a $^{14}N^+$ ion energy of 10 keV, one can adjust the $^{11}B^+$ energy to 7.5 keV, which would then result in a perfect overlap of the implantation profiles as shown in figure 3.10. In order to verfiy the SRIM calculations, a BN sample was prepared in this manner, i.e. by reducing the B ion energy to 7.5 keV but keeping all other deposition parameters identical to those that were used to grow a c-BN film with 10 keV (as described above). The IR absorption spectrum of the sample is shown in figure 3.11 (top). Although the c-BN peak exhibts a slight shift to higher wavenumbers and also a slightly increased peak width as compared to the ”pure” 10 keV sample (bottom), the c-BN content remains high (i.e. approx. $87 \pm 4\%$). Therefore, c-BN has continued to grow with a reduced B$^+$ ion energy, however, as indicated before, the adjustment is obviously not necessary when using an ion energy of 10 keV and below. It will most likely become eminent when using higher ion energies, though, and for the following experiments the ion energies for B$^+$ and N$^+$ have been adjusted according to the SRIM calculations.

3.2.3 Results and Discussion

AES measurements performed *in-vacuo* after deposition was finished confirmed stoichiometric film growth with a ratio of B:N≈1. The results of the *ex-situ* FTIR analysis of the films grown with 10 keV, 10 and 13 keV, and 15 and 20 keV B^+ and N^+ ions, respectively, are displayed in figure 3.12. All spectra exhibit the distinctive c-BN reststrahlen absorption at approximately 1068 cm^{-1} and the two t-BN TO modes at around 760 and 1380 cm^{-1}. Furthermore, the c-BN content of about 88±3% for all samples is higher than would be expected for t-BN growth on the previously nucleated c-BN film. The peak positions as well as peak widths are comparable for all samples and indicate the formation of a cubic phase with relatively low internal stress values and good crystalline quality. Thus, the FTIR measurements provide strong evidence that c-BN film growth is possible even with 15 keV B^+ and 20 keV N^+ ions.

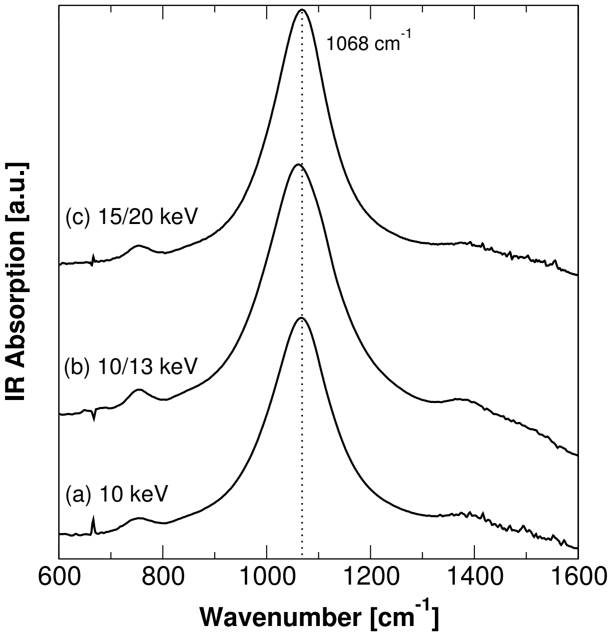

Figure 3.12: FTIR absorption spectra of BN films, grown with (a) 10 keV, (b) 10/13 keV, and (c) 15/20 keV on a c-BN substrate. The ion energies have been adjusted according to SRIM calculations to ensure a perfect overlap of the B and N implantation profiles. Graph labels have to be read as B^+/N^+ ion energy. c-BN growth has continued in all cases.

A TEM analysis performed on the 15/20 keV sample further supports the FTIR

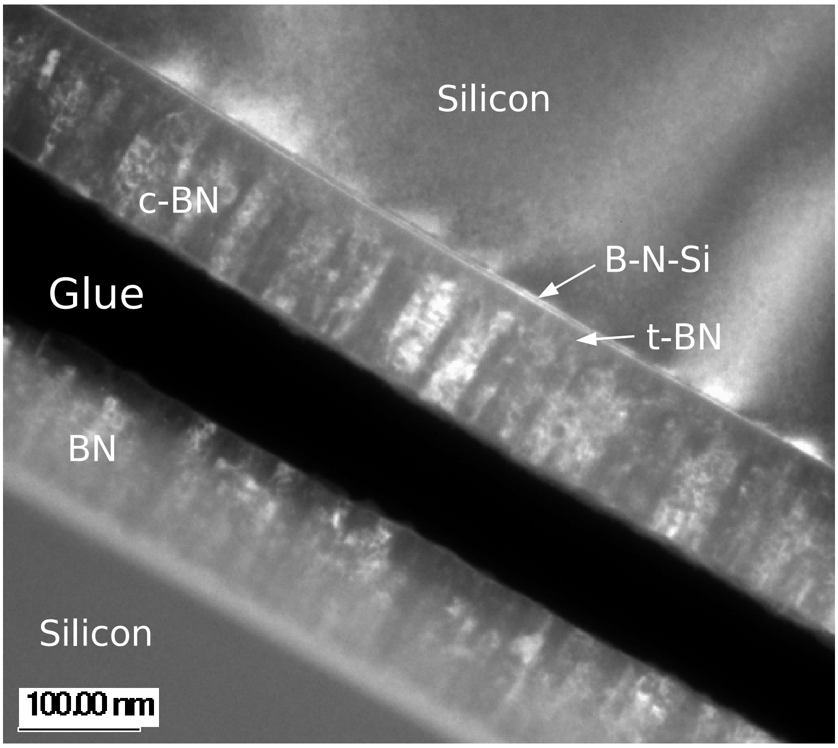

Figure 3.13: TEM dark-field image of a c-BN sample, grown with ion energies of 15 keV for B^+ and 20 keV for N^+ ions, respectively. The typical BN layer sequence is clearly visible. The silicon substrate is followed by a thin amorphous layer, which most likely contains B,N, and Si atoms. An approx. 100 nm thick c-BN film has formed on an about 15 nm thick t-BN layer. Columnar growth is clearly visible, with c-BN grains extending from their nucleation site at the t-BN layer to the surface.

results and confirms successful c-BN growth with high ion energies. A dark-field TEM image is displayed in figure 3.13 and has been obtained by selecting the c-BN (111) reflections. It shows the typical layer sequence where the silicon substrate is followed by a thin amorphous layer that presumably consists of B,N, and Si atoms as a consequence of the ion impact. The about 15 nm thick t-BN layer is then followed by an approx. 100 nm thick c-BN film. The individual c-BN crystallites are clearly visible, which in some case exhibit lateral diameters of about 30 nm and are extending from their nucleation site up to the surface. Considering the ion range of 15 keV B^+ and 20 keV N^+ ions, which is about 30 nm according to SRIM calculations, there is no indication of an interruption of c-BN growth; no interface can be found between the c-BN formed during the nucleation and growth steps, which is indistinguishable.

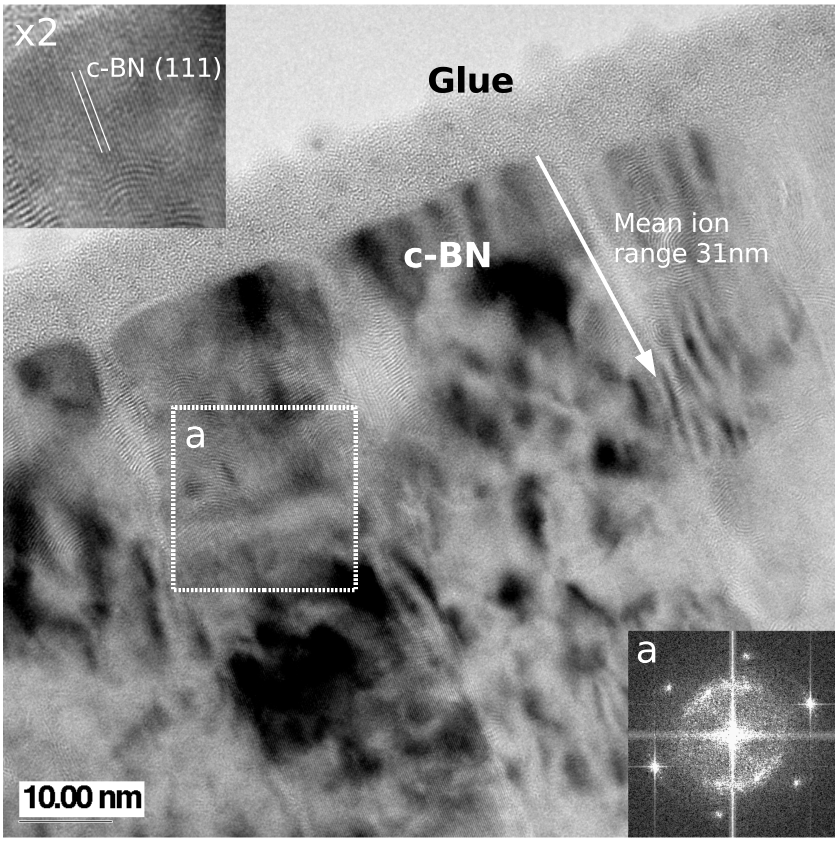

Figure 3.14: HRTEM image showing the upper part of the c-BN sample displayed in figure 3.13. Cubic BN grains with lateral diameters of about 20 nm are extending up to the surface, and their (111) plains are aligned roughly perpendicular to the substrate surface (see inset in the upper left). Sp^2-bonded BN is also visible between the grains, thus, the Fourier transform image (a) shows the pronounced c-BN (111) reflections as well as diffuse and broad t-BN (0002) spots. The mean ion range of 15 keV B^+ and 20 keV N^+ ions is indicated by the arrow.

A detailed high-resolution TEM picture is displayed in figure 3.14. It shows the upper part of the 15/20 keV sample and again confirms successful c-BN growth. The c-BN crystallites have grown up to the surface, and are not covered with the typical sp^2-bonded BN layer that is usually observed on ion-beam-deposited c-BN films. The absence of this surface layer has been reported previously on a c-BN sample that was grown with an ion energy of 5 keV [Eyh01, Fel01]. It is not clear whether this feature is due to structural failure of the mechanically unstable, soft BN phase during the TEM preperation procedure or a consequence of the high-energy growth process. However, there are some indications that point to the latter. For low ion energies (i.e. around 500 eV), the actual c-BN formation can be regarded as a sub-surface process, since the ion ranges of B^+ and N^+ are usually only about 1 nm. In the view of the cylindrical spike model for the formation of diamond-like phases (which will be discussed in detail in section 4.4), the evolution of a dense sp^3-bonded phase is related to a transient densification of the film material during successive ion bombardment, followed by a recrystallization process that is determined by the surrounding bond configuration [Hof98]. However, consecutive ion bombardment cannot lead to a densification beyond the c-BN bulk density, and excessive atoms will diffuse out to grain boundaries or to the surface. The customary sp^2-bonded terminal layer is therefore a consequence of the ion bombardment, and is successively transformed into sp^3-bonded BN upon ion impact. This explanation is indeed plausible, considering the fact that the thickness of this layer corresponds well to the ion range. In the case of high ion energies (i.e. 15/20 keV in this case), the ion range is in the order of 30 nm, which then resembles a volume growth rather than a sub-surface growth process. A diffusion of the implanted atoms to the surface is unlikely, thus, excessive atoms will most likely move to other sinks, i.e. grain boundaries. Agglomaration of sp^2-bonded material is indeed visible between the c-BN grains in figure 3.14, whereas a formation of sp^2-bonded BN at the surface is probably hampered due to sputtering effects. Furthermore, significant amounts of t-BN are only visible in the upper 30-35 nm of the film, which further supports this assumption when taking the ion range of 15/20 keV B^+/N^+ ions into account (indicated by the arrow in figure 3.14). An EELS measurement performed directly after deposition has revealed a plasmon energy of $E_p \approx 27 - 28$ eV. Although this value is about 1-2 eV higher than one would expect for a pure t-BN film, it is also lower than the plasmon energies found for cubic BN (around 30 eV). Considering the presence of both sp^2- and sp^3-bonded BN in the surface region of the film, the obtained E_p value can be regarded as an average between the c-BN and t-BN plasmon energies. Consequently, electron energy loss spectroscopy can neither be used for a reliable bulk phase identification nor to conclude on the existence of a purely sp^2-bonded BN surface layer.

A closer look at the c-BN crystallites shows that they are highly ordered, i.e. the c-BN (111) planes are aligned roughly perpendicular to the substrate surface. The Fourier transform inset shows the distinct and sharp c-BN reflections, which have

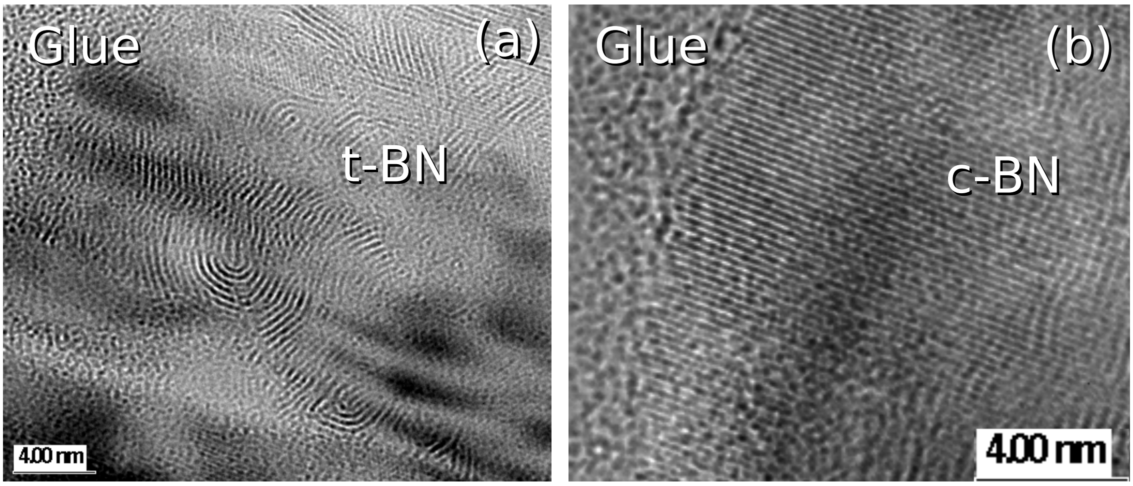

Figure 3.15: Magnified HRTEM images of a c-BN sample, grown with 15 keV B^+ and 20 keV N^+ ions. (a) t-BN formation can be observed between the c-BN grains, with no apparent orientation of the (0002) planes. (b) the individual c-BN grains consist of highly aligned crystallites, which have their (111) planes roughly perpendicular to the substrate surface.

a d spacing of 2.09 ± 0.05 Å and can therefore be associated with the cubic (111) planes. In addition, the broad and diffuse t-BN (0002) reflections are also visible ($d \approx 3.5 \pm 0.2$ Å) and indicate the presence of disordered sp^2-bonded BN between the c-BN grains. Figure 3.15 displays magnified HRTEM images of (a) an sp^2-bonded region between two c-BN crystallites and (b) a representative area of a c-BN crystallite. The t-BN planes show no apparent orientation and are highly disordered, whereas the c-BN (111) planes are perpendicular to the substrate surface and therefore seem to have inherited the orientation from their initial nucleation site at the t-BN/c-BN interface.

Since cubic boron nitride growth has proven to be possible even with 15 keV B^+ and 20 keV N^+ ions, the ion energy was increased further to values of 20 and 27 keV, and 31 and 43 keV for B^+ and N^+, respectively. In order to be able to independently examine the nucleation and growth layer, a motorized shutter was installed at ADONIS. It is positioned approx. 30 cm in front of the substrate and was used after deposition of the initial nucleation layer to cover one half of the sample. Deposition of the growth layer was then continued on the uncovered half

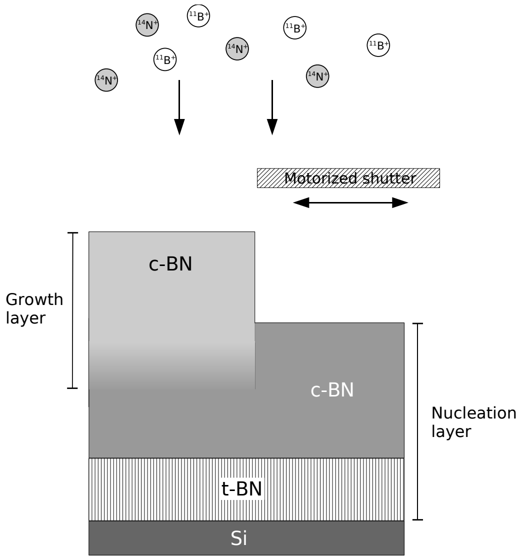

Figure 3.16: Schematic diagram of high-energy BN film growth. After deposition of the initial nucleation layer, a motorized shutter was used to cover one half of the sample. Deposition of the growth layer was then continued on the uncovered half of the film.

of the film (see figure 3.16). This way, *in-situ* as well as *ex-situ* analysis methods can be applied to both the nucleation and (nucleation +) growth layer and a more detailed investigation on the influence of the ion energy on BN growth is possible.

Figure 3.17 shows the FTIR spectra of three BN films, grown with a B^+/N^+ ion energy of (a) 15/20 keV, (b) 20/27 keV, and (c) 31/43 keV. The data has been obtained by measuring the total IR absorption of the nucleation and growth layer using the shutter technique described above, and the differences between the nucleation and growth layer will be discussed in a following paragraph. All spectra in figure 3.17 exhibit the distinct c-BN reststrahlen absorption at around 1065-1068 cm^{-1}, together with the two t-BN peaks at 760 and 1380 cm^{-1}, respectively. Moreover, samples (b) and (c) show an increased absorption due to sp^2-bonded BN with respect to sample (a). The c-BN content, however, remains high, i.e. it is about $89 \pm 3\%$ for sample (a) and then drops slightly to about $82 \pm 4\%$ for samples (b) and (c). Nevertheless, when considering the charge deposited during the growth step and the respective increase in film thickness, the t-BN signal would have been higher if pure t-BN growth had been occured. Although the peak position shift only slightly to lower wavenumbers (1068 cm^{-1} for sample (a) to 1066 cm^{-1} for sample

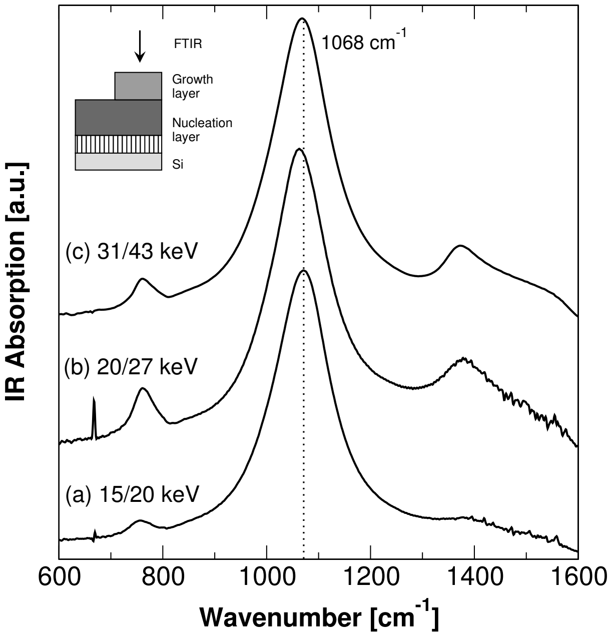

Figure 3.17: FTIR spectra of c-BN films, grown with B^+/N^+ ion energies of (a) 15/20 keV, (b) 20/27 keV, and (c) 31/43 keV. The distinct c-BN TO mode at approx. 1068 cm^{-1} is dominant in all cases, although samples (b) and (c) also show a slightly increased absorption due to sp^2-bonded BN as compared to sample (a).

(b)), the peak widths increase significantly from 125 ± 7 (a) over 133 ± 9 (b) to 142 ± 9 cm^{-1} for sample (c). Thus, the FTIR results indicate that c-BN growth can be maintained even with an ion energy of 43 keV, although the crystalline quality of the growth layer seems to deteriorate for energies above about 20 keV. This is presumably related to effects already observed on the 15/20 keV sample (see figure 3.14): the individual c-BN grains are still highly oriented, but a substantial amount of sp^2-bonded material can be noticed between the crystallites. The increase in t-BN absorption and the peak-widening can thus be accounted for by a decrease in c-BN grain size and an increased agglomaration of sp^2-bonded BN between the grains.

Further evidence for successful c-BN growth with 31/43 keV is given in figure 3.18, which again displays the IR absorption spectrum of the 31/43 keV sample (spectrum labeled (b) in figure 3.18). In addition, the FTIR spectrum of the nucleation layer only has been included in the figure (a). As a consequence of the large film thickness of about 150 nm (corresponding to a deposited charge of $Q = 0.68$ C), the spectrum

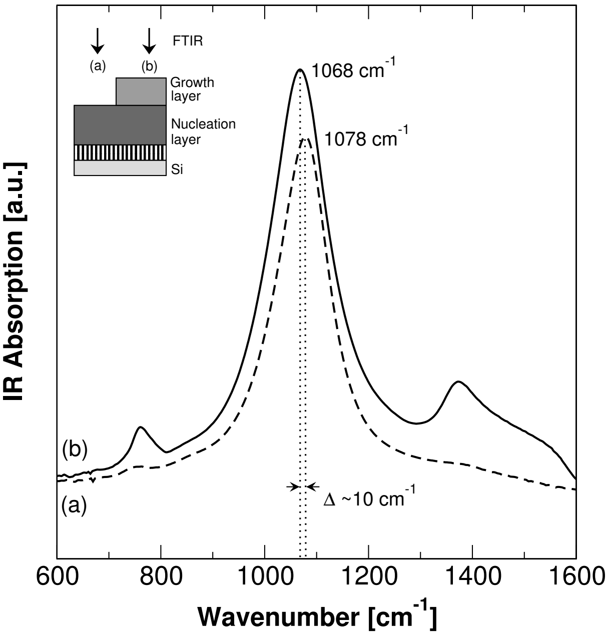

Figure 3.18: Comparison of the IR absorption spectra obtained from (a) the c-BN nucleation layer (grown with E_{ion} = 500 eV and T_S = 250 °C) and (b) both nucleation and growth layer of a BN film that has been deposited with ion energies of 31 keV for B^+ and 43 keV for N^+, respectively. Spectrum (b) shows a stronger absorption for the c-BN as well as the t-BN peaks. Furthermore, the c-BN peak of spectrum (b) is shifted by about 10 cm^{-1} to lower wavenumbers and also exhibits an increased peak width as compared to spectrum (a).

(a) is dominated by the pronounced c-BN absorption at 1078 cm^{-1}, whereas the t-BN peaks are barely visible. Considering the c-BN peak position as well as its width (FWHM$\approx 125 \pm 5$ cm^{-1}), it is apparent that the nucleation layer consists for the most part of c-BN crystallites of comparatively high quality with only a thin t-BN interlayer. In contrast, the c-BN peak position has shifted by about 10 cm^{-1} to a value of 1068 cm^{-1} after the growth layer was deposited, which is similar to the values found for c-BN films grown with $E_{ion} > 5$ keV and indicates a substantial decrease in compressive stress within the film. Although the t-BN peaks at 770 cm^{-1} and 1385 cm^{-1} have increased significantly, the c-BN reststrahlen absorption is still very distinct. In addition, the peak height as well as its width has increased after the growth step, hence, it is indeed reasonable that c-BN growth has continued with 31 and 43 keV ions, although the phase purity and crystalline quality of the growth layer seem to have deteriorated.

In summary, the high-energy deposition experiments described above show that c-BN thin film growth can be maintained at ion energies up to 43 keV, at least while the substrate temperature is at 250 °C. The films exhibit comparatively low compressive stress values, however, the crystallinity and purity of the c-BN layer degrade for ion energies above approx. 10-15 keV. As regards the film microstructure, the well-known Si/Si-B-N/t-BN/c-BN layer sequence is preserved, although substantial amounts of sp^2-bonded material have been observed between the c-BN grains in the upper film region. The customary sp^2-bonded terminal layer has been found missing on the samples examined by means of TEM. Its presence on other parts of the samples cannot be excluded in general, though, but there is strong evidence that an sp^2-bonded layer with a thickness comparable to the ion range has not been formed during high-energy deposition.

3.3 Temperature thresholds for high-energy c-BN growth

As already mentioned in section 3.1.2, growth of c-BN films is possible at room temperature, i.e. about 125 °C below the nucleation threshold. It was therefore concluded that the temperature threshold is related to c-BN nucleation and not its growth. However, the maximum ion energy used in those experiments was 500 eV [Fel97, Fel01], and little is known about the interplay of high ion energies and substrate temperature during growth of BN films. In this subsection, the influence of the temperature during high-energy deposition of c-BN films is studied. The same approach for sample preperation as described in the last section was used: a sufficiently thick c-BN nucleation layer was deposited on silicon (100) substrates by using an ion energy of 500 eV and a temperature of 250 °C. Total deposited charge was 0.36-0.66 C, corresponding to film thicknesses of 80-150 nm. The samples were then cooled down to temperatures between 150 °C and RT and deposition of the growth layer was started once the desired temperature had been reached. Ion energies between 5 and 43 keV have been used in this step.

Figure 3.19 displays the FTIR spectra of a sequence of BN samples that were grown at room temperature on a c-BN substrate. All spectra exhibit a strong c-BN reststrahlen absorption at around 1078-1082 cm^{-1}, together with the two t-BN absorption peaks at 750-770 cm^{-1} and 1360-1385 cm^{-1}. However, the t-BN peak intensity increases with increasing ion energy, and consequently, the c-BN content which is about $\leq 95\%$ for the 500 eV sample, drops to $84 \pm 4\%$ for the 5 keV sample and further to about $60 \pm 5\%$ and $50 \pm 5\%$ for the samples grown with 10 and 15/20 keV, respectively. Thus, it is apparent that a deposition with energies above 5 keV at RT leads to the growth of t-BN films only. In contrast, the results described in section 3.2.3 show that c-BN growth is possible with ion energies up to 43 keV if the substrate temperature is kept at $T_S = 250$ °C. The transition back to t-BN growth as observed here is therefore clearly related to the lowered substrate temperature. In addition, the c-BN growth threshold at room temperature is most likely at an ion energy of around 5 keV. An indication for this is given in figure 3.20, which shows the IR absorption spectra of the films

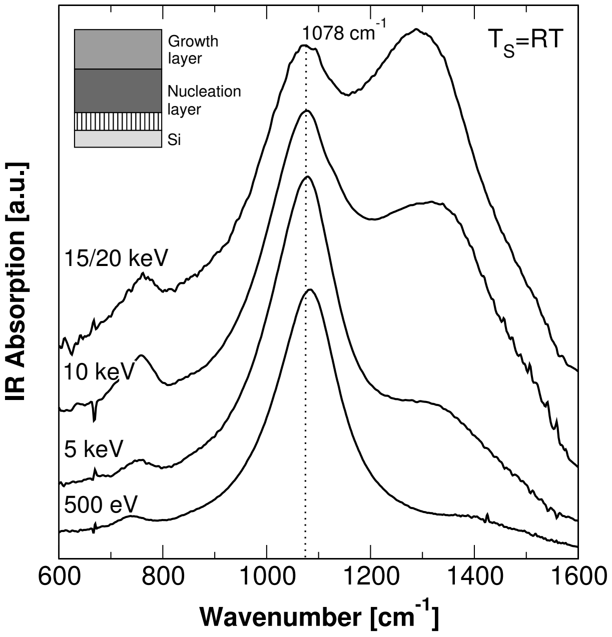

Figure 3.19: FTIR spectra of BN films that have been grown at room temperature with an ion energy of 0.5, 5, 10, and 15/20 keV, respectively, on a c-BN substrate. Using energies above 5 keV at T_S=RT has led to t-BN growth only. The 500 eV spectrum has been taken from ref. [Fel01].

grown with 5 keV (left) and 15/20 keV (right), in comparison to their respective nucleation layers (dashed lines). Obviously, 5 keV ion irradiation has led to a slight increase in t-BN absorption intensity, but the c-BN peak is still very distinct and its intensity as well as the width have increased, too. This implies that the cubic phase has continued to grow, but the crystalline quality and phase purity of the growth layer seem to have deteriorated. On the other hand, deposition with 15 keV B^+ and 20 keV N^+ ions has not only resulted in t-BN formation, but also to a transformation of a substantial amount of the initial c-BN layer into sp^2-bonded BN upon ion irradiation. The c-BN peak intensity drops by about 25-30% after high-energy deposition, which gives rise to the assumption that a region of the intial c-BN layer with a thickness comparable to the ion range of 15 keV B^+ and 20 keV N^+ ions in c-BN has been transformed into t-BN upon ion impact. Under the chosen deposition conditions and taking sputter effects into account, the thickness of the nucleation layer calculates to about 110 nm, including an about 10-15 nm thick t-BN interlayer. The mean range of 15/20 keV B^+/N^+ ions as calculated by

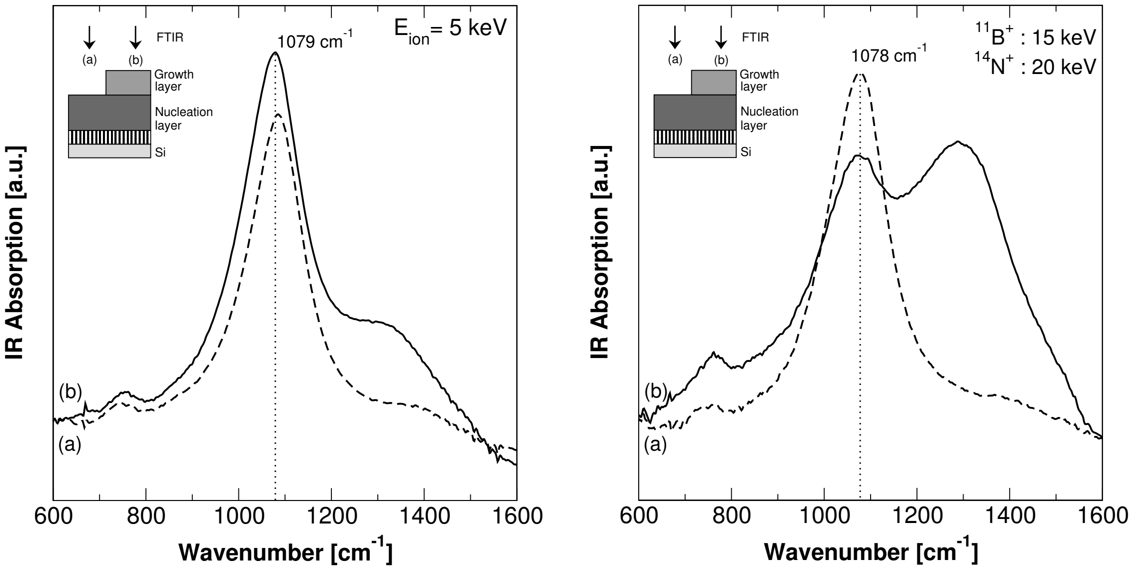

Figure 3.20: FTIR spectra of BN films grown at room temperature with ion energies of 5 keV (left) and 15/20 keV (right), in comparison to their respective nucleation layers (dashed line).

SRIM is 34 nm with a straggling of 10 nm. Hence, a c-BN to t-BN conversion in the upper 30 nm of the initial c-BN film would presumably result into a decrease in absorption intensity as shown in figure 3.20.

A TEM analysis was performed on this sample as well, and the results are displayed in figure 3.21. The darkfield TEM micrograph in figure 3.21(a) shows the entire cross-section of the film. In contrast to figure 3.13, columnar c-BN growth is only visible in the lower part of the sample. After a thickness of about 80 nm, a change in phase composition and texture is visible. In addition, the top most 50 nm contain only small cubic crystallites. The presence of large amounts of t-BN in this region of the film was confirmed by HRTEM, e.g. as shown in figure 3.21(b). Textured turbostratic BN is clearly visible between two c-BN crystallites. Furthermore, the t-BN basal planes are oriented roughly perpendicular to the incident ion beam and are following a 2:3 lattice match to the c-BN. However, all kinds of orientations can be found in the upper part of the sample, e.g. t-BN (0002) planes perpendicular to the substrate surface have been observed as well as completely unordered sp^2-bonded regions. Hence, the TEM analysis corroborates the preliminary FTIR measurements, confirming an interruption of c-BN growth with ion energies of 15 and 20 keV at room temperature.

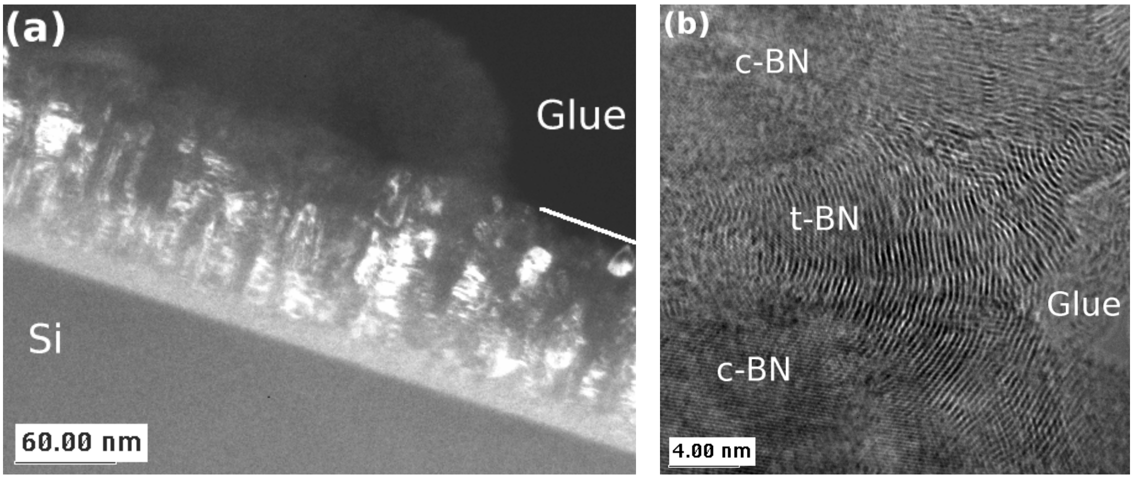

Figure 3.21: TEM images of a BN film, grown with 15/20 keV at room temperature. (a) DFTEM micrograph showing the entire cross-section of the sample. Columnar c-BN growth is visible in the lower part of the film, whereas the top most 50 nm contain only small cubic crystallites. (b) HRTEM image showing large amounts of t-BN between the cubic crystallites near the surface.

Apparently, a critical temperature T_C exists below which c-BN growth reverts back to t-BN growth. In order to investigate this effect in more detail and to gain more insight into the interplay of ion energy and substrate temperature, a series of BN samples was prepared by keeeping the ion energy at a fixed value and systematically lowering the temperature from 250 °C down to RT for each sample. A series of IR spectra for a sample deposited with 15/20 keV is shown in figure 3.22. Decreasing the substrate temperature to 150 and 100 °C did not interrupt cubic phase formation, but at $T_S \leq 60$ °C a strong absorption peak at around 1380 cm^{-1} becomes visible, indicating the formation of a sp^2-bonded phase. The c-BN content drops from about $\leq 94\%$ to $65 \pm 5\%$ for these two samples, and additionally, the c-BN peak position is located at around 1078 cm^{-1}. As mentioned earlier, this value is typical for c-BN films deposited with ion energies of 500-800 eV, hence, it is likely that the c-BN peak in these spectra is due to absorption from the initial nucleation layer. On the other hand, the peak position is shifted by about 10 wavenumbers to a value of around 1068 cm^{-1} for the samples deposited at $T \geq 100$ °C, which fits well to the results described in section 3.2.3. Thus, the transition from c-BN to t-BN growth at an ion energy of 15 and 20 keV, respectively, occurs at a temperature between 100 and 60 °C.

These experiments were repeated with different ion energies, and the critical tem-

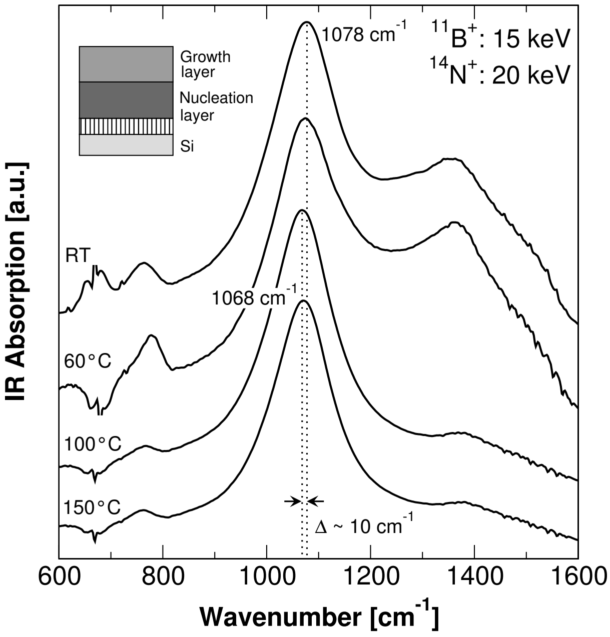

Figure 3.22: FTIR spectra showing the temperature-energy dependence for c-BN growth. The samples were grown with 15 keV B^+ and 20 keV N^+ ions on a c-BN substrate. The substrate temperature was lowered from 250 °C to 150, 100, 60 °C, and RT, respectively, before the high energy deposition was started. c-BN growth can be maintained at T_S = 100 °C and above, but at T_S = 60 °C and below only t-BN films are obtained.

perature T_C below which c-BN growth cannot be accomplished was found to be dependent on the ion energy. Table 3.1 lists T_C as a function of B^+ and N^+ ion energy. While for 5 keV ions a temperature of $T_C \approx 25$ °C is sufficient to maintain c-BN growth, the use of higher ion energies requires increasing the temperature as well. For deposition with 31/43 keV ions T_S must be kept above 100 °C to prevent a transition back to t-BN growth.

B^+ ion energy [eV]	N^+ ion energy [eV]	T_C [°C]
5000	5000	25(8)
10000	10000	60(8)
15000	20000	80(13)
31000	43000	100(13)

Table 3.1: Minimal substrate temperature (T_C) required to maintain c-BN growth on a previously nucleated c-BN film as a function of B^+ and N^+ ion energy.

A temperature dependency for the growth of c-BN films has not been observed or reported so far. In fact, c-BN growth has been regarded as being mostly temperature independent, with the temperature only being important in establishing the boundary conditions necessary for c-BN nucleation. All models developed for c-BN formation thus rely on mechanisms for which the temperature plays only a minor role or is not of importance at all, e.g. sputtering, thermal spikes, or ion-beam-induced defect production and stress generation. Consequently, none of the existing models is able to explain the observed experimental results.

Chapter 4

Boron nitride growth models

In this section, a brief overview of the existing models for c-BN formation will be given. Except for the sputter model, all models that have been applied to describe c-BN film formation were originally developed to explain the growth of diamond-like amorphous carbon (DLC) films and then adapted to c-BN deposition conditions. However, although both materials share certain similarities concerning their fabrication, i.e. the deposition involves an intense bombardment with energetic particles, they also exhibit fundamental differences. DLC films are amorphous and consist of a single, homogenous phase, whereas c-BN is usually nanocrystalline because of the ionicity of the B–N bond, and the films generally exhibit the typical two-layer nucleation sequence explained in section 1.4. In addition, while DLC films are typically deposited at room temperature and with ion energies of around 100-300 eV [Ron97b], c-BN growth is possible at a broad temperature range from RT to 1100 °C and with ion energies between 60 eV and at least 43 keV. Furthermore, as one has to discriminate between c-BN nucleation and its subsequent growth, a successful model must not only account for the different threshold values for ion energy and substrate temperature that exists for these processes, but also for the abrupt change in density from the textured t-BN to nanocrystalline c-BN during nucleation. Hence, because of the complex growth process and the many parameters involved, none of the existing models is able to satisfactorily explain all aspects of c-BN nucleation and growth, especially not the observed energy-dependent temperature threshold and the growth with high ion energies.

In view of the results presented in chapter 3, a new model based on temperature-driven diffusion processes will be developed in section 4.5. By using a combination of SIMS data and SRIM calculations, the critical temperatures below which c-BN growth cannot be maintained are calculated as a function of ion energy [Eyh05], and the predictions made by the model are shown to be in good agreement with the experimental results [Eyh04, Hof04b].

4.1 Compressive stress models

Although ion bombardment seems to be absolutely necessary to form c-BN, it also leads to the generation of point defects (i.e. vacancies and interstitials) in ballistic displacement collisions. These defects induce a volumetric lattice distortion, and are thus being held responsible for the high compressive stress values in the range of several GPa typically found in almost all c-BN films [Mir94]. McKenzie *et al.* therefore proposed a model, after which cubic phase formation is related to the compressive stress created during the ion bombardment process [McK91]. In their investigations, the authors observed the cubic phase only in BN films which exhibited a compressive stress value above 4-6 GPa [McK93]. To that time, the equilibrium phase diagram proposed by Corrigan and Bundy was still accepted (see section 1.2.2) and the predicted h-BN/c-BN phase boundary at around 3 GPa is in reasonable agreement with the ”threshold” value found by McKenzie and co-workers, since the biaxial (compressive) stress differs from the hydrostatic pressure by only a factor of 2/3. Hence, the high stress created during ion deposition would place the BN material in a region of the phase diagram where c-BN is the stable phase [McK93]. Although the more recent phase diagrams identify c-BN as the stable phase at atmospheric pressure, the argumentation by McKenzie *et al.* still holds in principle. They stated that, since the Gibbs free energy of c-BN is smaller than that of h-BN at pressures exceeding 1.6 GPa, a transformation from h-BN to c-BN is still to be expected [McK96]. A quantitative relation between stress and ion bombardment was given by Windischmann [Win87, Win91]. He assumes that, if the substrate temperature is low enough (i.e. $T_S/T_m < 0.25$, T_m melting temperature), defects created by the ion beam are frozen in and the film strain (which is related to the stress by Hooke’s law) is proportional to the number of atoms displaced from their equilibirum sites in the ion collision cascade. This way, he finds that the biaxial stress is proportional to $JE_{ion}^{1/2}$, with J as the ion flux and E_{ion} as ion energy. Thus, the stress shows the same $E^{1/2}$-dependence as the universal parameter p/a introduced by Kester and Messier and Mirkarimi (see section 1.5.2). However, Windischmann's model is static in nature and neglects any defect annealing. As the number of defects created during ion beam deposition is in the order of 10-50 per ion in the energy range of 100 eV–2 keV (as calculated using SRIM), the subsequent accumulation of defects would most likely hamper or prohibit the formation of a crystalline cubic phase.

Consequently, Davis extendend Windischmann's model by taking into account thermally activated defect relaxation induced by spherical thermal spikes [Dav93]. The thermal spike concept will be discussed in detail below, but, in brief, it is based on the assumption that near the end of the ion-generated collision cascade the ions do not have enough energy to displace atoms and will transfer all of their remaining energy to phonons. On a small spatial and temporal scale ($t \approx 10^{-12}$ s, $r \approx 1$ nm), these phononic excitations correspond to temperatures of several 1000 °C, thus giving rise to a high atomic mobility and an increased number of annealing processes within the spike volume. By calculating the rate of defect production and relaxation and by assuming that the defect density is approx. proportional to the relative change in volume, Davis finds for the compressive stress σ:

$$\sigma \sim \frac{E_{ion}^{1/2}}{a/J + kE_{ion}^{5/3}} \tag{4.1}$$

where J/a is the flux ratio (see section 1.5.2), and k is a constant. For small J/a ratios, σ is proportional to $E_{ion}^{1/2}$, in conformity with Windischmann's model. However, for typical c-BN deposition conditions (i.e. $J/a > 1$), σ scales with $E_{ion}^{5/3}$, and the model predicts a decreasing film stress with increasing ion energy. Hence, it fails to explain the observed t-BN/c-BN boundary line in the F/E-phase diagram (see figure 1.12).

Davis' model was later adopted and extended by several researchers. For example, Reinke *et al.* reported a stress-energy-dependence of $\sigma \sim E^{-2/3}$ [Rei96b]. Klotzbücher *et al.* based their model on the rate equations of Davis, but took into account the balance of vacancies and interstitials formed in the film during ion bombardment [Klo98]. This way, the authors found that the stress as a function of ion energy and flux ratio can be described in terms of the momentum transfer p/a as the single independent variable (equation 1.4), and the h-BN/c-BN transition line in the F/E phase diagram can be explained as the curve of minimum stress necessary for c-BN formation. Mirkarimi *et al.* used a kinetic approach to describe stress generation as a process controlled by the dynamics of defect production and relaxation [Mir94]. Within this model, c-BN formation is predicted to occur once the stress exceeds some critical level. Quantitatively, they found that the stress scales with $\sigma \sim E_{ion}^{1/2}$, consistent with their observations.

In summary, all stress models are based on a pressure-induced phase transformation from h-BN to c-BN, while the hydrostatic pressure is assumed to be proportional to the defect density created by the ion bombardment. The dependency between stress σ and deposition parameters $E_{ion}, J/a, T$, however, is treated differently within the models. Windischmann, Klotzbücher and Mirkarimi found an increase in film stress with increasing ion energy. Davis' and Reinke's models on the other hand predict a decreasing stress value for high ion energies, and the majority of experimental results published point to the latter (see for example Ulrich *et al.* [Ulr96], Klett *et al.* [Kle99]), including the findings presented in chapter 3 of this thesis. Furthermore, it has also been found that pure t-BN films can exhibit stress values exceeding 4 GPa [Bou92, Ye98, Kle99, Fit00, Fit01], proving that a high pressure alone is not sufficient to nucleate c-BN, as opposed to the original concept of McKenzie. In addition, Fitz *et al.* [Fit00] and Abendroth *et al.* [Abe04] were able to synthesize c-BN films with stress values as low as 1.3 and 1.7 GPa, respectively, if the growing film was simultaneously bombarded with medium-energetic Ar or N ions.

None of the models is able to explain the role of the substrate temperature for c-BN nucleation, especially not the observed threshold temperature of around 150 °C. Cubic BN films can be readily produced at temperatures above 800 °C [Zha04b, Dey04], however, high temperatures should enhance defect relaxation processes due to an increased atomic mobility, decrease the overall stress and therefore hamper c-BN formation. And finally, the c-BN nucleation process, i.e. the abrupt change in density from t-BN to c-BN, is not discussed or explained by any of the stress models.

4.2 Sputter model

Within the sputter model proposed by Reinke *et al.* [Rei94, Rei95, Rei97], preferential sputter mechanism are being held responsible for the growth of c-BN films. According to this model, both sp^2- and sp^3-bonded BN are formed simultaneously during the deposition process. However, as the sputter yield for sp^2-bonded BN is about 1.5 times larger than for c-BN, the hexagonal phase is preferentially sputtered upon ion bombardment. This way, the model accounts for the three regions (h-BN/c-BN/no growth) in the IBAD-growth diagrams (figure 1.12) and is able to correctly predict the respective phase boundaries. For increasing ion energies and fluxes, the sputter yield for h-BN rises above unity and thus only the cubic phase will continue to grow. If the energy and flux are further increased, the sp^3-bonded phase will be completely resputtered, too.

Presently, it is generally accepted that the mechanisms described in the sputter model are not responsible for c-BN growth. IBAD methods indeed work close to the resputter relimit, but it has been shown that cubic film formation by MSIBD is possible with an ion energy of 125 eV, its subsequent growth even with energies below 75 eV. At these low energies sputtering is insignificant. The same holds true for growth with high ion energies, where the ions are implanted several ten nanometers into the film, and sputtering again is neglectable. And finally, c-BN films are usually covered with a thin sp^2-bonded layer, however, if sp^2-bonded material is preferentially sputtered, the surface should be sp^3-bonded. Consequently, the sputter model is considered obsolete and its relevance is merely historical.

4.3 Subplantation models

The subplantation (*sub*surface im*plantation*) model was introduced by Lifshitz *et al.* in order to describe the growth of diamond-like carbon films by hyperthermal species (i.e. ions or atoms with kinetic energies between 1 eV and about 1 keV) [Lif89, Lif90]. According to Lifshitz, the subplantation process is divided into three stages. In the first stage, the energetic species penetrate into the surface layer and transfer their kinetic energy to the substrate by atomic collisions, phonon excitation, and electronic excitations within a time of 10^{-13} s. It is assumed that preferential displacement of sp^2-bonded atoms with low displacement energies takes place, whereas sp^3-bonded atoms with high displacement energies presumably keep their bond configuration. Furthermore, a fraction of displaced and highly excited atoms become stabilized in metastable sites with high displacement energies, and the site occupation is determined by the surrounding bond configuration in the crystalline matrix. In the second stage, thermal equilibrium between the excited atoms and the surrounding atoms is established within a time of 10^{-11} s. This thermalization process can be treated within the thermal spike concept, which will be discussed below. Finally, the third stage is a long term relaxation stage with a duration of 100 ps to 1 s, where diffusion processes, chemical reactions, and phase transformations are possible. According to the subplantation model, the essential processes determining the final structure of the material take place during the first (collisional) and third (relaxation) stage, while thermal spikes only have a second-order effect on the film evolution.

Robertson modified the subplantation model by placing more emphasis on the energy dissipation processes during a thermal spike [Rob93, Rob94]. In contrast to Lifshitz' model, Robertson assumes the film evolution to be governed by only two, oppositional mechanisms. At first, penetration of ions into the material leads to a local densification, which results into an increase of sp^3-bonds as the atoms "adjust" their hybridization in order to suit the local density. The second mechanism leads to a density relaxation towards sp^2-bonding during a thermal spike, as the interstitials diffuse back to the surface. Thus, the relaxation stage as proposed by Lifshitz is not considered at all; in fact, relaxation processes are assumed to take place during a thermal spike. Robertson's approach is similar to the one used in developing the stress models, as both models relate the formation of a dense, sp^3-bonded phase to an increase in density. Within the subplantation model the density increase is directly responsible for the evolution of sp^3 hybridization, whereas the stress models explain c-BN formation with an increase in biaxial stress, which is related to hydrostatic pressure. Hence, the resulting ion energy and flux dependencies of the relative density increase and the compressive stress, respectively, are quite similar and also exhibit the same deficiencies when used to predict the observed deposition parameter dependence for c-BN formation [Mir97a]. Although Robertson's model also quantifies the c-BN growth regime, it only predicts c-BN growth to be possible within an ion energy range of 50 eV to 500 eV [Rob96], which contradicts the experimental results.

As were all other subplantation models, the semiquantative subplantation model introduced by Boyd, Marton *et al.* was initially developed to describe the formation of tetrahedral amorphous carbon (ta-C) films [Boy98, Mar98]. Within this model, the production of sp^3-bonded structures is determined by a balance between the beneficial effects (subsurface deposition, enhanced diffusion, densification) and deleterious effects (damage production) of energetic particle beams. The amount of damage is taken to be proportional to the accumulated number of ballistic displacements and the conversion of sp^3 to sp^2 bonds is assumed to be proportional to the sp^3-fraction itself. The model is able to describe the energy dependence of the sp^3-fraction f_{sp^3} in ion deposited amorphous carbon (a-C) films using the relation

$$f_{sp^3} = \alpha \ln\left(\frac{E}{E_p}\right) - \beta f_{sp^3}\left(\frac{E - E_D}{E_D}\right) + f_0, \tag{4.2}$$

where E is the ion energy, E_D the displacement energy, E_P the penetration threshold energy, α and β are fit parameters, and f_0 is a constant. The first term describes the penetration probability and the second term the defect production by introducing an efficiency factor β multiplied with the defect production rate $(E - E_D)/E_D$. In addition, the second term is multiplied by f_{sp^3} to take into account that defect production is proportional to the abundance of sp^3-bonded carbon. Finally, the third term describes an energy-independent sp^3-fraction. By choosing adequate values for α and β, the model can indeed give a reasonable good prediction for the ion energy range for which c-BN growth is possible. However, as it was initially developed to describe the growth of amorphous carbon films, the model is not able to describe the observed layered structure of c-BN films or the mechanisms leading to c-BN nucleation. Furthermore, all subplantation models described above can neither explain the temperature threshold for c-BN nucleation nor the energy-temperature dependence for c-BN growth presented in section 3.3.

4.4 Cylindrical thermal spike model

The thermal spike concept was first discussed quantitatively by Seitz and Koehler [Sei54, Sei56] based on the assumption that at the end of an ion-generated collision cascade the ions do not have enough kinetic energy to displace atoms and will instead transfer all their remaining energy Q to phonons. This energy is then deposited into the solid in a point-like manner and dissipates as a spherical spike. For ion energies in the order of several 100 eV the temperatures in a small volume (i.e. a few nm in diameter) around the impact site would be sufficiently high (i.e. several 10^4 K) over a brief time ($10^{-11} - 10^{-12}$ s) to induce permanent rearrangements of the atoms in the solid. The total number n_T of rearrangement processes during a spherical thermal spike was found to be

$$n_T \approx 0.016p \left(\frac{Q}{E'}\right)^{5/3} \tag{4.3}$$

with E' as the activation energy for a rearrangement process and a constant parameter $p \approx 1 - 10$. The number n_T was estimated to be in the range of 5 to 100 for deposited thermal energies Q between 100 eV and several keV [Hof98]. Most or perhaps all of the atoms rearranged in a thermal spike contribute to disordering, which can be expected to be retained. However, Seitz and Koehler pointed out that, in the case of ionic crystals, strong Coulomb forces may re-establish crystalline order. As a consequence of the temperature gradient, which is directed towards the center of the molten spike zone, the ordered lattice at the boundary of the spike region can provide nucleation sites for an inward recrystallization of the spike volume [Sei56].

Weissmantel *et al.* adopted the thermal spike concept in order to explain c-BN film formation quantitatively [Wei81]. They suggested that the formation of the cubic phase is favored if the energy of the thermal spikes dissipates sufficently fast, so that the spike volume is rapidly quenched and thus "frozen in". However, this simple model was based on the phase diagram proposed by Corrigan and Bundy, which predicted h-BN as the stable phase under atmospheric pressure, while c-BN should be metastable. Furthermore, the model cannot explain why the size of c-BN crystallites can reach several tens of nm or why c-BN films typically show a characterstic layer sequence.

Hofsäß *et al.* proposed a model for the formation of diamond-like phases by ion deposition, which includes the effects of thermal spikes in a quantitative way [Hof98].

They stated that, for typical c-BN deposition conditions, each ion impact can be considered as an individual event, well separated in time and distance from the preceding and following impact. Thus, the evolution of a film structure has to be described as a sequence of individual ion-impact processes, each giving rise to a slight change in film properties such as density, composition, and bond configuration. In contrast to other models, which assume thermal spikes having only second-order effects on the film evolution or are considered as a density relaxation mechanism (see section 4.3), Hofsäß *et al.* regard thermal spikes as being directly responsible for the formation of a dense, diamond-like phase. In this view, the evolution of a diamond-like film structure is a consequence of a sufficiently large number of atomic rearrangements during a thermal spike, and each individual ion impact creates a thermal spike which will locally produce a change in the film structure. The resulting local structure is partially determined by the boundary conditions around the spike volume (e.g. film density and bond configuration) and partially by the initial spatial distribution of the deposited energy. Hence, with persistent ion bombardment, the film structure evolves continually until a steady-state condition is reached.

Within the model the process of impact, energy deposition and dissipation of each ion is described by a cylindrical thermal spike with a given initial spatial distribution of the deposited energy. As Hofsäß *et al.* pointed out, the energy deposition in a solid due to ion impact is far from being point-like. Instead, they assume that the energy is deposited uniformely with a constant stopping power dE/dx along the ion track, which has a length L corresponding to the mean ion range. Since for ions with energies exceeding a few hundred eV the major fraction of the initial ion energy is converted into the kinetic energy of primary recoiled atoms and further into phonon excitations, energy distribution is therefore not point- or linelike along the path but described by a cylindrically symmetric Gaussian distribution. In addition, only the energy present in form of phonon excitations (the thermal energy Q, with $Q < E_{ion}$) causes atomic rearrangements during a thermal spike; the fraction of energy converted into electronic excitations is shown not to contribute significantly.

Taking all the features of the ion impact process into consideration, the number of rearrangement processes n_T within a thermal spike was calculated following the approaches of Seitz and Koehler [Sei56] and Vineyard [Vin76]. By using typical values found during the growth of diamond-like films as input parameters, Hofsäß *et al.* found the relation

$$n_T \approx 0.042 \cdot \frac{1}{L} \left(\frac{Q}{E'} \right)^2 \mathrm{e}^{-\sigma^2/\sigma_C^2}. \tag{4.4}$$

Here, σ is the energy-dependent initial width of the cylindrically symmetric Gaussian energy distribution, and $\sigma_C \approx 0.3$ nm is a characteristic width that is dependent on the atomic density, thermal energy, activation energy, and length of the ion track. Thus, the number n_T of rearrangement processes decreases exponentially with increasing initial width σ, while σ itself increases with increasing ion energy because of significant energy transfer from the primary ion to recoil atoms leading to a larger collision cascade volume.

In order to investigate the influence of the number of rearrangement processes on the evolution of a specific phase, however, n_T has to be compared to the total number n_S of atoms present within the spike volume. Rearrangement processes can only modify the local film structure significantly if their number n_T is comparable or larger than n_S. If the ratio $n_T/n_S > 1$, each atom within the spike volume will be rearranged at least once and gets a chance to form stable chemical bonds with its neighbor atoms and a new local structure may evolve. If $n_T/n_S < 1$, rearrangement of the spike volume is incomplete, and it becomes unlikely that the existing local structure can be significantly modified by the ion impact. Within the cylindrical thermal spike model, the ratio n_T/n_S is therefore regarded as the key parameter characterizing the evolution of the resulting film structure.

The number n_S of atoms within the volume V_S should posses a high probability of being involved in a rearrangement process, thus, they must be located in the close vicinity of the ion track in order to gain sufficient energy. If one assumes that a local energy density larger than $E'N$, with N as the atomic density, is sufficient, the volume V_S is then defined as the maximum volume in which the energy exceeds the value $E'N$. The number n_S of atoms in this volume is then given by $n_S = V_S N$. By solving the heat diffusion equation for this energy density value, Hofsäß *et al.* found for n_S:

$$n_s = 0.3679 \frac{Q}{E'} \tag{4.5}$$

Thus, n_S only depends on the activation energy E' and linearly on the deposited thermal energy Q. For ion energies between 100 eV and 20 keV and assuming

$E' = 3$ eV, n_S is between 5 and 1000. The ratio n_T/n_S is then given by

$$\frac{n_T}{n_S} \approx k \frac{1}{L} \frac{Q}{E'} \mathrm{e}^{-\sigma^2/\sigma_C^2}, \tag{4.6}$$

where k is a constant. At low ion energies (i.e. below 100 eV) n_T/n_S initially increases with increasing ion energy and can easily reach values above unity; the maximum possible value has been calculated to $n_T/n_S \approx 10$. At high ion energies, the ratio n_T/n_S strongly decreases whenever the collision cascade becomes large enough and is therefore dominated by the energy dependence of the initial width σ.

For armorphous carbon films (a-C), the condition $n_T/n_S > 1$ is regarded as necessary in order to achieve a transient densification of the material and the formation of a diamond-like phase [Hof98]. For a-C films, a good quantitative agreement is obtained between the experimentally observed ion energy dependence of the sp^3-bond fraction and the calculated n_T/n_S ratio. However, in the case of BN, the existance of an amorphous BN phase is unlikely due to the ionicity of the B–N bond. Thus, one can either form the low-density sp^2-bonded phase or the high-density sp^3-bonded phase. Ion impact with $n_T/n_S > 1$ leads to a complete rearrangement and a recrystallization of the spike volume determined by the surrounding boundary conditions. This process proceeds from the spike boundary inwards and explains why a crystallite (e.g. in the c-BN layer) can grow larger than the volume of one spike.

For the case of c-BN film growth, the model explains the sp^2-bonded surface layer found in most c-BN films as an intrinsic feature of the ion-bombardment process. Ion impact into c-BN cannot lead to a transient densification of the crystalline material, as its density is predefined by the crystalline structure. Additional atoms can only be incorporated as interstitials, which eventually diffuse out, either temperature- or stress-driven. The film surface or the boundaries of individual crystallites act as a sink for these defects. Continued ion bombardment will thus lead to the formation of an sp^2-bonded surface layer, and the transition region between bulk c-BN and this surface layer can be regarded as the actual c-BN growth region, where part of the material is transformed into c-BN upon ion impact.

In order to give a quantitative description for the energy-dependence of the c-BN growth regime, SRIM calculations were carried out by simulating the impact of

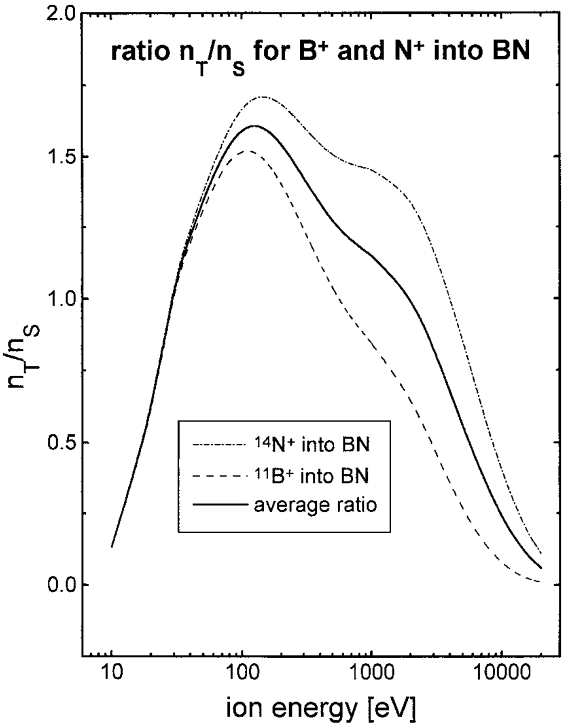

Figure 4.1: Ratio n_T/n_S calculated for $^{11}B^+$ and $^{14}N^+$ ion deposition into c-BN as a function of ion energy. The average ratio is also displayed as indicated by the solid line (from ref. [Hof98]).

$^{11}B^+$ and $^{14}N^+$ into c-BN. The obtained energy dependence of the ratio n_T/n_S is displayed in figure 4.1. As the range of $^{14}N^+$ ions is significantly smaller than that of $^{11}B^+$ due to their larger mass, $^{14}N^+$ ions create a higher initial energy density and are therefore more efficient achieving complete rearrangement during a thermal spike. With increasing ion energy, n_T/n_S grows rapidly in the energy regime below about 100 eV, reaches a maximum around 100-200 eV and decreases rapidly above 3 keV. The initial increase is due to the growing amount of energy being deposited into a more or less constant volume. The maximum is caused by a decreasing amount of ion energy converted into thermal energy and also by the onset of primary collisions. Finally, the decrease at higher ion energies is caused by an increasing collision cascade volume due to secondary displacements. Thus, the ratio n_T/n_S rises above unity at about 50 eV, in agreement with the experimentally observed energy threshold for c-BN growth. Although n_T/n_S decreases below unity above several 100 eV for $^{11}B^+$, it remains high up to about 4 keV in the case of $^{14}N^+$. The model therefore predicts complete rearrangement and optimum c-BN growth conditions between 50 eV and 4 keV.

The mechanism of recrystallization of a completely rearranged spike volume with suitable boundary conditions has also been applied to explain the initial nucleation of c-BN. The texture of the underlying t-BN as well as the spacing of the t-BN (0002) planes allowing a 2:3 lattice matching to the c-BN (111) planes may provide the boundary conditions necessary for c-BN nucleation. The observed energy and temperature threshold are seen as being related to the ability to establish these boundary conditions. The experimental studies by McCarty *et al.* [McC96] described in section 1.5.3 support this hypothesis. In this picture, the temperature-driven diffusion of defects between the t-BN basal planes towards the surface would increase the local order and reduce the interlayer distance. Furthermore, as shown by Feldermann *et al.* [Fel01] and Zhang *et al.* [Zha03], the t-BN interlayer is not a necessary structural precursor, but a preferential c-BN nucleation site which provides crystallographic and interface energy relationships favorable for the formation of c-BN. The choice of appropriate substrate materials and deposition conditions, respectively, makes it possible to avoid the t-BN interlayer and grow c-BN as the initial phase directly on the substrate.

Although the cylindrical thermal spike model is to date the only model that can describe most aspects of c-BN film formation, it does not explain the growth of c-BN with high ion energies or the observed energy-temperature dependence for c-BN growth described in chapter 3.3. This is not surprising, since the mechansim of thermal spike induced rearrangement processes, on which the model is based, should be independent of the substrate temperature because of the high energy density within the spike volume. One can argue that the model does not necessarily predict a transition back to t-BN growth at ion energies exceeding about 5 keV. It is obvious, however, that the mechanisms responsible for maintaining cubic phase formation at high ion energies are not based on atomic rearrangements caused by a thermal spike.

4.5 Modeling c-BN growth with high ion energies

As described in the last section, none of the existing models is able to explain c-BN growth with high ion energies. Furthermore, when considering the immense energy density transferred to the growing film by the bombarding ions, the existence of a rather sharp, energy-dependent threshold temperature below which c-BN growth reverts back to t-BN formation (see section 3.3) is not obvious. Ion bombardment not only leads to a penetration of atoms below the film surface causing a local densification, but also to sputtering effects, electronic excitation and ionization, Frenkel-defect production in ballistic displacement collisions, and excitation of target atom vibrations. It is the balance between these processes (i.e. defect production vs. defect annihilation) that controls the final film structure. An ion induced accumulated defect concentration above a certain critical value will presumably lead to a destruction of the cubic phase, as this effect is well-known for the case of diamond, where prolonged ion irradiation leads to a graphitization of the diamond surface [Rei96a]. Thus, defects, which are created upon ion impact, have to be efficiently annealed out in order to avoid defect accumulation that would eventually lead to a destruction of the cubic phase.

Defect production in ballistic displacement collisions occurs on a timescale of femtoseconds immediately upon ion impact. In the following picosecond, the excitation of target atom vibrations causes a local rearrangement of atomic positions and bonds. This thermal spike has been suggested as being responsible for an efficient suppression of defect accumulation [Hof02]. Within a certain energy regime (ranging from 100 eV to several keV), the number of rearrangements occuring within a thermal spike is an order of magnitude larger than the number of displacements produced by the incident ion beam. Hence, rearrangement processes will completely override the effect of ballistic displacements and the assumption of thermal spike induced annealing of created defects is indeed reasonable. However, as can be seen from figure 4.1, the number of rearrangement processes strongly decreases for energies exceeding 5 keV due to an increasing volume of the collision cascade. Consequently, thermal spike induced annealing becomes ineffective for high ion energies. Since c-BN growth has been shown to be possible with ion energies far beyond 5 keV, an efficient annealing mechanism has to be introduced, which however cannot be based on thermal spikes because of the aforementioned reasons. Instead, an efficient annealing of created implantation defects requires the diffusion of defects (i.e. vacancies or interstitials), followed by mutual annihilation. As a consequence of the bonding ionicity of c-BN, it is then likely to be expected that the cubic crystalline structure is retained [Chr87].

4.5.1 ^{10}B marker implantation into c-BN

As the MSIBD technique allows for the growth of isotopically pure c-BN films (i.e. the films have been prepared exclusively with $^{11}B^+$ and $^{14}N^+$ ions), the following experiment was conducted in order to gain insight into the growth mechanism: Three c-BN films were prepared at standard deposition conditions, i.e. $^{11}B^+$ and $^{14}N^+$ ions were deposited using an energy of 500 eV, a substrate temperature of 250 °C, and a total deposited charge of 0.35 C leading to film thicknesses of about 70 nm. Directly after deposition, the samples were implanted with 2×10^{15} ^{10}B ions/cm^2 and 2×10^{15} ^{14}N ions/cm^2 with $E_{ion} = 10$ keV. This corresponds to a defect concentration of about 0.8 displacements per atom (dpa) [Hof02], although it is important to note that "dpa" describes the accumulated defect concentration generated by ballistic displacements neglecting any defect annihilation.

One sample was kept at 250 °C (i.e. above T_C) while the other one had been cooled down to room temperature prior to implantation. In addition, the third sample has been implanted at room temperature and was then annealed at 250 °C under UHV conditions for one hour. Since ^{10}B and ^{11}B behave chemically identical, ^{10}B is particularly well suited to act as a marker, allowing for the determination of depth distributions as a function of implantation and annealing temperature. This way, information on B diffusion processes can be gained. Since c-BN is known to be very sensitive on stoichiometric changes, ^{14}N has been co-implanted in order to ensure a stoichiometric film composition.

The samples were characterized by FTIR spectroscopy after implantation (and annealing), and the results are shown in figure 4.2. All three samples show a distinct c-BN reststrahlen absorption at around 1080 cm^{-1}, and only weak t-BN peaks at about 760 and 1380 cm^{-1}, respectively. Although the t-BN absorption seems to be slightly larger for the samples implanted at room temperature, one cannot reli-

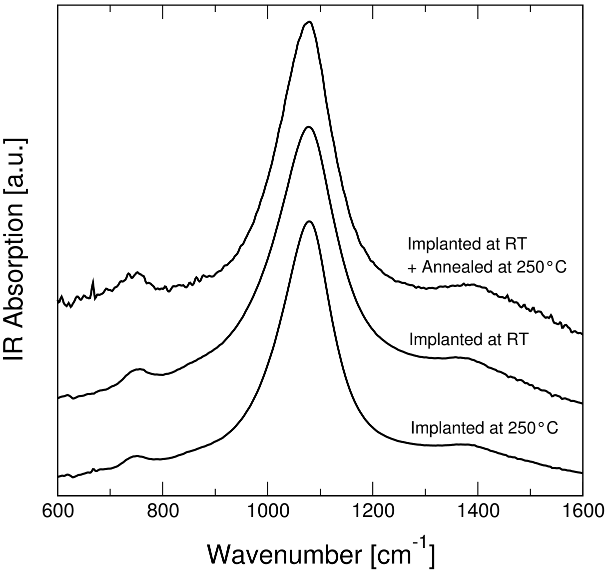

Figure 4.2: FTIR spectra of three c-BN samples that have been implanted with 2×10^{15} $^{10}B^+/cm^2$ and 2×10^{15} $^{14}N^+/cm^2$, respectively. One sample was implanted at $T_S = 250$ °C, the other two films at $T_S =$ RT. One of them was subsequently annealed at 250 °C for one hour under UHV conditions. All three samples show strong c-BN absorption peaks.

ably conclude on structural changes within these samples from FTIR results alone. Due to the low irradiation fluence, IR spectroscopy may not be able to detect an ion-beam-induced phase transformation, which might have occured for the samples irradiated at room temperature.

Secondary ion mass spectroscopy (SIMS) was then applied to measure the ^{10}B implantation profiles. The ^{10}B profile due to implantation at room temperature is displayed in figure 4.3b (represented by circles), together with the profile that resulted from implantation at 250 °C (up triangles). Both data sets have been fitted using a Gauss-function (solid lines). When comparing the two curves, there are two striking differences: First, when implanting ^{10}B at 250 °C, the maximum of the depth profile is positioned at a depth of about 20 nm, i.e. about 6 nm closer to the surface as compared to the profile resulting from implantation at RT (maximum position at $\approx$ 26 nm). Second, the RT profile is broader than the 250 °C one. Since the samples were prepared identically except for the temperature during final $^{10}B/^{14}N$ implantation, both effects must be due to the different substrate tempera-

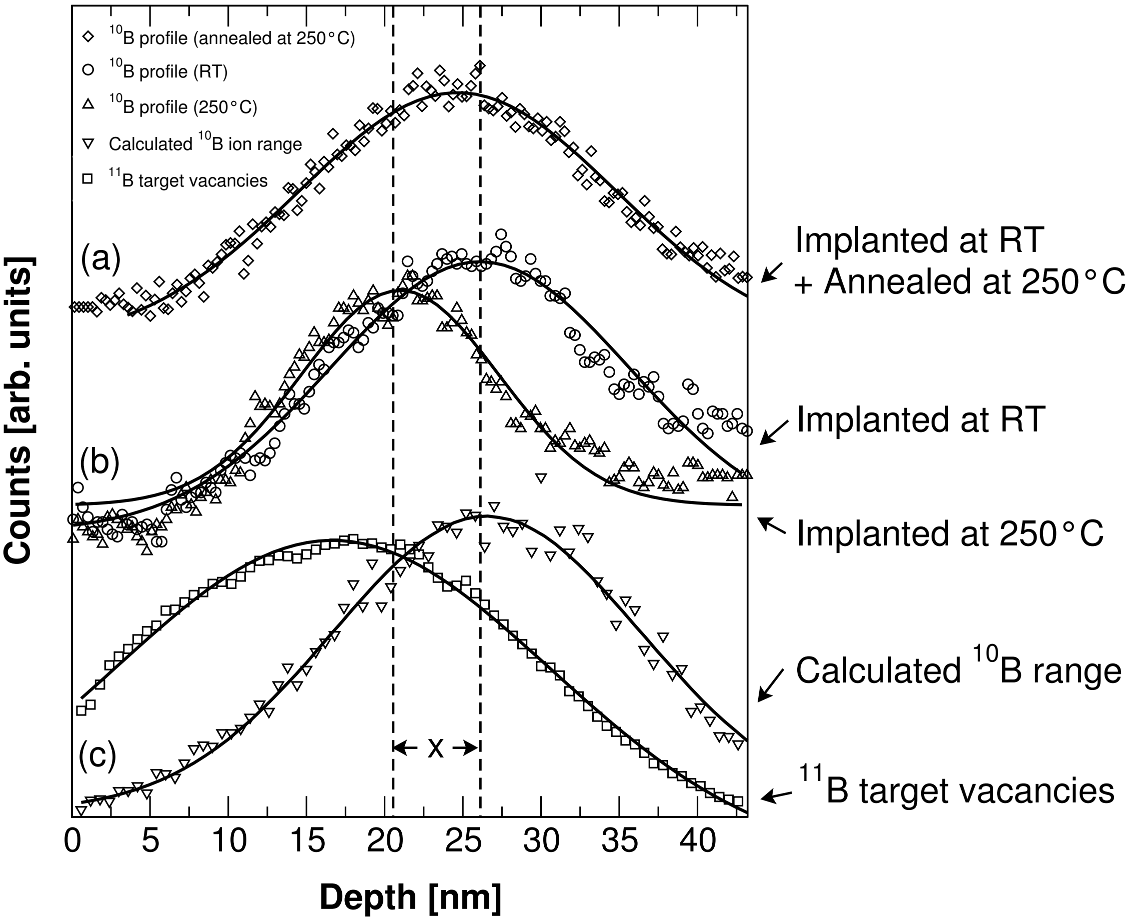

Figure 4.3: (a+b) SIMS depth profiles of 2×10^{15} $^{10}B^+/cm^2$ implanted into a c-BN sample with an ion energy of 10 keV. (a) Implantation at room temperature and subsequent annealing at 250 °C for one hour under UHV conditions. (b) Implantation at room temperature (up triangles) and at 250 °C (circles). (c) ^{10}B depth profile as calculated by SRIM, when implanted with 10 keV into a c-BN sample (down triangles). Squares represent the SRIM calculated number of ^{11}B target vacancies created by the incident ion beam. This data has been scaled down in order to be comparable to the calculated depth profile.

tures and cannot be related to other sample properties. Furthermore, an annealing step subsequent to implantation at RT is not sufficient to reproduce the 250 °C-profile. As can be seen from figure 4.3a, annealing leads to a further broadening of the peak and only to a slight shift of the maximum towards the surface. Thus, one can conclude that the shape of the aforementioned implantation profile is related to effects, which occur during ion impact and not afterwards.

Figure 4.3c shows the SRIM calculated implantation profile for 10 keV $^{10}B^+$ ions impinging on a c-BN target (down triangles). Position and width are in very good agreement with the RT profile when using a c-BN target density of $\rho = 3.2$ g/cm^3 for the simulations. Additionally, the ^{11}B target vacancy distribution has also been calculated and is represented by the open squares in figure 4.3c. This damage profile has its maximum at a depth of about 16 nm, which as about 10 nm lower than the mean ion range of ^{11}B implanted into c-BN.

4.5.2 Model requirements

Besides sputtering, electronic excitation, ionization and excitation of target atom vibrations, ion impact on a target material leads to defect production (i.e. vacancies and interstitials) in ballistic displacement collisions. The number of vacancies initially created through primary and secondary collisions can be calculated by SRIM and is between 50 and 200 per ion in the energy range from 5–30 keV. About the same number of target interstitials are generated, with a distribution similar to the vacancy profile displayed in figure 4.3c. When comparing the experimental and calculated data in figure 4.3, one can draw the conclusion that a higher substrate temperature during implantation (or growth) leads to a higher atomic mobility, which allows the implanted atoms to diffuse a certain distance backwards along the ion track. At room temperature, significant atomic movement is not observed, hence, the ability to dynamically anneal radiation damage is suppressed and defect accumulation sets in.

Consistent with this assumption are the findings by Deyneka *et al.* [Dey04], who observed significantly improved c-BN grain sizes and overall crystallinity when using high substrate temperatures (i.e. $T_S > 800$ °C) during c-BN growth, presumably due to an increased atomic diffusivity. Furthermore, Zhang *et al.* found that epitaxial growth of c-BN on diamond is only possible at temperatures above approx. 900 °C, which was attributed to an efficient dynamic annealing of radiation damage at high temperatures [Zha03]. The use of lower temperatures resulted in an amorphization of the diamond surface. Thus, it is indeed reasonable to assume that the ability to form c-BN at substrate temperatures above T_C is related to an increased atomic mobility that leads to an efficient annealing of ion-beam-induced defects. However, when lowering the substrate temperature below T_C (e.g. room

temperature), diffusion processes are strongly suppressed, defects will accumulate and finally lead to a destruction of the cubic phase.
Assuming the temperature dependence of the diffusion coefficient D obeys an Arrhenius law, $D = D(T)$ is then given by

$$D = D_0 \exp(-W_m/\mathrm{k_B}T), \tag{4.7}$$

where D_0 is the temperature-independent diffusion constant, W_m is the migration energy, T the temperature and $\mathrm{k_B}$ the Boltzmann constant. Using the relation

$$D = x^2/t, \tag{4.8}$$

with x as the diffusion length and t as the diffusion time, a combination of (4.7) and (4.8) gives:

$$T = -\frac{W_m}{\mathrm{k_B} \ln\left(\frac{x^2}{D_0 t}\right)}. \tag{4.9}$$

In order to use this equation to calculate the critical temperatures needed to maintain c-BN growth at a given ion energy, three assumptions have to be made:

1. Diffusion length x

As mentioned earlier, ion bombardment leads to an initial defect production of around 100 total displacements per ion in the energy range of 5 to 30 keV, with a comparable spatial distribution of vacancies and ^{11}B and ^{14}N interstitials. Figure 4.4 displays the ^{11}B interstitial and ^{10}B implantation profile created by irradiation of a c-BN target with 10 keV ^{10}B ions. The ratio of ^{10}B/^{11}B interstitials derived from those profiles is also shown in the figure and increases from $\ll 1\%$ at the surface to approx. 5% at about 40 nm depth. Thus, due to a significant amount of ^{10}B, an excess of B interstitials compared to the locally available vacancies exists at a depth beyond the vacancy maximum. Recombination with vacancies therefore requires diffusion of boron atoms towards the vacancy maximum. This situation is indicated by figure 4.5. It shows an SRIM simulated impact of a 5 keV ^{10}B ion into a c-BN target. The ion track is represented by the red line. The ion collides with target atoms along its path, and generates vacancies and interstitials by transferring part of its energy to target atoms. These recoils can also start a collision cascade

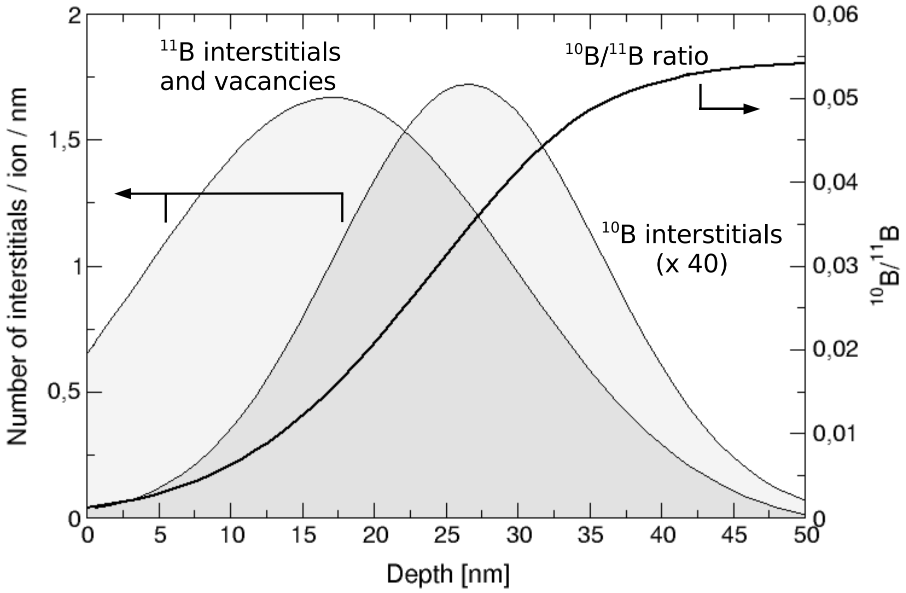

Figure 4.4: ^{11}B interstitial and ^{10}B implantation profile as created by irradiation of a c-BN target with 10 keV ^{10}B ions. The ^{10}B/^{11}B ratio increases from $\ll 1\%$ at the surface to about 5% at ≈ 40 nm depth.

(green tracks), if their energy is large enough. It is of importance to note that the ^{10}B profile and movement in figure 4.3 only describes diffusion processes at the end of the ion track. In order to avoid defect accumulation, ^{11}B interstitials generated in either primary or secondary collision cascades are also required to move backwards along the ion track (indicated by the black arrows in figure 4.5). The distance interstitial atoms have to diffuse in order to annihilate with vacancies can

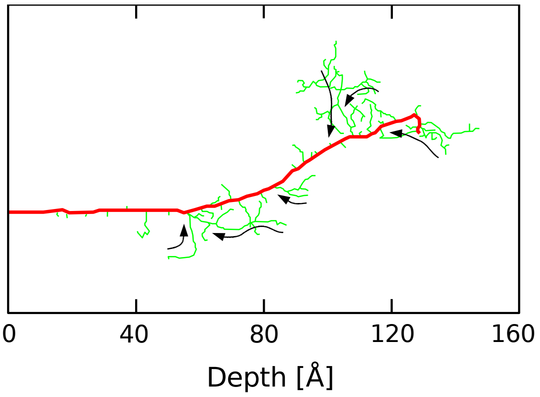

Figure 4.5: Graphical visualization of a B^+ ion impact into a c-BN target with an ion energy of 5 keV as calculated by SRIM. The ion path is represented by the red line. Along its path it creates vacancies and interstitials through ballistic displacement collisions. If the energy transferred to recoils is sufficiently large, the latter can as well generate a collision cascade (green tracks) and create defects. Diffusion of interstitials backwards along the ion track is indicated by the black arrows.

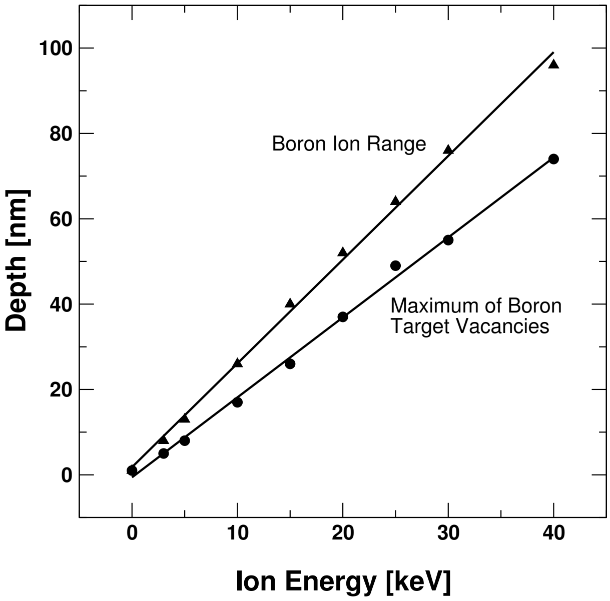

Figure 4.6: Projected range of ^{11}B ions implanted into c-BN as a function of ion energy (triangles). Circles represent the position of the maximum of the projected boron target vacancy profile as created by the incident ion beam. The data has been calculated by SRIM.

be estimated by using the available SIMS data in addition to SRIM simulations. A comparison of the measured and calculated profiles in figure 4.3 yields a diffusion length x that is approx. given by the depth difference of vacancy and implantation profile. Figure 4.6 shows the projected range of ^{11}B ions implanted into c-BN as a function of ion energy (triangles), and the position of the maximum of the boron vacancy distribution (circles) as calculated by SRIM. Within the given energy range, both vacancy maximum position and ion range increase linear with the ion energy. Thus, the distance between both profiles is proportional to the ion energy as well, and this value will be used as (energy-dependent) diffusion length x. However, it should be mentioned that the effective diffusion length could be larger than this assumed value. This is related to the fact that both SRIM and SIMS data only show the projected ion and vacancy distribution, but particle trajectories in a material have to be treated three-dimensionally. Hence, the calculated value x is most likely being underestimated.

2. Diffusion constant D_0

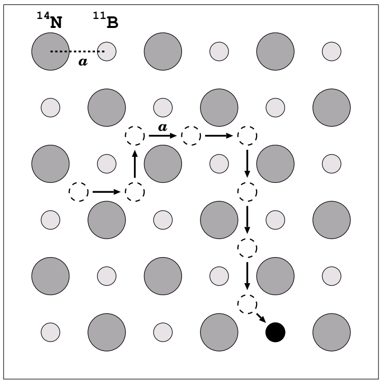

Figure 4.7: Schematic diagram of a simple random walk diffusion mechanism.

Atomic diffusion processes are often discribed by using random walk models, which treat atomic motion in a material as jumps of fixed length in specific directions, usually between different minima in a potential landscape (figure 4.7). In crystalline solids, these minima are represented by lattice sites or interstitial sites. Thermally activated, jumps occur at a rate ν', with a temperature dependence that obeys an Arrhenius law:

$$\nu' = \nu_0 \exp(-W_m/\mathrm{k_B}T), \tag{4.10}$$

where ν_0 is the attempt frequency, W_m is the migration energy, $\mathrm{k_B}$ the Boltzmann constant, and T is the temperature. If jumps can occur to Z neighboring sites, the total jump frequency is then given by

$$\nu = Z\nu'. \tag{4.11}$$

After a given time t, a particle was able to perform $N = \nu t$ jumps, and its trajectory is composed of a sequence of elementary jumps with average jump length a. The diffusion coefficient in three dimensions is then given by the Einstein-Smoluchowski relation

$$D = \frac{1}{6}a^2\nu, \tag{4.12}$$

which leads to a diffusion constant D_0 of

$$D_0 = \frac{Z}{6}a^2\nu_0. \tag{4.13}$$

The attempt frequency can be set to $\nu_0 = 10^{13}$ Hz, which is a typical phonon frequency in diamond-like materials [Hof98]. Cubic BN with its zinc-blende structure exhibits a variety of lattices sites that can be occupied by interstitial atoms, e.g. tetrahedral, bond-center, or hexagonal sites (see e.g. ref. [Wah97] for an overview). As the use of a simple random walk mechanism to calculate the diffusion constant is only a rough approximation in the first place, it will be assumed that atomic jumps occur mainly between tetrahedral sites. Thus, an interstitial atom has the possibility to jump into 4 adjacent sites, which leads to a coordination number of $Z = 4$ and a jump length of the order of the c-BN bond length ($a = 1.5$ Å). Combining the above estimates yields a diffusion constant of $D_0 \approx 1.5 \times 10^{-3}$ cm^2/s.

3. Diffusion time t

The diffusion time t can be estimated when considering the deposition parameters used during film growth. As described in detail by Hofsäß *et al.* [Hof98], each ion impact during MSIB deposition can be considered as an individual event, well separated both in time and distance from preceding and following impacts. The affected projected area during a single ion impact has been estimated to 1–10 nm^2 in the energy range from 1 keV to 40 keV by using SRIM. With typical ion currents of 20 μA deposited on an area of about 2 cm^2, the time between subsequent ion impacts into the same target region calculates to $t \approx 0.1$ s. Therefore, the affected target volume can relax for at least 0.1 s before the next ion hits the same area. When comparing this value to the typical duration until thermalization ($\approx$ 1 ps)

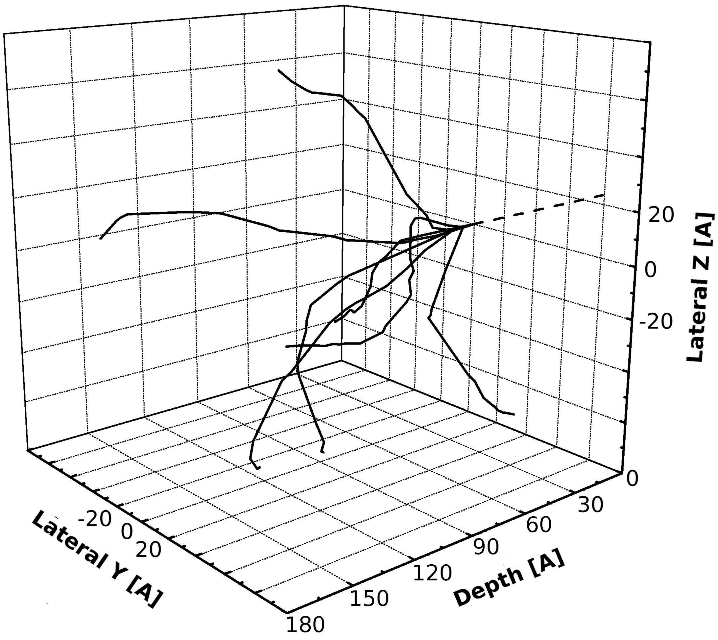

Figure 4.8: 3-dimensional visualization of several ion impacts with $E_{ion} = 5$ keV into c-BN as calculated by SRIM.

for an ion impact, it becomes obvious that the picture of individual ion impacts holds even for an ion flux of up to several A/cm^2.

However, it is difficult to give an exact value for the time t. This is mainly related to the fact that particles in a material move on three-dimensional trajectories, but the value for t has been derived by projecting the trajectories onto a two-dimensional plane. Figure 4.8 shows a number of SRIM simulated impacts of 5 keV ^{11}B$^+$ ions into a c-BN target. Although all ions enter the material at the exact same spot, the affected target volumes do not necessarily overlap for each impact. Thus, the relaxation time t could be significantly larger than the assumed value of 0.1 s. As pointed out by Lifshitz *et al.*, the duration of this relaxation stage can be as large as $t = 1$ s [Lif90]. Nevertheless, for the following calculations, the diffusion time will be set to $t = 0.1$ s, and the influence of a larger value t will be discussed in a following paragraph.

4.5.3 Discussion for c-BN growth

By using the estimated values for diffusion length $x(E)$, diffusion constant D_0, and diffusion time t, one can now calculate the critical temperatures required to maintain c-BN growth at a given ion energy. In order to avoid defect accumulation, at least stationary equilibrium between defect production and annealing has to be established. This state is reached, when an interstitial atom is able to diffuse the distance $x(E)$ within the time $t = 0.1$ s. Figure 4.9 presents the critical temperatures using the data from table 3.1. Those values have been fitted using equation (4.9), with $t = 0.1$ s, $x = x(E)$, and $D_0 = 1.5 \times 10^{-3}$ cm^2/s as mentioned previously and W_m as fit parameter. The fit has been included in the figure as indicated by the solid line and shows a good agreement with the experimentally gained data points. A migration energy of $W_m = 0.5(1)$ eV has been extracted from the fit. For 5 keV ions, the model predicts c-BN growth to be possible even at room temperature, in agreement with the experimental results. Using 40 keV B$^+$ ions (and 60 keV N$^+$ ions, respectively) would require a substrate temperature of at least 400 K.

The use of larger diffusion times does not change the calculated migration energy significantly. For $t = 1$ s for example, a value of $W_m \approx 0.55$ eV is obtained. This is mainly related to the logarithmic dependency of temperature T on diffusion time t

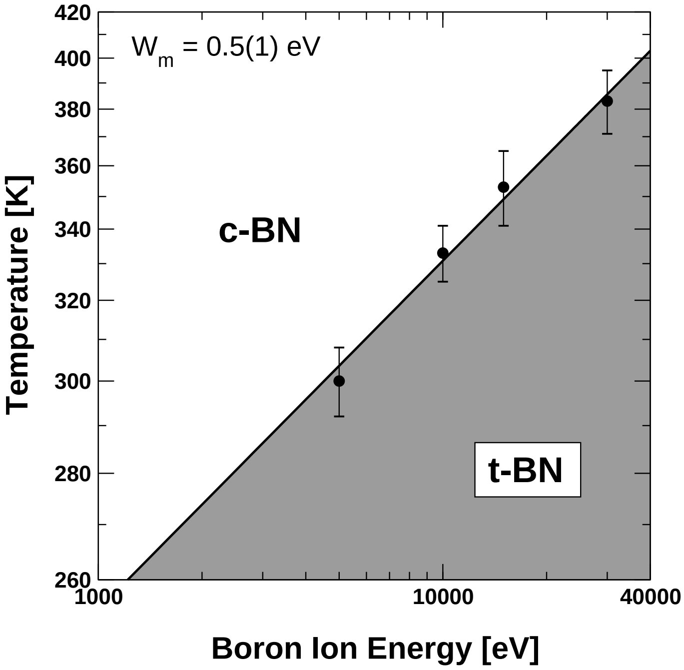

Figure 4.9: Minimum temperature required to maintain c-BN growth on a previously nucleated c-BN film as a function of B^+ ion energy, plotted as $\log_{10}(E)$ vs. $1/T$. The data points have been fitted using equation (4.9) with $t = 0.1$ s, $x = x(E)$, and $D_0 = 1.5 \times 10^{-3}$ cm^2/s. A migration energy of $W_m = 0.5(1)$ eV was extracted from the fit.

in equation (4.9), which only leads to slight changes in T when varying t. Currently, there is no possibility to gain further information about the diffusion time other than estimating values based on SRIM simulations. Since the relaxation time used in the model has been assumed to be related to the time between subsequent ion impacts into the same target region, it is thus inversely proportional to the ion flux used during deposition. Because T is a function of $\log(t)$, a significant influence of the flux on the temperature is only to be expected if the ion flux would be increased by several orders of magnitude. Unfortunately, with the ion source currently installed at ADONIS, the flux can only be adjusted within a very narrow range, which makes further investigations concerning diffusion times experimentally inaccessible at this time.

The same holds true for ion energies exceeding about 50 keV. Due to the instability of the t-BN/c-BN interface upon ion irradiation, the nucleation layer has to have a thickness larger than the range of the high energetic ions used in the subsequent growth step. However, because of the painfully low ion currents achievable with ADONIS, the effective film thickness is limited to about 150 nm.

As can be seen from figure 4.9, the model predicts the critical temperature to be very sensitive on ion energy changes for $E_{ion} < 3 - 5$ keV, which would offer the opportunity to test the proposed model by using lower energies. However, for ion energies below 5 keV, the critical temperatures are expected to be below room temperature. Thus, those experiments would require the sample to be cooled during deposition, which is currently not possible. It is interesting to note that the energy regime below about 5 keV is the region for which the cylindrical thermal spike model predicts complete rearrangement during a thermal spike, i.e. the parameter n_T/n_S increases above unity (see section 4.4 and figure 4.1). According to the model, thermal spike induced rearrangements would then be responsible for suppressing defect accumulation and maintaining cubic phase formation. Consequently, c-BN growth is then expected to be mostly temperature-independent.

By using the calculated values for D_0 and W_m, it is possible to give an estimation for the defect concentration generated by the ion impact as a function of annealing time. If one defines the defect concentration c generated by a single ion impact as

$$c = N_i/N, \tag{4.14}$$

with N_i as the number of interstitials and N as the total number of atoms within a collision cascade volume, the decrease of c over time due to recombination processes is then given by [Rei96b]

$$-\frac{\mathrm{d}c}{\mathrm{d}t} = c^2 \nu_0 \mathrm{e}^{-W_m/kT}. \tag{4.15}$$

Solving this equation with $c(t = 0) = c_0$ leads to

$$c(t) = \frac{c_0}{t c_0 \nu_0 \mathrm{e}^{-W_m/kT} + 1}. \tag{4.16}$$

At $t = 0$, i.e. immediately after ion impact, the number N_i of interstitials created by a 10 keV B^+ ion is about 100. An estimation of the volume of the collision cascade yields a value of about 100–150 nm^3, assuming an ion range of 26 nm and a projected area of about 5 nm^2. Thus, using a c-BN mass density of $\rho = 3.5$ g/cm^3

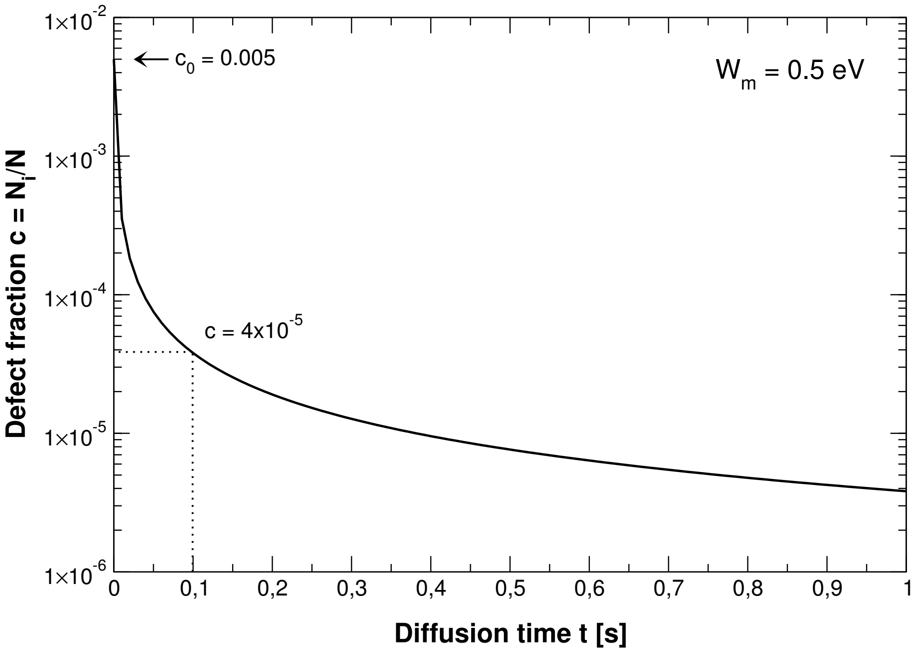

Figure 4.10: Defect fraction $c = N_i/N$ within a collision cascade volume as a function of diffusion time t, as given by equation (4.16). A migration energy of $W_m = 0.5$ eV, a temperature $T = 333$ K (corresponding to T_C for 10 keV ions) and an initial defect fraction $c_0 = 0.005$ have been assumed.

and a molar density of $m_{mol} = 12.5$ g/mol leads to a number of atoms in the collison cascade of about $N \approx 20000$. The defect fraction in the cascade volume is then given by equation (4.14) and calculates to

$$c_0 \approx 5 \times 10^{-3} = 0.5\ \%. \tag{4.17}$$

Diffusional annealing processes will then lead to a recombination of interstitials with vacancies, and the defect concentration will decrease according to equation (4.16). The time dependence $c(t)$ of the defect fraction has been plotted in figure 4.10 by assuming a migration energy $W_m = 0.5$ eV, a temperature $T = 333$ K (corresponding to T_C for 10 keV ions), and an initial defect fraction c_0 as given above. After a time $t = 0.1$ s, the number of defects per target atom has decreased to about 4×10^{-5}, hence, almost all (99.996%) of the 100 initially created interstitials have been annealed out. Increasing the available diffusion time leads to a slightly slower annealing rate, but even when using a migration energy $W_m = 0.55$ eV, the number of defects still decreases by about 96% after a time $t = 0.1$ s. Thus, the majority of recombination processes occur within a short time after ion impact.

Existing data on diffusion constants and migration energies for c-BN are sparse, and self-diffusion constants and activation energies have not been published so far. Deyneka *et al.* examined the temperature dependent evolution of argon depth profiles in BN films prepared by ion beam assisted deposition [Dey03]. A migration of Ar atoms at temperatures above 1000 K was attributed to grain boundary diffusion, and a diffusion coefficient $D = 2 \times 10^{-16}$ cm^2/s at a temperature of 1373 K was reported, which would lead to an activation energy of $W_A \approx 3.5$ eV. By using the analogy of c-BN to diamond, one may be able to compare the calculated data to the results published by Quintel *et al.* [Qui96], who examined the annealing behavior of heavy-ion implanted diamond. They found two annealing stages in diamond, the early one occurs in the temperature range 300-600 K and was attributed to interstitials trapped at defects in the collision cascade being released as the temperature is increased, and combining with vacancies. The fact that interstitial atoms in diamond are able to migrate distances comparable to the size of the collision cascade already at temperatures as low as 300 K is quite similar to the described experimental results for the c-BN case. In an other study by Allers *et al.* [All98], the intensity of the GR1 band in diamond (i.e. absorption caused by vacant lattice sites) as a function of annealing temperature and time was examined by means of absorption spectroscopy in the UV/visible range. The observed decrease in absorption intensity was attributed to migration of interstitial atoms to vacancies, followed by mutual annihilation, and a migration energy of $W_m = 1.68$ eV for the process was reported.

In summary, the characteristic energy-dependent temperature threshold for c-BN growth as described in chapter 3.3 is explained by dynamic annealing of defects caused by an impeding ion in a collision cascade. In this picture, the suppression of defect accumulation that is crucial for maintaining cubic phase formation is attributed to temperature-driven back-diffusion and subsequent annihilation of B and N interstitial recoils. With the assumption of an Arrhenius diffusion behavior and a combination of SRIM simulations and SIMS measurements the critical temperatures as a function of ion energy were calculated. A diffusion constant $D_0 = 1.5 \times 10^{-3}$ cm^2/s and a migration energy $W_m = 0.5(1)$ eV for interstitial boron diffusion in c-BN have been estimated.

4.5.4 Discussion for c-BN nucleation

Diffusional annealing processes may also play a role for c-BN nucleation. As mentioned before, c-BN formation can only be initiated if substrate temperature and ion energy exceed certain threshold values. For MISB deposited c-BN films the thresholds are $E_{ion} = 125$ eV and $T_S = 150$ °C. Lowering either one below these values will result in deposition of t-BN films only. It is commonly agreed upon that compressive stress induced by the incident ion beam is indispensable to orient the t-BN basal planes parallel to the surface normal, a feature present in most if not all c-BN films grown on silicon substrates. The role of the substrate temperature, however, is not clear. The experiments reported by McCarty *et al.* (see section 1.5.3) may already indicate the relevance of diffusion processes during nucleation, as they could be responsible for the observed decrease of the t-BN basal plane distance, which is apparently required to establish the necessary boundary condition.

The phase diagram for ion beam deposited BN films as introduced in section 3.1.1 shows sharp thresholds for both ion energy and substrate temperature, below which c-BN growth cannot be accomplished. Theses thresholds seem to be independent of each other, however, the respective boundary lines are not exact, but have been extrapolated to higher energies based on data obtained for c-BN nucleation at ion energies below about 500–800 eV.

In order to investigate the influence of ion energy on the temperature threshold, BN films investigated in this section were deposited directly on silicon substrates with energies ranging from 500 eV to 5 keV and substrate temperatures between 150 °C and 250 °C. The results of the subsequent FTIR characterization are shown is figure 4.11a. All ion energies used are well above the nucleation threshold of $E_{ion} = 125$ eV and, except for the 5 keV sample, successful c-BN nucleation at those energies has been demonstrated before [Fel98]. For the sample grown at 500 eV, the substrate temperature was below the threshold value of $T_S = 150$ °C and as expected, only t-BN has been formed. On the other hand, for the samples deposited with 800 eV and 1 keV, T_S was kept above 150 °C and no c-BN could be found within the films either. Increasing the substrate temperature to 250 °C has led to successful c-BN nucleation and growth, as confirmed by FTIR spectroscopy [Hof97]. At an ion energy of 5 keV no cubic phase was found within the film, even though the temperature was set to 250 °C.

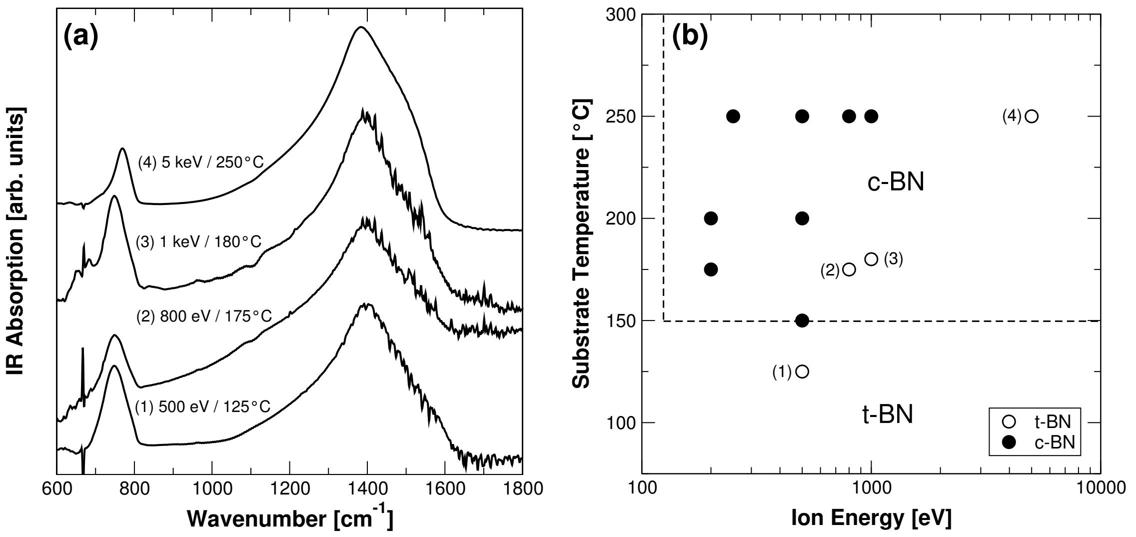

Figure 4.11: (a) FTIR absorption spectra of BN films, directly deposited on silicon substrates with ion energies ranging from 500 eV–5 keV, at substrate temperatures of 125–250 °C. No c-BN signal is visible. Instead, all samples show a strong t-BN absorption with broad peaks at around 1380 cm^{-1}, indicating a highly disordered film structure. (b) Phase diagram for ion beam deposited boron nitride films, as introduced in section 3.1.1. The c-BN content is plotted as a function of ion energy and substrate temperature. Filled symbols indicate successful c-BN formation, whereas hollow symbols represent t-BN samples. Contrary to previous assumptions (as indicated by the dashed line), the temperature and ion energy thresholds are not independent of each other.

Figure 4.11b displays the phase diagram for MISB deposited BN films, which includes the previously accepted phase boundary as indicated by the dashed line. The FTIR results explained above are also shown and are represented by the hollow symbols labeled (1)-(4), corresponding to the respective IR spectra displayed in figure 4.11a. Hence, the independence of energy and temperature thresholds has been disproved. Instead, increasing the ion energy requires the use of a higher substrate temperature as well, an effect quite similar to the results found for the growth of c-BN films. Furthermore, the IR spectra are almost identical to each other, although the corresponding samples were deposited at different conditions. They exhibit features common to room temperature grown BN films, i.e. the peak at approx. 1380 cm^{-1} is very broad and shifted to lower wavenumbers. Most likely, the samples are structurally almost identical and consist of a highly disordered sp^2-bonded phase.

It has to be noted that the existence of a high energy threshold, above which c-BN nucleation is no longer possible, is very likely. However, further investigations regarding this matter are very difficult. As already observed by Feldermann [Fel02], the thickness of the t-BN interlayer increases with increasing ion energy, which would thus require the growth of very thick films in order to possibly detect c-BN within the sample. Figure 4.12 displays the FTIR spectra of three BN films that have been deposited with 2, 3, and 5 keV, respectively, on silicon substrates at a temperature of 250 °C. The total deposited charge for each film was $Q = 1.3 - 1.4$ C, which resulted in film thicknesses of 1.2–1.6 μm, as measured using profilometry. For the sample deposited with $E_{ion} = 2$ keV, the cubic phase content calculates to about 50%, but a further increase of the ion energy leads to a drastic decrease of sp^3-bonds until eventually only t-BN films are obtained. As the use of higher temperatures is required to form c-BN with increasing ion energy, the failure to nucleate c-BN with an energy of 5 keV might also be related to an insufficiently high substrate temperature. However, in the view of the cylindrical thermal model, c-BN formation is related to the number of rearrangements in a thermal spike. Since this number strongly decreases for energy above about 3 keV, the effective c-BN growth regime is possibly limited to ion energies below 3 keV.

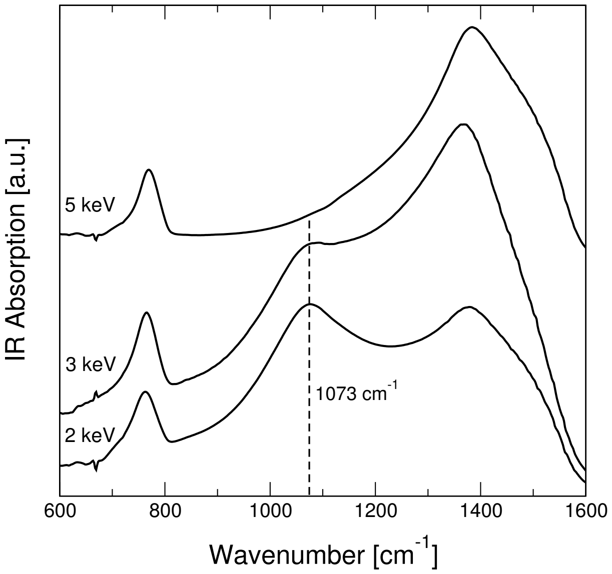

Figure 4.12: FTIR spectra of BN films, directly deposited on silicon substrates with $E_{ion} \geq$ 2 keV.

When depositing a BN film, ion impact on the silicon substrate initially leads to the formation of an unordered, sp^2-bonded phase. If the ion energy is within the limits required to nucleate c-BN (i.e. 125 eV $< E_{ion} <$ 2 keV), the incident ion beam would be capable of inducing sufficient compressive stress in the film to orient the t-BN planes perpendicular to the substrate surface. Yet, this effect is suppressed for temperatures below a specific, energy dependent value T_C, and the result would be a sample exhibiting an IR absorption spectrum as shown in figure 4.11a. This might also be due to accumulation of defects created by the impinging ions.

In the considered energy range between 125 eV and 2 keV, the range of $^{11}B^+$ and $^{14}N^+$ ions in t-BN is in the order of a few nanometers. The distance x between the mean ion range and the maximum of the vacancy distribution is similar to the c-BN case, i.e. $x_{c-BN}(E) = x_{t-BN}(E) = x(E)$. Since the ion flux for MSIB deposited films is almost constant, the diffusion time can be set to $t = 0.1$ s as well. To fill a formerly created vacancy (or move to the surface in the early stage of deposition) and avoid defect accumulation, an interstitial atom is again required to diffuse the distance $x(E)$ within the time $t = 0.1$ s. If one assumes a random walk as diffusion mechanism as well, the diffusion constant D_0 for t-BN is then given by equation (4.9). Orellana and Chacham [Ore01] investigated the ion beam induced formation of defects in boron nitride, and they stated that an interstitial boron atom in hexagonal BN is most likely to be found at an interlayer position forming metalliclike bonds with B atoms of adjacent layers. Assuming an interstitial atom resides between the basal planes and moves perpendicular to the c-axis (figure 4.13), the jump length can be estimated to $a = 2.9$ Å (assuming a distance $a_0 =$ 1.45 Å between two atoms in a t-BN hexagon), which results in a diffusion constant of $D_0 \approx 1.2 \times 10^{-2}$ cm^2/s. c-BN nucleation at a substrate temperature of $T_S =$ 150 °C is observed when using an ion energy of 500 eV, but not at $E_{ion} = 800$ eV (see figure 4.11). Therefore, the corresponding ion energy for a critical temperature of 150 °C is between 500 and 800 eV, and the ion range at those energies as calculated by SRIM is about $x \approx 1.3$ nm. Using equation (4.9), this results in a migration energy of $W_m \approx 0.9$ eV, which is in good agreement with the reports by Albe [Alb98]. In a theoretical study, he calculated the migration energies for boron and nitrogen diffusion in h-BN and obtained a value of about 1-2 eV. This value is significantly larger than the calculated migration energy for c-BN, which would

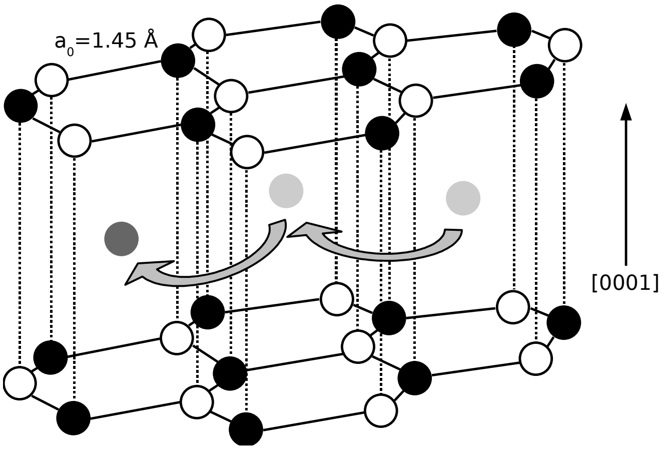

Figure 4.13: Schematic diagram of a simple random walk diffusion in h-BN, assuming an interstitial atom resides between the basal planes and moves perpendicular to the c-axis.

probably explain the need for a higher temperature for c-BN nucleation as compared to growth. If the substrate temperature is high enough, diffusion processes can be effective in annealing radiation damage. This is also in conformity with the findings by McCarty *et al.*. The temperature-driven diffusion of defects located between the t-BN basal planes would allow a compression of the t-BN lattice until eventually a 2:3 matching to the c-BN (111) planes is reached.

4.6 Summary

An energy-temperature dependence for c-BN nucleation has been found that exhibits features similar to c-BN growth. The previously assumed independence of ion energy and substrate temperature thresholds has been disproved; instead, the temperature has to be increased for increasing energies in order to nucleate the cubic phase. The simple diffusion model developed for c-BN growth at high ion energies has been applied to c-BN nucleation as well, and a diffusion constant and migration energy for self-diffusion in t-BN have been estimated to $D_0 \approx 1 \times 10^{-2}$ cm^2/s and $W_m \approx 0.9$ eV, respectively. As these values are significantly larger than for c-BN, a higher temperature at a given ion energy is required in order to nucleate c-BN as compared to its subsequent growth. Temperature-induced diffusion processes are seen responsible for annealing of radiation damage, avoiding defect accumulation

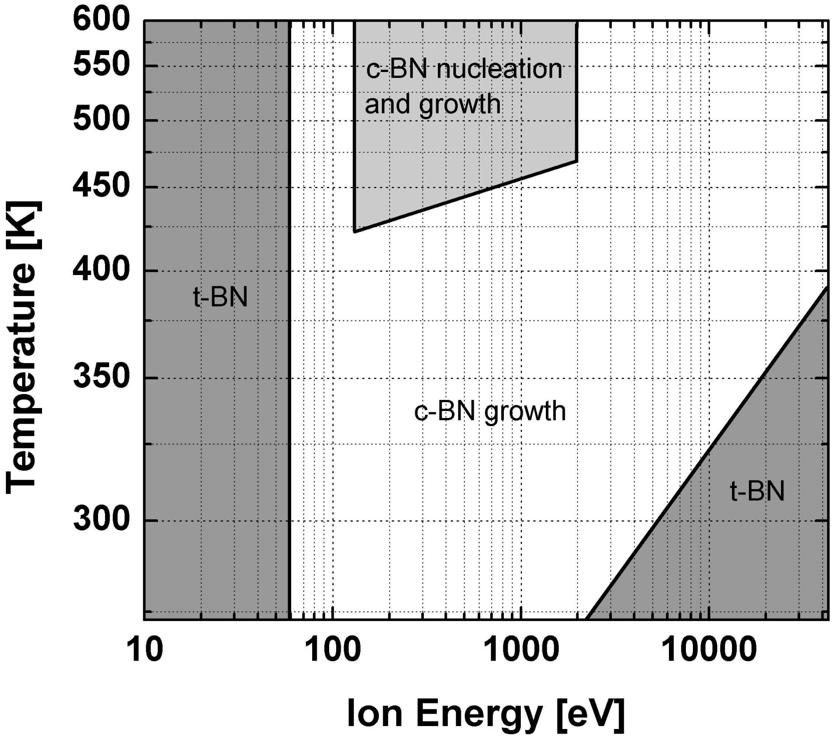

Figure 4.14: Phase diagram for BN films deposited via MSIBD, plotted as $\log_{10}(E)$ vs. $1/T$. c-BN nucleation is only possible in a narrow energy window ranging from 125 eV to about 2 keV. For higher ion energies the temperature has to be increased slightly in order to nucleate the cubic phase. c-BN growth on the other hand is possible for a wider range of both substrate temperature and ion energy. The low energy threshold is at $E_{ion} \approx 60$ eV. For ion energies up to about 5 keV, $T_S \approx$ RT is sufficient to grow c-BN, but for higher energies the temperature has to be increased according to equation (4.9).

and providing the boundary conditions required to nucleate the cubic phase.

With the available data it is now possible to extend the phase diagram for MISB deposited BN films (figure 3.1.1), and the revised diagram is shown in figure 4.14. Nucleation of c-BN is possible only within a narrow energy window ranging from 125 eV to about 2 keV. Increasing the ion energy requires a slight increase in substrate temperature as well; the respective dependence has been estimated from the obtained values for W_m and D_0 for t-BN. Cubic BN growth, on the other hand, can be maintained for a broader range of ion energies and substrate temperatures. The low energy threshold is around 60 eV, and up to an energy of about 3–5 keV the growth process seems to be relatively temperature-independent. For energies above approx. 5 keV, the substrate temperature has to be increased according to equation (4.9).

Chapter 5

Ion irradiation of c-BN films

5.1 Summary of foregoing results

Although ion bombardment during c-BN film growth is absolutely necessary to initiate (and maintain) cubic phase formation, it is also inevitably accompanied by the buildup of strong compressive stresses [McK93], which usually cause the destruction of a c-BN film due to delamination at thicknesses above approx. 100–200 nm. This limitation in thickness represents a serious barrier in the development of c-BN film technology preventing, e.g. its application as a superhard coating for cutting tools, where a thickness of the order of micrometers is required.

Consequently, much effort has been devoted to the problem of minimizing intrinsic stress. Several procedures have been proposed, such as deposition at elevated temperatures [Mir97b], growth at reduced or elevated ion energies [Hah97, Rei96b] or the use of a buffer layer [Mur90]. Post-deposition treatments have also been applied, e.g. thermal annealing [Don98] or irradiation with energetic ions [Wid97, Ull99, Fit00, Abe04]. The latter has been shown to be quite effective in reducing stress present in the as-prepared state, e.g. Widmeyer *et al.* observed a stress decrease from 20 GPa to 5 Gpa after irradiation with 350 keV Kr^+ ions [Wid97]. Ullmann *et al.* have used 1.1 MeV He, N, Ar, and Xe ions and were able to reduce the stress from 10 GPa down to 5 Gpa [Ull99]. Furthermore, Boyen *et al.* applied a procedure based on sequential film growth followed by subsequent ion bombardment (300 keV Ar^+), and succeeded in preparing films with thicknesses exceeding 1 μm [Boy99].

However, ion irradiation involves the risk of destroying the cubic phase and may lead to a c-BN to t-BN transformation if a certain ion fluence is exceeded. Ullmann *et al.* observed that the cubic phase remained stable upon irradiation with 2×10^{17} $\mathrm{He}^+/\mathrm{cm}^2$ at 1.1 MeV, but the use of 1.1 MeV Xe^+ ions has led to a transformation of the cubic into an sp^2-bonded phase already at a fluence of 10^{15} $\mathrm{ions/cm}^2$ [Ull98]. The latter corresponds to an accumulated defect concentration of about 1 dpa. As a consequence of their low mass, Helium ions are much more ineffective in inducing atomic displacements, since more than 99% of the energy is spent on electronic and not phononic excitations [Hof02]. Irradiation with 350 keV Kr^+ ions up to about 0.5 dpa has not induced a phase transformation either [Wid97]. A transformation from c-BN to sp^2-bonded BN has also been observed at defect concentrations as low as 0.025 dpa [YT02], however, in this study a few hundred keV C, F, and Si ions were used. Thus, a phase transformation due to a change of stoichiometry cannot be excluded, especially, since no elemental analysis was performed after implantation.

Hence, it seems reasonable to assume that c-BN is stable upon ion irradiation up to a critical defect concentration of about 1 dpa. However, most experiments carried out so far have utilized ion energies that led to ion ranges larger than the c-BN film thickness, resulting in an irradiation of the t-BN interlayer. As the c-BN/t-BN boundary has been shown to be unstable upon ion bombardment, the observed c-BN to t-BN transformation might not be due to an instability of the c-BN film, but because of the interface irradiation.

In this chapter the stability of c-BN films upon ion irradiation is examined. $^{40}\mathrm{Ar}^+$ and $^{14}\mathrm{N}^+$ ions with energies ranging from 10 to 30 keV have been used. It will be shown that c-BN films are extremely stable against ion bombardment. In addition, a transformation from c-BN to t-BN can be induced by irradiating the t-BN/c-BN interface with fluences generating a accumulated defect concentration of about 1 dpa.

5.2 Experimental results

5.2.1 Interface instability

In order to verify the observed c-BN/t-BN interface instability described in section 3.2.1, two c-BN samples were prepared at a substrate temperature of 250 °C and with an ion energy of 500 eV. The deposited charges were 0.15 C for the first sample and 0.33 C for the second one, resulting in film thicknesses of about 40 nm and 80 nm, respectively. The films were then irradiated with 30 keV $^{40}\mathrm{Ar}^{+}/\mathrm{cm}^{2}$ to a fluence of 1×10^{16} cm^{-2}. An SRIM calculation yields a mean ion range of about 20 nm and a maximum range of approx. 35 nm, hence in the case of the thinner sample, the Ar ions reached the t-BN/c-BN interface. On the other hand, the c-BN layer of the second sample was thick enough to prevent an irradiation of the t-BN layer. Sputtering effects have also been calculated by SRIM, resulting in a sputter yield of $s \approx 2.4$. Hence, sputter effects are negligible, since a fluence of 1×10^{16} ions/cm^2 reduces the film thickness by only about 4%.

Both samples were then analyzed with FTIR and the spectra are displayed in figure 5.1. Clearly visible is the transition from cubic to sp^2-bonded BN in the spectrum shown in figure 5.1a for the thinner sample. The t-BN absorption peaks are very pronounced, whereas the c-BN absorption has almost completely vanished. The second sample, however, shows no sign of a phase transformation upon ion bombardment. Instead, only a slight increase of the sp^2-stretching mode as well as a shift of about 14 wavenumbers of the position of the reststrahlen band has occured. The latter points to a significant reduction of compressive stress within the sample, similar to the effects observed for c-BN growth with high ion energies (section 3.2). Thus, the transformation from sp^3- to sp^2-bonded BN is unmistakebly related to the instability of the t-BN/c-BN interface.

However, the mechanisms leading to the cubic phase destruction upon interface irradiation remain unclear. In order to find out whether the transformation starts from the t-BN/c-BN boundary and how quickly it will advance, a c-BN film identical to the first one was prepared. A substrate temperature of 250 °C, an ion energy of 500 eV, and a deposited charge of $Q = 0.15$ C were chosen, leading to a film thickness of about 40 nm. The sample was then analyzed *in-vacuo* using x-ray

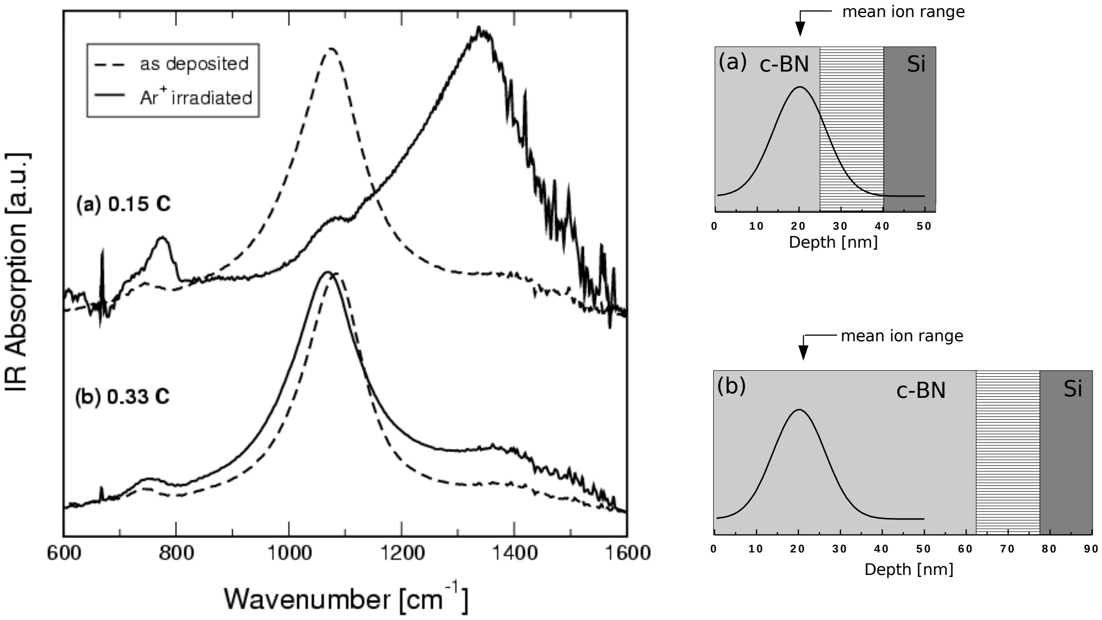

Figure 5.1: FTIR spectra of two c-BN films that have been irradiated with 1×10^{16} $^{40}\mathrm{Ar}^+/\mathrm{cm}^2$. (a) Total deposited charge for this sample was $Q = 0.15$ C, corresponding to a film thickness of about 40 nm, including an about 10-15 nm thick t-BN interlayer. The mean range of $^{40}\mathrm{Ar}^+$ ions in c-BN is about 20 nm with a maximum ion range of approx. 35 nm. Thus, some ions have penetrated the c-BN film and have irradiated the t-BN layer, resulting in an almost complete transformation of sp^3-bonded BN into t-BN. (b) Total deposited charge was $Q = 0.33$ C, resulting in a film thickness of about 80 nm. The c-BN film remained intact upon irradiation.

photoelectron spectroscopy (XPS) by measuring the plasmon energy loss of the B1s peak on 6 equidistant positions over the entire sample surface (figure 5.2, right hand side). The plasmon energies are displayed in figure 5.2 (black data points). A value of $E_p = 30 \pm 0.5$ eV has been measured, which confirms a high cubic phase content within the near surface region of the film.

The sample was then cooled down to room temperature in UHV and subsequently irradiated with 30 keV $^{40}\mathrm{Ar}^+$ ions. The ion current density was set to $I = 6$ $\mu\mathrm{A/cm}^2$, and the motorized shutter installed at ADONIS was moved into the ion beam with a speed of $v \approx 0.2$ mm/s. After a time of 80 s, the shutter had covered the entire sample (diameter $d \approx 15$ mm), thus, the ion fluence has increased gradually from 0 to 3×10^{15} cm^{-2} over the sample area. The plasmon energies were then

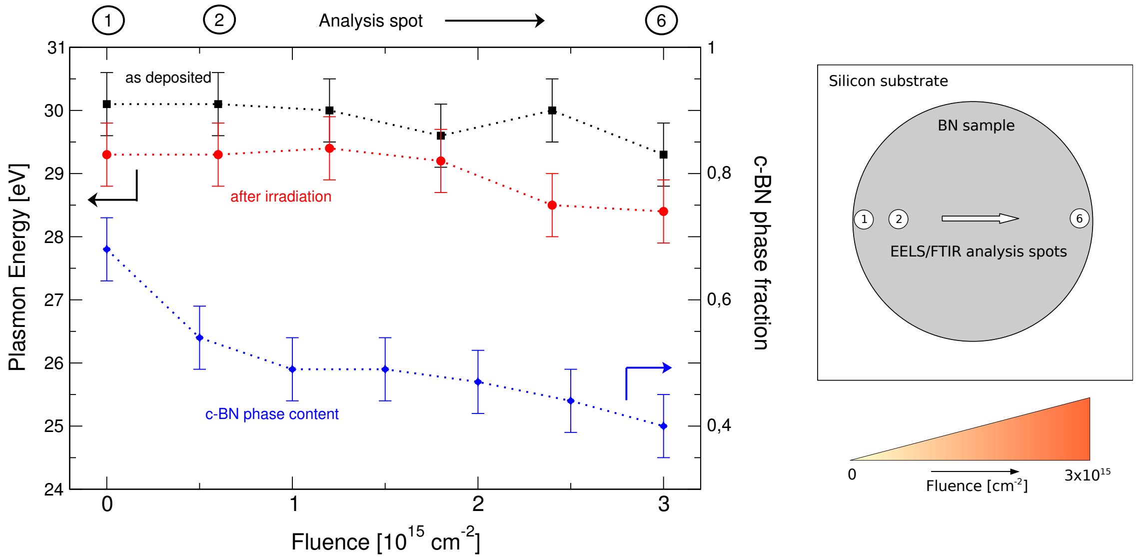

Figure 5.2: Plasmon energy and cubic phase content as a function of ion fluence. The t-BN/c-BN interface was irradiated with 30 keV ^{40}Ar^{+} ions. By using a motorized shutter, the ion fluence was gradually increased from 0 to 3×10^{15} cm^{-2} over the sample area. EELS (*in-vacuo*) and FTIR (*ex-vacuo*) measurements were performed at the positions labeled 1–6.

again measured at the exact same spots and are shown in figure 5.2 as represented by the red circles. They are generally about 0.5 eV smaller as compared to the as-deposited sample, which might be due to surface contaminations that occured during the cool down. An almost constant value of about $E_p = 29 \pm 0.5$ eV has been measured. Hence, the cubic phase content at the surface of the sample did not change significantly upon ion irradiation.

FTIR spectroscopy was applied *ex-situ* to measure the cubic phase content within the bulk of the film. The IR beam was rastered over the sample area, which thus allows for an extraction of the c-BN content as a function of ion fluence from the respective spectra. As can be seen from figure 5.2, the c-BN content decrases gradually from about $70 \pm 5\%$ down to approx. $40 \pm 5\%$ with increasing ion fluence. However, as the plasmon energy remains rather constant, it is obvious that an irradiation of the t-BN/c-BN boundary leads to destruction of the cubic phase, which starts from the interface region and proceeds towards the film surface.

The experiment was repeated with an ion fluence of up to 1×10^{16} cm^{-2}, and the FTIR and EELS results are shown in figure 5.3. Again, the plasmon energy for the as-deposited sample remains constant at $E_p = 30 \pm 1$ eV. After irradiation, however,

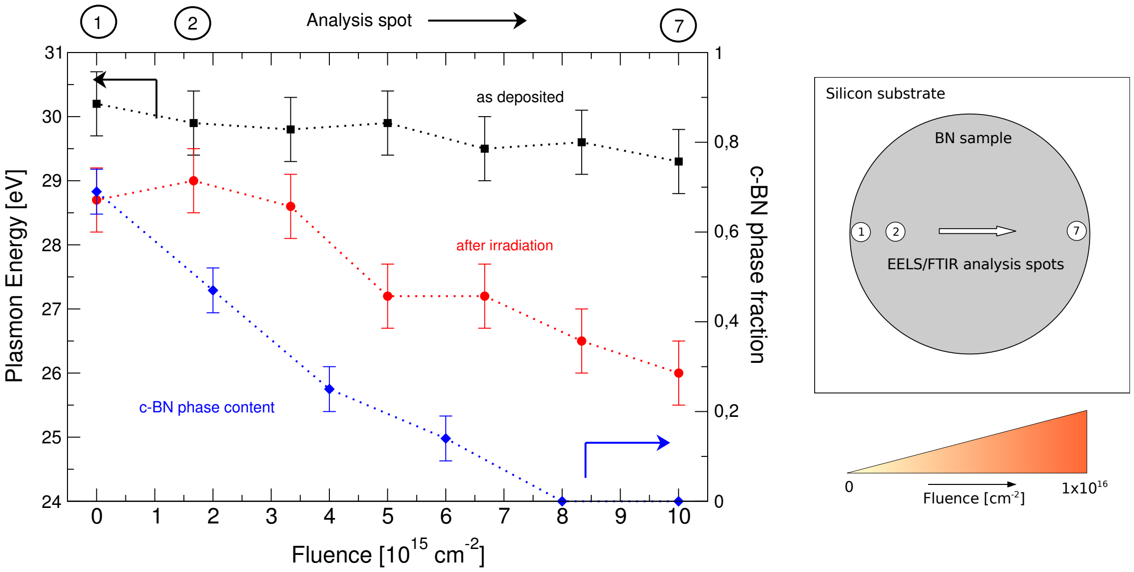

Figure 5.3: Plasmon energy and cubic phase content as a function of ion fluence. The t-BN/c-BN interface was irradiated with 30 keV ^{40}Ar^{+} ions. By using a motorized shutter, the ion fluence was gradually increased from 0 to 1×10^{16} cm^{-2} over the sample area. EELS (*in-vacuo*) and FTIR (*ex-vacuo*) measurements were performed at the positions labeled 1–7.

it has dropped to $E_p = 29 \pm 1$ eV and decreases further down to 27.5 ± 0.5 eV after a fluence of 3×10^{15} cm^{-2} is exeeded. At the same time, the cubic phase fraction decreases almost linearly from about $70 \pm 5\%$ to 0% at a fluence of 8×10^{15} cm^{-2}. Once the cubic phase fraction reaches zero, the plasmon energy decreases further to about 26 ± 0.5 eV, which is probably related to an increasing amount of disorder that is induced by the ion bombardment.

Apparently, a fluence of $6 - 8 \times 10^{15}$ ^{40}Ar^{+}/cm^{2} is sufficient to transform the entire cubic film into an sp^2-bonded phase. However, as can be seen from figure 5.2, the destruction already sets in at fluences as low as about 1×10^{15} cm^{-2}, which corresponds to an accumulated defect concentration of about 1 dpa, and is thus in good agreement with the values reported by other groups [Ull98, Wid97, Abe04].

The mechanism leading to a destruction of the cubic phase may also be related to diffusional annealing processes as described in section 4.5. Figure 5.4 shows a schematic diagram of an about 35 nm thick c-BN film (including a 15 nm thick t-BN layer), which is irradiated with 30 keV ^{40}Ar^{+} ions. The mean ion range is about 20 nm, and the corresponding depth distribution has been included in the figure as represented by the squared symbols. The ion-beam-induced damage

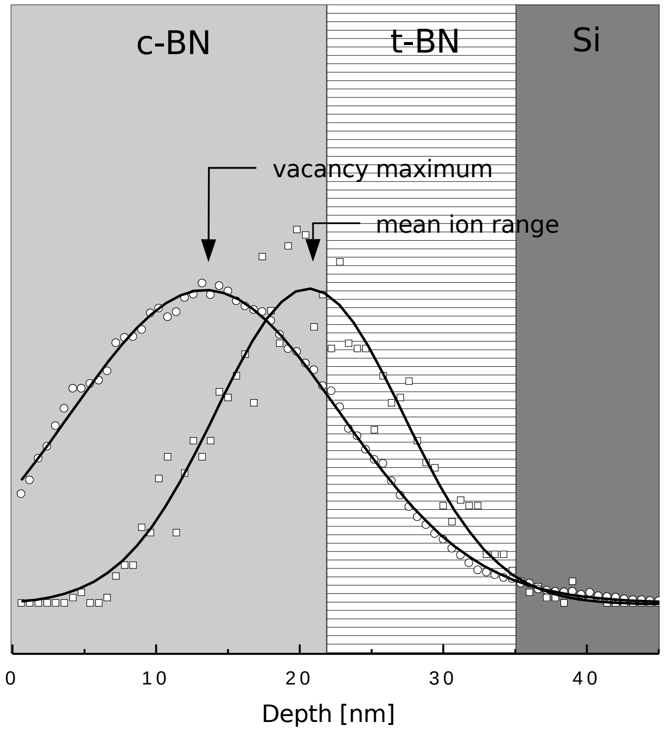

Figure 5.4: Schematic diagram showing the position of the vacancy profile and ion distribution within a thin c-BN film when irradiated with 30 keV ^{40}Ar^{+} ions.

profile has its maximum at a depth of approx. 12 nm (circles). Hence, a substantial amount of ions comes to rest within the t-BN layer while most defects are created within the c-BN film. If one applies the picture of diffusional annealing processes being responsible for a suppression of defect accumulation, it is obvious that a significant amount of interstitials would have to migrate from the t-BN into the c-BN layer in order to annihilate with vacancies. However, this process seems to be unfavorable from an energetic point of view. Albe calculated the formation energies for nitrogen and boron interstitials in c-BN and h-BN [Alb98] and reported values of the order of 20-28 eV (depending on the lattice site) in c-BN and about 10 eV in h-BN. Hence, diffusion of atoms from the t-BN into the c-BN layer requires the atoms to overcome a substantial energy barrier. Diffusion processes therefore might be severely hampered, leading to an accumulation of defects near the t-BN/c-BN boundary. As a consequence, the cubic phase would be transformed from the bottom up into a rather unordered, sp^2-bonded phase.

5.2.2 Stability of c-BN films upon ion irradiation

As the t-BN/c-BN boundary has been shown to be the weak point upon ion bombardment, the following ion irradiation experiments have been performed on c-BN films whose thicknesses exceeded the range of the bombarding species. All films were deposited at $T_S = 250$ °C and with $E_{ion} = 500$ eV, and then analyzed using FTIR spectroscopy. They were then irradiated with $^{40}\mathrm{Ar}^+$ and $^{14}\mathrm{N}^+$ ions, respectively, at room temperature with ion energies ranging from 10 keV to 30 keV. Ion fluences of 10^{15}, 10^{16}, 10^{17}, and 10^{18} cm^{-2} have been used. Subsequent to each irradiation step, the c-BN phase content was measured again by IR spectroscopy. As the analysis had to be performed *ex-situ*, EELS and AES were not performed because of surface contaminations that would falsify the measurement. Nitrogen and argon were used as species in order to rule out any changes to stoichiometry within the c-BN, which may also induce a cubic to sp^2-BN transformation. Both elements are commonly used during ion beam assisted deposition of c-BN films and it is known that over-stoichiometric nitrogen becomes volatile and diffuses out to the surface [Mir97a]. For the case of argon, Deyneka *et al.* [Dey03] observed an argon concentration of only $C_{Ar} = 0.3$ at.% within the c-BN layer, although the film was grown using the dual beam IBAD technique, i.e. the growing film was bombarded simultaneously with Ar and N ions.

Figure 5.5 shows the FTIR spectra of a c-BN film that has been irradiated with $10^{15} - 10^{18}$ $^{40}\mathrm{Ar}^+/\mathrm{cm}^2$ at an ion energy of 30 keV. Apparently, the c-BN film remained stable up to a fluence of 10^{16} cm^{-2} as for the corresponding spectrum the c-BN peak at about 1070 cm^{-1} is still very distinct. The peak position shifts from about 1085 cm^{-1} for the as-deposited sample to 1070 cm^{-1} after irradiation with 10^{16} cm^{-2}, indicating a significant release of compressive stress. However, the FWHM of the peak increases from about 154(5) cm^{-1} to 189(5) cm^{-1}, which can be attributed to a decrease in crystal sizes and overall crystalline quality. An interesting observation is that upon ion irradiation with fluences exceeding 10^{15} cm^{-2} the height of the c-BN reststrahlen absorption peak of the sample strongly decreases, although the cubic phase content as calculated from the ratio of the c-BN and t-BN peak areas remains high. After irradiation with a fluence of 10^{17} cm^{-2} the c-BN reststrahlen absorption is still visible, but the sample also exhibits an increased

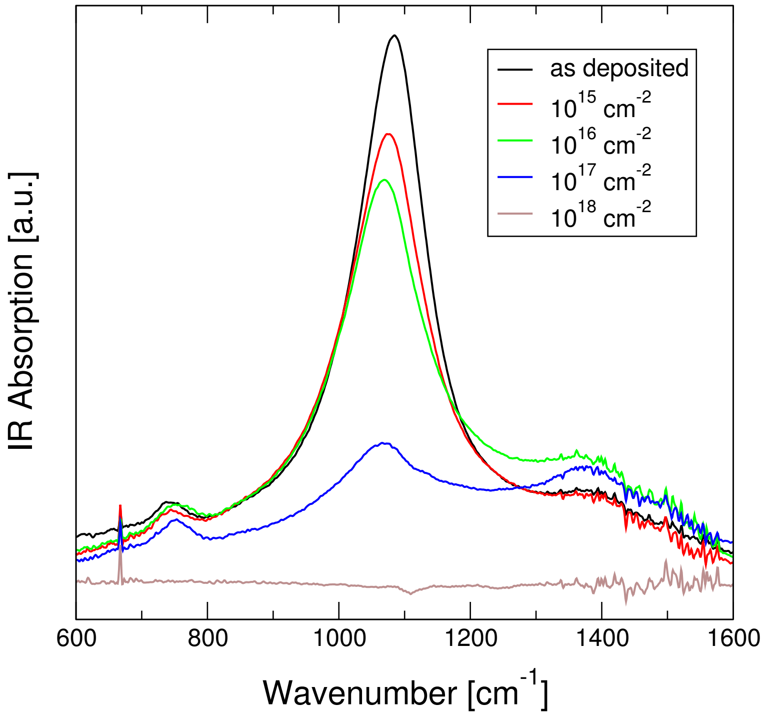

Figure 5.5: FTIR spectra of a c-BN film, recorded after subsequent ion irradiation with 10^{15} – 10^{18} ^{40}Ar^{+}/cm^{2} with E_{ion} = 30 keV. The film remained stable up to a fluence of 10^{16} cm^{-2}.

t-BN absorption. Hence, a significant amount of c-BN has been transformed into sp^2-bonded BN, probably because of a substantial number of defects that have been created due to ion bombardment. Finally, at a fluence of 10^{18} cm^{-2} the film has been completely sputtered.

The experiment was repeated with nitrogen instead of argon as the bombarding species, and the IR spectra acquired after each irradiation step are displayed in figure 5.6. The same trend as for the case of Ar bombardment can be noticed, i.e. the IR intensity decreases with increasing ion fluence, and the c-BN absorption peak shifts from 1075 cm^{-1} to 1070 cm^{-1} after irradiation with 10^{17} N^{+}/cm^{2}. The peak width increases from 135(5) cm^{-1} to 180(5) cm^{-1}, again indicating a decrease in compressive stress, which, however, seems to be accompanied by a deteriorating crystalline quality. In contrast to Ar irradiation, the c-BN film remained stable up to irradiation with 10^{17} N^{+}/cm^{2}. After a fluence of 10^{18} cm^{-2} the complete film had been removed due to sputtering.

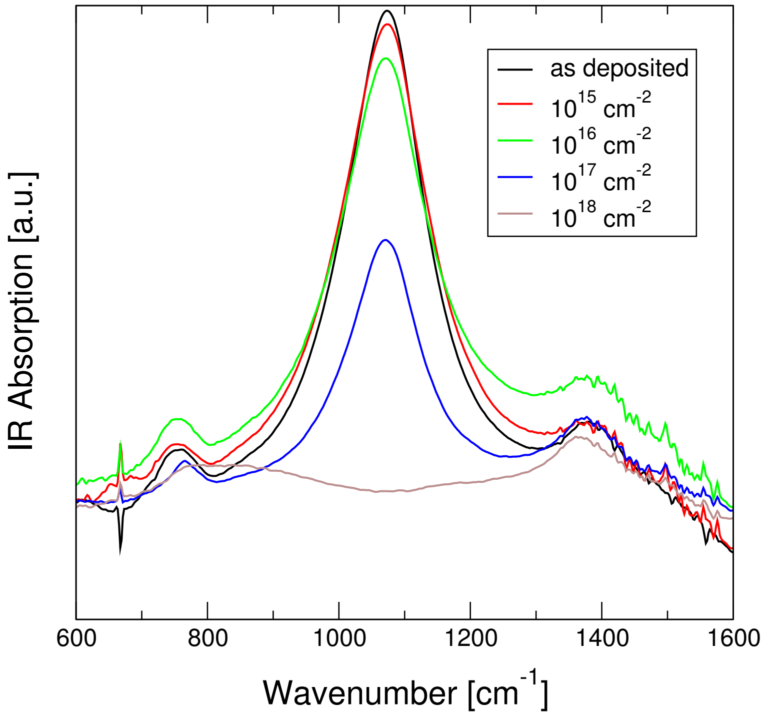

Figure 5.6: FTIR spectra of a c-BN film, recorded after subsequent ion irradiation with 10^{15} – -10^{18} $^{14}N^{+}/cm^{2}$ with E_{ion} = 30 keV. The film remained stable up to a fluence of 10^{17} cm^{-2}.

Figure 5.7 summarizes the results obtained from irradiation experiments and displays the cubic phase content of BN films that have been bombarded with N^{+} and Ar^{+} ions as a function of ion fluence. Ion energies between 10 and 30 keV have been used, and the c-BN content has been determined by calculating the ratio of the c-BN and t-BN peak areas as described in section 2.2.1. For the case of nitrogen irradiation, the cubic phase content remains high up to a fluence of 10^{17} cm^{-2}, whereas, Ar bombardment leads to a significant destruction of the cubic phase already at a fluence of about 10^{16} cm^{-2}. These fluences correspond to accumulated defect concentrations of about 8 dpa and 20 dpa for argon and nitrogen bombardment, respectively. Hence, if an irradiation of the c-BN/t-BN interface is avoided, the cubic BN phase turns out to be extremely stable upon ion bombardment. However, as can be seen from figures 5.5 and 5.6, a significant reduction of c-BN absorption intensity is visible already at a fluence of 10^{15} cm^{-2}, which corresponds to approx. 1 dpa. This effect is presumably a result of an increased amount of defects that is

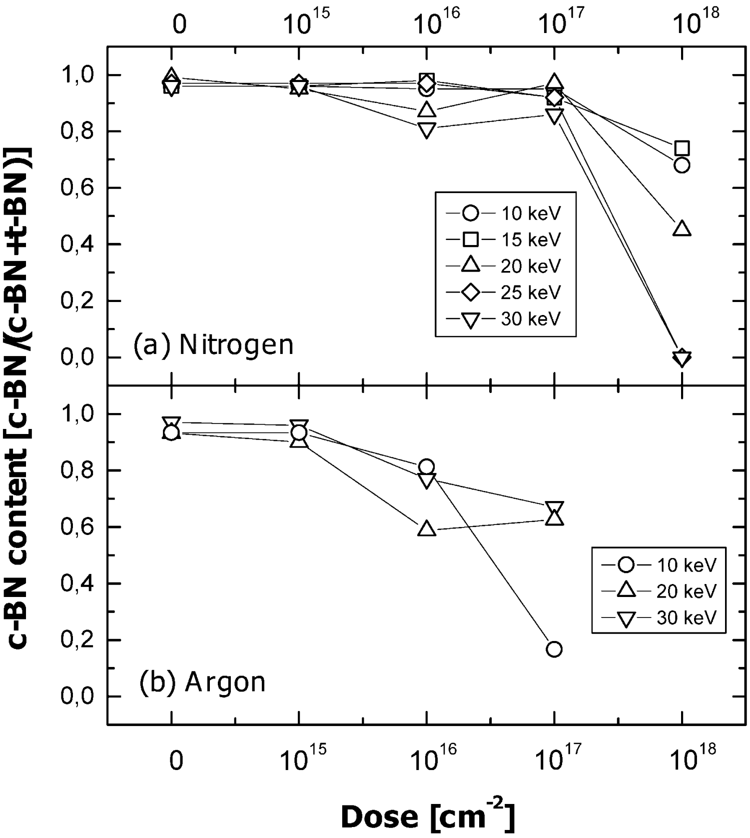

Figure 5.7: Cubic BN phase content, extracted from FTIR measurements, of BN films irradiated with (a) N^+ and (b) Ar^+ ions using different ion energies as a function of ion fluence.

accompanied by a change of crystallinity. A recent study by Zhang *et al.* supports this assumption [Zha05]. The authors have irradiated 350 nm thick c-BN films with 300 keV Ar^+ ions and observed a decrease of the c-BN peak height with increasing ion fluence as well. The c-BN content, on the other hand, remained high up to a fluence of about 4×10^{15} cm^{-2}, which, however, was accompanied by a significant increase of peak width. In a detailed HRTEM study, Zhang *et al.* observed a decrease in c-BN crystal size upon ion bombardment, which was interpreted as "cutting large crystals into smaller crystallites" as a consequence of ion bombardment [Zha05]. Moreover, they found that c-BN films of a high crystalline quality including high concentrations of the cubic phase are more stable against ion irradiation than samples of more poor crystallinity. This is also in conformity with the results presented above, since a film of poor crystallinity is expected to exhibit an

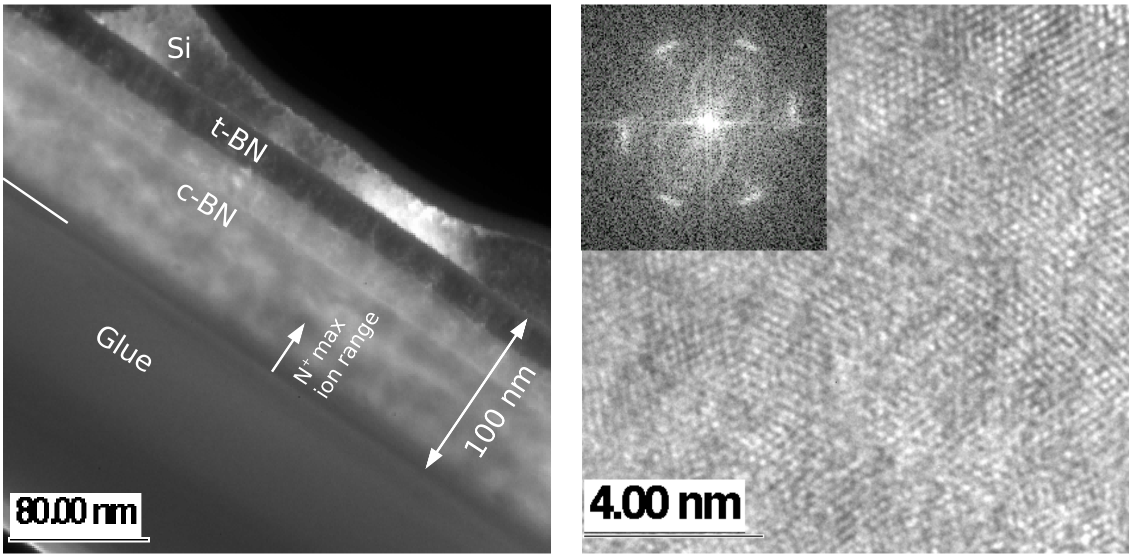

Figure 5.8: *Left:* Dark-field TEM image of a c-BN sample that has been irradiated with 15 keV $^{14}N^+$ ions at a fluence of 10^{17} cm^{-2}. The total film thickness is about 100 nm and no ion-beam induced transformation of c-BN into sp^2-bonded BN is visible. The maximum range of 15 keV N^+ ions is indicated by the arrow (about 34 nm). *Right:* HRTEM micrograph of a c-BN crystallite in the upper film region. The FFT image in the inset shows cubic reflection patterns only.

increased amount of sp^2-bonded material between the cubic grains, which would thus resemble a c-BN/t-BN interface. Consequently, this may act as a nucleation site for the ion-induced transformation of c-BN into t-BN leading to a strongly reduced stability of the majority c-BN phase against irradiation.

A TEM analysis was carried out on a c-BN sample that had been irradiated with 15 keV $^{14}N^+$ ions to a fluence of 1×10^{17} cm^{-2}. The dark-field image displayed in figure 5.8 shows an approx. 100 nm thick BN film on top of a silicon substrate. Although columnar c-BN growth is barely visible, it is clear that the cubic film extends up to the surface, and no destruction or transformation due to ion bombardment can be noticed. This is further supported by the HRTEM micrograph that has been recorded at the near surface region of the sample. The corresponding FFT image clearly shows the c-BN (111) reflections, but there is no indication of sp^2-bonded BN. Hence, the TEM analysis corroborates the conclusions drawn from the FTIR measurements. In addition, considering a film thickness of about 110 nm prior to irradiation, it is obvious that sputter effects are indeed only a minor effect with respect to the observed IR intensity loss, and a fluence of 1×10^{17} N^+/cm^2 decreases the film thickness by only about 10%.

5.3 Simulation of IR spectra

In order to investigate the mechanisms leading to a decrease of absorption intensity, it has been attempted to describe the measured IR spectra by using a classical Lorentz oscillator model. This model is well suited to describe the interaction of electromagnetic waves with valence electrons or ions in solid matter [Sch02]. If matter is irradiated with electromagnetic waves, its response is given by the dielectric function $\epsilon(\omega)$, which can be separated into a real (ϵ') and an imaginary part (ϵ''):

$$\epsilon = \epsilon' + i\epsilon'' \tag{5.1}$$

For the case of ionic crystals, the dielectric function can be expressed as a sum over the electric susceptibilities of all possible excitations, i.e.

$$\epsilon(\omega) = 1 + \chi_{ve}(\omega) + \chi_{fc}(\omega) + \chi_{ph}(\omega). \tag{5.2}$$

The contribution of free charge carriers χ_{fc} can be neglected for ionic crystals [Sch02]. The term χ_{ve} is caused by valence electrons and is for mid-IR light in good approximation real and independent of the frequency. It is therefore often referred to as high-frequency dielectric constant

$$\epsilon_\infty = 1 + \chi_{ve}. \tag{5.3}$$

Within the Lorentz oscillator model, contribution of phonons is given by

$$\chi_{ph}(\omega) = \frac{S}{\omega_0^2 - \omega^2 - i\gamma\omega}, \tag{5.4}$$

where S is the oscillator strength, γ is the damping constant, and $\omega_0 = \omega_{TO}$ is the transverse optical resonance frequency. Thus, the dielectric function is given by

$$\epsilon(\omega) = \epsilon_\infty + \frac{S}{\omega_0^2 - \omega^2 - i\gamma\omega}. \tag{5.5}$$

In the presence of more than one oscillator, the susceptibility can be calculated from the sum over the contribution of each oscillator:

$$\epsilon(\omega) = \epsilon_\infty + \sum_{j=1}^{N} \frac{S_j}{\omega_{j,0}^2 - \omega^2 - i\gamma_j\omega}. \tag{5.6}$$

A comparison with (5.1) then yields

$$\epsilon' = \epsilon_\infty + \frac{S(\omega_0^2 - \omega^2)}{(\omega_0^2 - \omega^2)^2 + \gamma^2\omega^2} \tag{5.7}$$

$$\epsilon'' = \frac{S\gamma\omega}{(\omega_0^2 - \omega^2)^2 + \gamma^2\omega^2} \tag{5.8}$$

If one defines the complex refractive index as

$$N = n + i\kappa = \mathrm{Re}(\sqrt{\epsilon}) + i \cdot \mathrm{Im}(\sqrt{\epsilon}), \tag{5.9}$$

with n as the refractive index and κ as the extinction coefficient, the optical constants can be calculated from the dielectric function according to:

$$n = \sqrt{\frac{1}{2}\left(\sqrt{\epsilon'^2 + \epsilon''^2} + \epsilon'\right)} \tag{5.10}$$

$$\kappa = \sqrt{\frac{1}{2}\left(\sqrt{\epsilon'^2 + \epsilon''^2} - \epsilon'\right)} \tag{5.11}$$

The refraction index n describes the ratio of the speed of light in vacuum to the phase velocity of the wave within the material, while the extinction coefficient κ causes the wave intensity to decrease exponentially when entering the medium.

The optical properties of c-BN and h-BN have been investigated by Geick *et al.* [Gei66], Gieliesse *et al.* [Gie67], and Eremets *et al.* [Ere95] by using transmittance and reflectance spectroscopy in the UV/visible and IR region as well as Raman spectroscopy. The obtained spectra for c-BN were found to be describable by one oscillator within the Lorentz model, while simulation of the h-BN spectra required the use of two oscillators. In addition, as h-BN is optically anisotropic, the authors examined the optical properties by using light that was polarized either perpendicular or parallel with respect to the c-axis. The published optical properties and oscillator parameters are summarized in data table 5.1.

Figure 5.9 shows the IR spectrum of a c-BN film, deposited with E_{ion} = 500 eV, T_S = 250 °C, and a total charge of Q = 0.33 C. The spectrum has been fitted by using an optic two layer model in order to account for the t-BN/c-BN layer sequence. One oscillator was found to be sufficient to reproduce the shape of the c-BN absorption line; whereas, the t-BN absorbtion requires the use of two oscillators

	ϵ	ν_{TO} [cm^{-1}]	ν_{LO} [cm^{-1}]	S [cm^{-2}]	γ [cm^{-1}]
h-BN $E \parallel c$	$\epsilon_\infty = 4.1$ $\epsilon_{\omega=0} = 5.09$	783 1510	828 1595	3.26×10^5 1.04×10^6	8.0 80
h-BN $E \perp c$	$\epsilon_\infty = 4.95$ $\epsilon_{\omega=0} = 7.04$	767 1367	778 1610	1.23×10^5 3.49×10^6	35 29
c-BN	$\epsilon_\infty = 4.46$ $\epsilon_{\omega=0} = 6.8$	1055.7	1340	2.61×10^6	40.3

Table 5.1: Optical properties and oscillator parameters of h-BN and c-BN (taken from refs. [Gei66, Ere95, Sch02]).

because of the two visible TO modes. Initial values for the oscillator parameters were taken from table 5.1, and, additionally, the layer thicknesses have been allowed as fit parameters as well.

As can be seen in figure 5.9, a Lorentz oscillator model is able to reproduce the shape of the absorption profile very well. Layer thicknesses of $d_{t-BN} = 21(5)$ nm and $d_{c-BN} = 71(8)$ nm have been obtained, which are in good agreement with the deposited charge and SRIM simulations. An oscillator strength $S = 2.1(2) \times 10^6$ cm^{-2} and a damping constant $\gamma = 115(5)$ cm^{-1} for the c-BN absorption have been derived from the fit. These values differ from the ones reported by Eremets *et al.* (see table 5.1), however, the authors investigated single-crystalline c-BN samples; whereas, the films deposited in this work are nanocrystalline, and the discrepancies are thus not surprising. On the other hand, S and γ are in reasonably good agreement with the values found by Scheible [Sch02], who analysed c-BN films by means of *in-situ* FTIR spectroscopy in reflectance mode.

Figure 5.10a displays the calculated real (ϵ') and imaginary (ϵ'') part of the dielectric function of the c-BN film in the region of the resonance frequency. The real part of ϵ increases initially with increasing wavenumbers and shows in the vicinity of ω_0 a maximum on the low-frequency side and a minimum on the high-frequency side, for which ϵ' becomes negative. ϵ' then increases and reaches the value of ϵ_∞, which is due to absorption caused by valance electrons. The frequency range for which ϵ' is negative is called reststrahlen band. In this region the imaginary part of ϵ has a

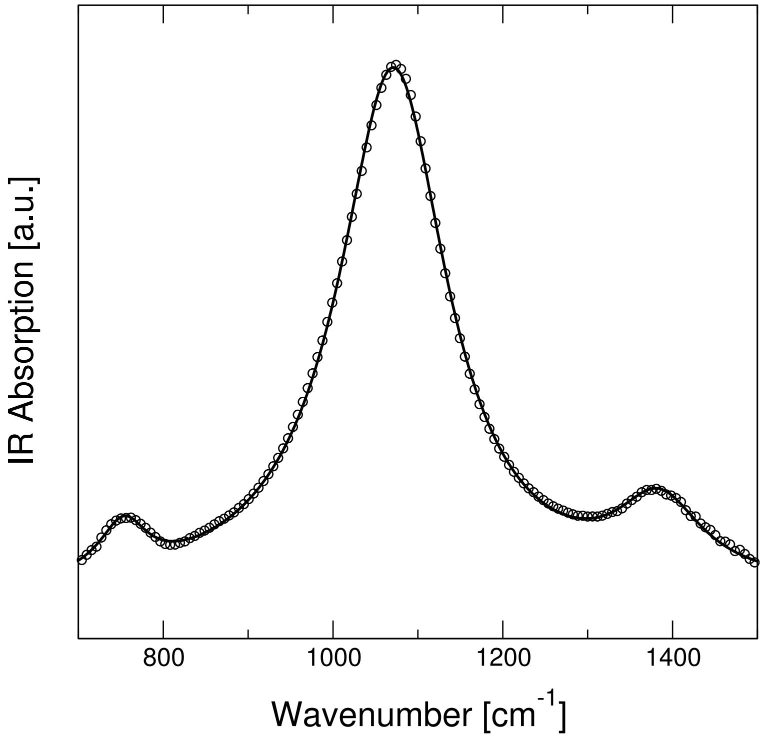

Figure 5.9: Measured (circles) and calculated (solid line) IR spectrum of a c-BN film. The data points have been fitted according to equations (5.7) and (5.8).

Lorentzian shape with a full width at half maximum of γ. The maximum of ϵ'' is located at ω_0.

Refractive index n and extinction coefficient κ have been calculated from the dielectric function according to equations (5.10) and (5.11), respectively, and are shown in figure 5.10b.

The FTIR spectra shown in figure 5.6 for a c-BN film irradiated with 30 keV $^{14}N^+$ ions have been fitted according to the procedure explained above as well. However, the fit is very sensitive to the film thickness, since the absorption intensity is also dependent on the film thickness as described by the Lambert-Beer law. Therefore, the thickness was not used as a fit parameter, but has been set to the value calculated for the as-deposited sample ($d = 71(8)$ nm) and decreased manually for each film according to sputter losses as given by SRIM simulations. The extinction coefficients κ were derived from the fit and are displayed in figure 5.11. The maximum

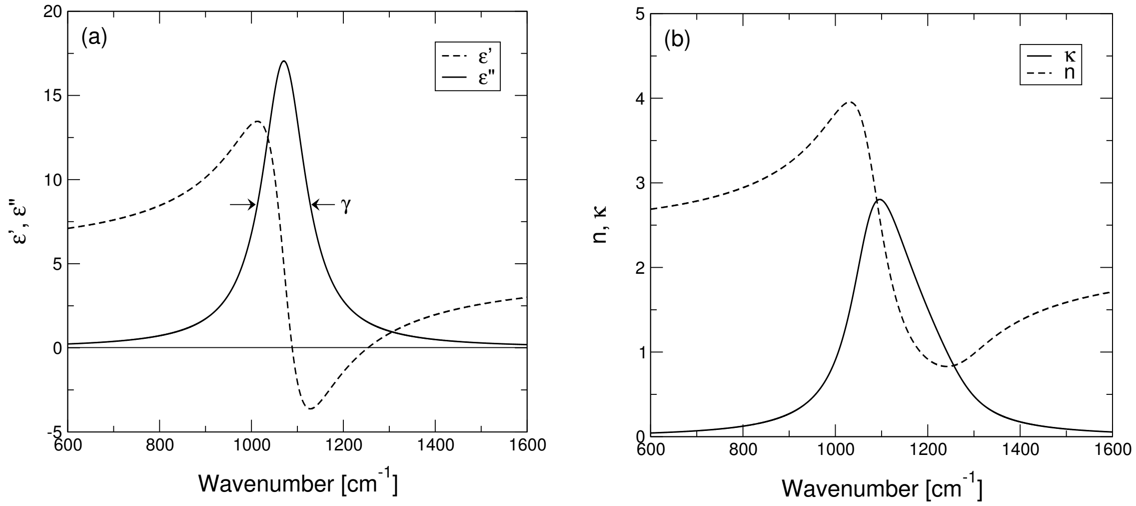

Figure 5.10: (a) Real and imaginary part of the dielectric function of a Lorentz oscillator in the region of the resonance frequency. The data has been derived by fitting the IR spectrum of a c-BN film according to equations (5.7) and (5.8). (b) Refractive index and extinction coefficient as calculated from the dielectric function using equations (5.10) and (5.11).

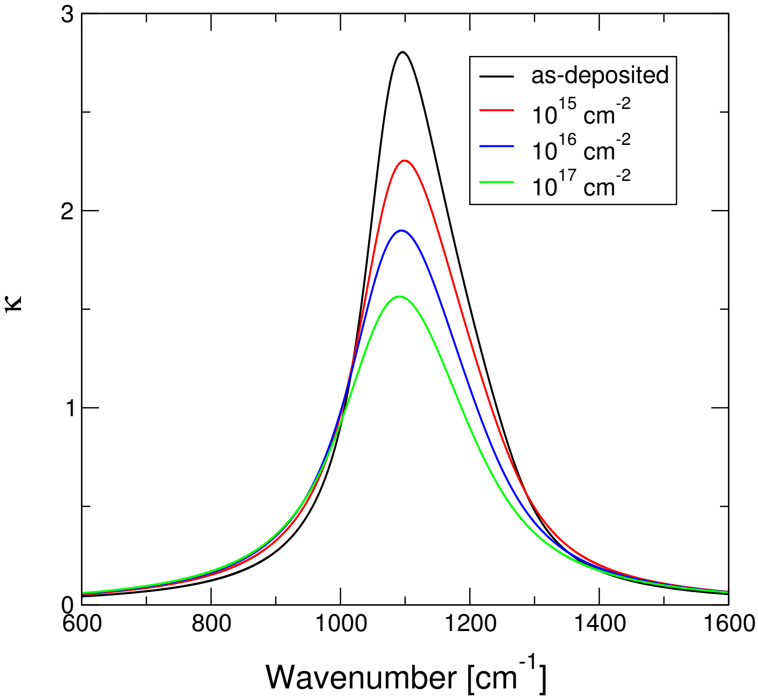

Figure 5.11: Extinction coefficient κ of a c-BN film as a function of irradiation fluence.

of κ decreases with increasing ion fluence, which is in agreement with the observed loss of IR peak intensity. At the same time, the damping constant γ increases from $\gamma = 115(5)$ cm^{-1} for the as-deposited sample to $\gamma = 195(7)$ cm^{-1} after irradiation with a fluence of 10^{17} cm^{-2}. In addition, the oscillator strength decreases slightly from $S = 2.1(2) \times 10^6$ cm^{-2} down to $1.8(3) \times 10^6$ cm^{-2}.

The damping constant is related to the phonon lifetime via $\gamma = 1/\tau$. In ideal crystals, the lifetime of optical phonons is limited mainly by the decay of an optical phonon into two accustic phonons through normal processes [Sri90]. In real crystals, however, the interaction of photons with phonons is additionally disturbed by scattering processes of phonons on crystal defects, such as grain boundaries, dislocations, stacking faults, or impurities. For the as-deposited sample, a damping constant $\gamma \approx 115$ cm^{-1} yields a phonon lifetime of $\tau \approx 0.3$ ps. By using a sound velocity in c-BN of $v_s = 1.5 \times 10^4$ m/s, the phonon mean free path length calculates to $l \approx 5$ nm. After irradiation with a fluence of 1×10^{17} cm^{-2}, γ has increased to about 195 cm^{-1}, which results in a free path length of approx. 2.5 nm. Hence, the assumption of an increased defect density due to ion irradiation seems reasonable, since a decreasing mean free path length indicates a pronounced phonon scattering at either point defects or crystal distortions, which gives rise to a decreasing crystallite size upon ion irradiation.

5.4 Stress measurements

The shift of the c-BN reststrahlen absorption in the IR spectra displayed in figures 5.6 and 5.5 points to a significant release of compressive stress within the film upon ion irradiation. In order to quantify this effect, a c-BN film was prepared at $T_S = 250$ °C, $E_{ion} = 500$ eV, and $Q = 0.35$ C on a silicon cantilever. The stress was analyzed by measuring the bending of the cantilever with an optical microscope. This value δ can then be used to calculate the compressive stress σ according to Stoney's equation:

$$\sigma_f = \frac{E_s t_s \delta}{3(1-\nu_s) t_f L^2}, \tag{5.12}$$

where E_s is the Young's modulus, t_s the thickness and ν_s the Poisson ratio of the substrate, respectively, t_f is the thickness of the film, L is the length and δ the

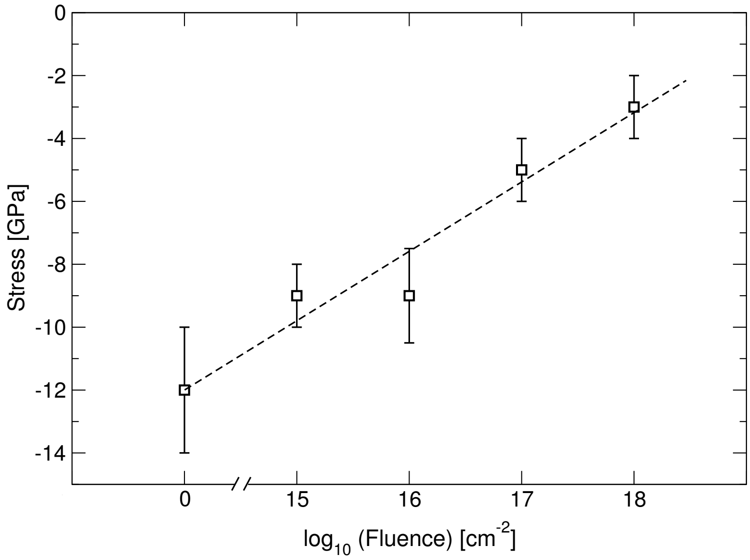

Figure 5.12: Compressive stress of a c-BN film, which was irradiated with 10 keV nitrogen ions at room temperature, as a function of ion fluence. The measurements were performed optically by measuring the bending of a small cantilever. No transition back to t-BN had been occured up to a fluence of 10^{17} cm^{-2} (after ref. [Eyh04]).

bending of the cantilever. The film was then subsequently irradiated with ^{14}N^{+} ions at room temperature with $E_{ion} = 10$ keV and fluences from 10^{15} to 10^{18} cm^{-2} and the stress was again measured after each irradiation step. The deposited charge of $Q = 0.35$ C ensured that the unstable t-BN/c-BN interface had not been irradiated. For the silicon substrate, a Young's modulus $E_s = 165$ GPa and a Poisson ratio $\nu_s = 0.2$ have been used for the calculations [Dol96, Hes96, Gan96, Kim96, Bhu97]. The obtained values σ are plotted in figure 5.12 as a function of ion fluence. The as-deposited sample shows a comparatively high stress of $\sigma = -12(2)$ GPa, which is in good agreement with the data published by other groups (see e.g. ref. [Mir97a] for an extensive review). With increasing ion fluence the stress decreases gradually to $-5(1)$ GPa after irradiation with 1×10^{17} cm^{-2}. After 1×10^{18} cm^{-2}, a value of $\sigma = -3(1)$ GPa has been measured, however, this value should be taken with care, since a significant decrease of film thickness had been occured due to sputter effects. Nevertheless, the study shows that ion irradiation allows for a significant reduction of compressive stress due to the high stability of c-BN films against ion bombardment.

5.5 Summary

It has been shown that c-BN films are extremely stable against ion bombardment. Irradiation with 1×10^{17} N^+/cm^2 and 1×10^{16} Ar^+/cm^2, respectively, has led to no significant transformation of c-BN into sp^2-bonded material. However, the crystalline quality seems to have deteriorated upon ion bombardment, presumably due to an increased amount of defects created within the film. The t-BN/c-BN boundary was found to be unstable, and irradiation of this interface induces a c-BN-to-t-BN transformation already at a fluence of about 1×10^{15} cm^{-2}, which corresponds to an accumulated defect concentration of about 1 dpa. If bombardment of the interface is avoided, ion irradiation offers the possibility of significantly decreasing the compressive stress within the film without destroying the cubic phase.

An interesting procedure for the growth of low-stress c-BN films was developed by Abendroth *et al.* based on the published results on the t-BN/c-BN interface instability [Abe04]. The authors used dynamic *in-situ* stress measurement by means of cantilever bending during magnetron sputter deposition of c-BN films. This way, the point of c-BN nucleation could be measured instantly. Figure 5.13a shows the force per unit width (FPUW) as a function of film thickness recorded during deposition of a BN film. The compressive stress at a certain film thickness is given by the slope of the lines; the onset of c-BN nucleation is accompanied by a sharp increase of compressive stress at a thickness of about 30 nm. The stress of the film then saturates at -10.7 GPa, which is good agreement with the results displayed in figure 5.12.

In order to reduce the stress, the growing film was simultaneously bombarded with 8 keV Ar^+ ions, which was accomplished by using short (2 μs) high-voltage pulses. The results are shown in figure 5.13b. After c-BN nucleation at a film thickness of about 50 nm, the stress level increases dramatically up to -8.7 GPa. However, at a thickness of 75 nm, the high-voltage pulses were switched on and the film was bombarded with 8 keV Ar ions. A dramatic stress decrease is visible, and the film grew up to a thickness of about 170 nm with a stress of only -1.1 GPa. It has to be mentioned, though, that the irradiations were carried out at elevated temperatures ($T_S = 350$ °C), and are thus not directly comparable to the experiments

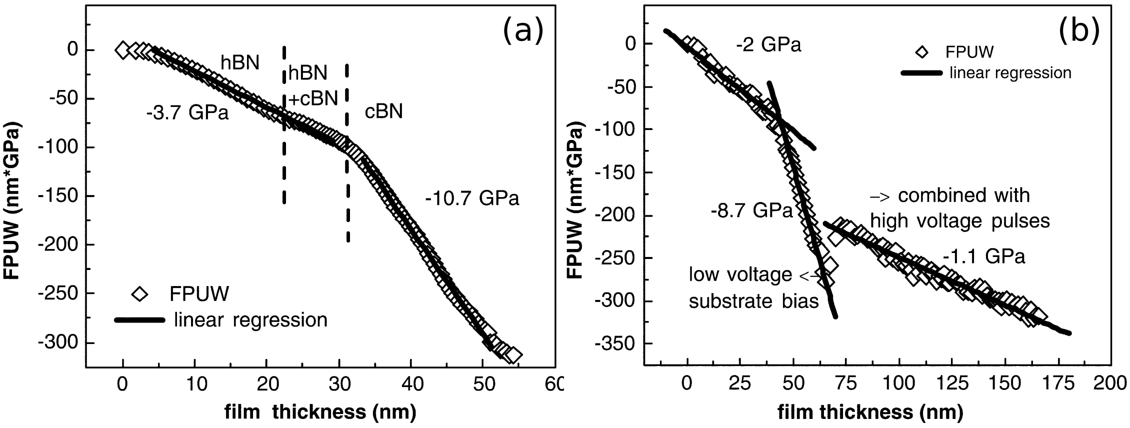

Figure 5.13: (a) Force per unit width (FPUW) as function of film thickness recorded during the deposition of an h-BN/c-BN layer sequence without stress relaxation. The open squares represent the FPUW data points and the solid lines mark linear regressions; the slope of the lines gives the instantaneous stress at that film thickness. (b) FPUW recorded during deposition including high voltage pulses for stress relaxation (taken from ref. [Abe04]).

described in section 5.2.2. As the phase formation has been found to be influenced by the temperature at high ion energies (see section 3.3), it is conceivable that elevated substrate temperatures would probably increase the c-BN phase stability even more. Hence, the use of higher temperatures may help to suppress the observed deterioration of c-BN crystalline quality upon ion irradiation.

Chapter 6

Summary and conclusion

The extensive research on cubic boron nitride thin films over the last decade may have eventually led to the circumvention of several problems that still prevent the use of c-BN as a material for tribologic or electronic applications. Worth mentioning in this respect are the successful hetero-epitaxial growth of c-BN on diamond and the deposition of thick and adherent c-BN films by means of biased fluorine CVD methods. Nevertheless, the fundamental processes leading to c-BN formation are still not resolved, especially the role of the ion energy and the influence of the ion bombardment in general. This is probably most obvious when examining the models that have been developed in order to describe the growth of thin films by ion beam deposition. Nearly every effect related to ion bombardment has been used as a basis for the one or the other model, for example sputtering (sputter model), defect and stress generation (stress models), or energy deposition and dissipation (subplantation and thermal spike models). Although each model is able to describe certain features of thin film deposition, none of them can explain all aspects of c-BN formation. The cylindrical thermal spike model is probably the most sophisticated model to date, and its predictions for the growth regime of tetrahedral amorphous carbon films are in very good agreement with the experimentally observed energy range. In the case of c-BN film growth, it can explain many of the features of a typical c-BN film, e.g. the characteristic layer sequence, the presence of an sp^2-bonded surface layer, or the nanocrystalline structure. Furthermore, the predicted lower energy threshold below which c-BN growth reverts back to t-BN growth is in very good agreement with the experiment. The model introduces the number of rearrangements occuring during a thermal spike compared to the total number of atoms within the spike volume as the key parameter n_T/n_S, which determines the resulting film structure. Only if $n_T/n_S > 1$ can each atom be rearranged at least once, and a new crystalline structure may evolve. Optimum c-BN growth conditions are predicted to be in the energy range of about 60 eV to 4 keV.

By using the mass separated ion beam deposition (MISBD) technique, the influence of the ion energy and substrate temperature on the growth of c-BN thin films was investigated in this thesis. As deposition with this method is not hindered by a resputter limit, it is the ideal tool to establish the parameter space for c-BN growth, especially for high ion energies. Boron nitride films were deposited on silicon substrates with varying ion energies between 500 eV and 43 keV and substrate temperatures ranging from room temperature to 250 °C. Nucleation of the cubic phase is most likely restricted to ion energies below about 2-3 keV, and in order to study the growth process only, high energy deposition was continued on a previously grown c-BN layer. At $T_S = 250$ °C, successful c-BN formation was confirmed with ion energies of 31 and 43 keV for $^{11}B^+$ and $^{14}N^+$ ions, respectively. This contradicts the predictions made by the cylindrical thermal spike model.

Within the energy range considered in this work, stopping of ions penetrating a target material is governed by two processes: For boron or nitrogen ions entering a c-BN target, nuclear stopping, i.e. elastic collisions between the ion and atoms in the sample, is the dominant mechanism for ion energies up to about 10 keV. Inelastic interaction between the incoming ion and the electrons in the target results in the so-called electronic stopping and becomes important at energies in excess of 10 keV. This situation is outlined in figure 6.1, which shows the nuclear and electronic stopping powers as a function of ion energy. The data has been calculated with SRIM by simulating an impact of $^{11}B^+$ ions onto a c-BN target. The region in which nuclear stopping is dominant, i.e. approximately 100 eV to 10 keV, one commonly speaks of subplantation [Hof98]. Interactions of ions with the solid can be treated within the termal spike concept in this energy range, since the energy present in form of phonon excitations (i.e. the thermal energy) is high as compared to the energy converted into electronic excitations. Above about 10 keV, however, electronic stopping becomes dominant and the influence of thermal spikes vanishes. The consequence of this is shown in figure 6.2. It displays the number of rearrangements

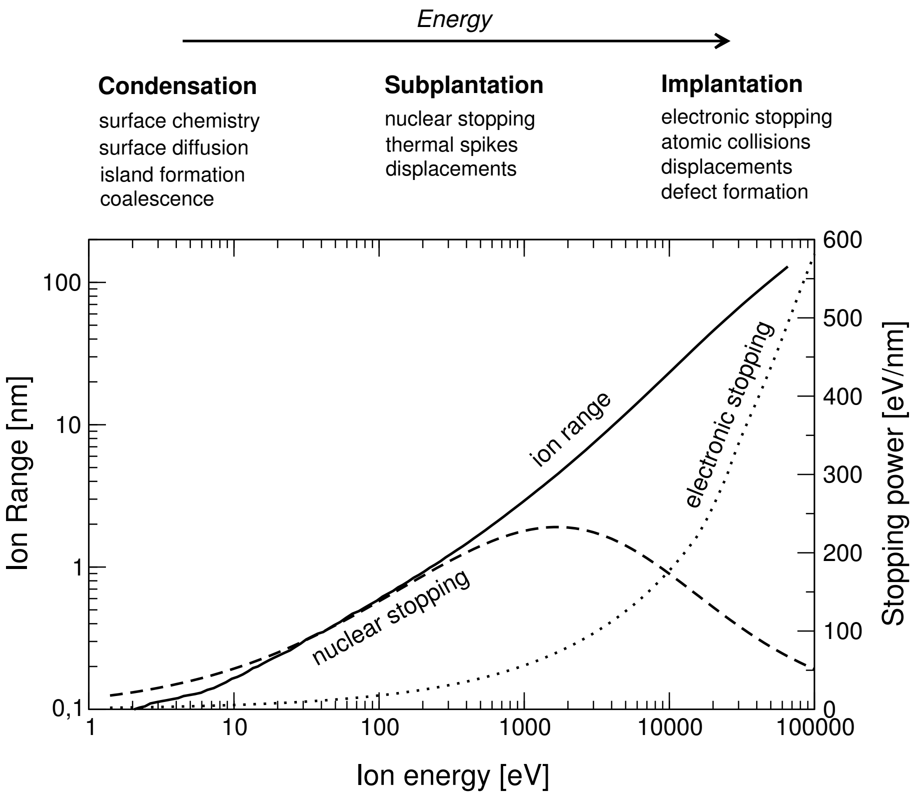

Figure 6.1: Electronic and nuclear stopping powers as a function of ion energy for an ^{11}B ion penetrating a c-BN target. The mean ion range is also displayed. All values have been calculated by SRIM (after ref. [Hof04a]).

occuring during a thermal spike (n_T) compared to the number of displacements induced by the incident ion. n_T has been calculated using equation (4.4) and the input parameters as given in ref. [Hof98]. Additional data, e.g. the mean ion range, and the number of displacements have been obtained by simulating an $^{11}B^+$ impact onto a c-BN target with SRIM. As can be seen, the number of rearrangements is in the energy range dominated by nuclear stopping about 10 times larger than the number of created displacements. Thermal spike induced rearrangements will completely override the effect of ballistic displacements and can thus be regarded as the predominant mechanism avoiding defect accumulation in this energy regime. For high ion energies, however, collision cascade effects become more important, and the number of rearrangements decreases along with the decreasing contribution of nuclear stopping to the total stopping power. Therefore, thermal spikes cannot be

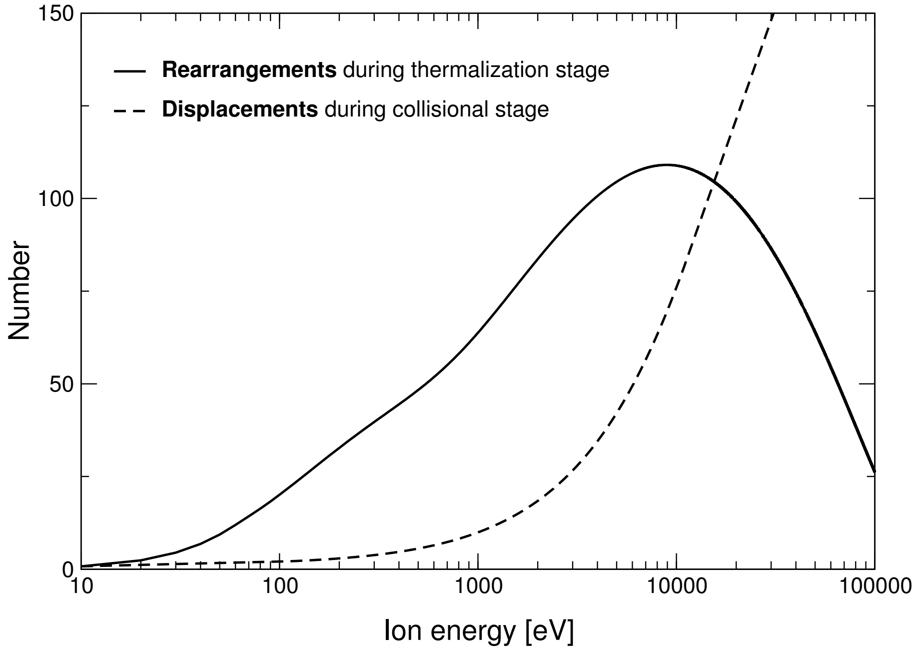

Figure 6.2: SRIM calculated displacements and replacement collisions as a function of ion energy for an ^{11}B ion penetrating a c-BN target (after ref. [Hof98]).

the predominant mechanism responsible for c-BN growth with energies exceeding about 10 keV.

Although c-BN growth was found to be possible with an ion energy of 43 keV at 250 °C, a systematic study has revealed a characteristic energy-dependent temperature threshold below which c-BN growth reverts back to t-BN growth at a given ion energy. At 5 keV for example, a substrate temperature of about 25 °C is sufficient to maintain c-BN formation, but for higher ion energies the temperature has to be increased as well. The use of 43 keV ^{14}N^{+} and 31 keV ^{11}B^{+} ions requires a substrate temperature of at least 100 °C.

^{10}B ions were implanted into a c-BN target at different substrate temperatures, and a subsequent SIMS analysis has revealed a substantial diffusion of ^{10}B atoms at elevated temperatures. SRIM simulations of the ion impact in combination with the SIMS data have shown a migration of interstitial ^{10}B atoms towards the maximum of the target vacancy profile, with a diffusion length that is approximately given by the distance between implantation and damage profile. This oberservation was used to establish a model based on an Arrhenius diffusion behavior and the assumption of a simple random walk as the dominant atomic diffusion mechanism. A diffusion constant of $D_0 \approx 1.5\times10^{-3}$ cm^2/s has been estimated, and the critical temperatures for c-BN growth were calculated by using the available SIMS data in addition to SRIM calculations. A migration energy of $W_m = 0.5(1)$ eV for interstitial boron diffusion in c-BN was found. The predictions made by the model were shown to be in good agreement with the experimental results. The dominating role of thermal spikes as the mechanism for suppression of defect accumulation is therefore superseded by temperature-driven back-diffusion and subsequent annihilation of boron and nitrogen interstitial recoils at ion energies in excess of about 5 keV.

A similar energy-temperature dependence for c-BN nucleation was found as well, and the previously assumed independence of ion energy and substrate temperature thresholds has been disproved. Instead, the temperature has to be increased for increasing ion energies in order to nucleate the cubic phase. The diffusion model developed for c-BN growth was applied to c-BN nucleation as well, and a diffusion constant and migration energy for self-diffusion in t-BN have been estimated to $D_0 \approx 1\times10^{-2}$ cm^2/s and $W_m \approx 0.9$ eV, respectively. As these values are significantly larger than for c-BN, a higher temperature at a given ion energy is required in order to nucleate c-BN as compared to its subsequent growth. Temperature-induced diffusion processes are seen responsible for annealing of radiation damage, avoiding defect accumulation and providing the boundary conditions necessary to nucleate the cubic phase.

Finally, the stability of cubic boron nitride films against ion irradiation was investigated. It was shown that a complete transformation of sp^3- into sp^2-bonded material can be induced by bombarding the t-BN/c-BN interface with ion fluences that generate an accumulated defect concentration of about 1 dpa. The cubic phase itself, however, is much more stable and is able to withstand irradiation with approximately 1×10^{16} Ar and 1×10^{17} N ions/cm^2, respectively. These fluences generate a defect concentration of about 8 and 20 dpa, respectively. A substantial release of compressive stress is observed upon ion bombardment, which, however, is accompanied by a significant decrease of grain size and overall crystalline quality.

The use of high ion energies may thus provide a way to grow thick c-BN films with relatively low compressive stress values even at low substrate temperatures. The

FTIR results described in section 3.2 already show a decrease of compressive stress with increasing ion energy, but it would be interesting to examine this effect more quantitavely, e.g. by means of cantilever bending. This approach could help to overcome the stress-related limitation of c-BN films to thicknesses of the order of 100-200 nm. Although thick and almost stress-free c-BN films can be prepared by using biased fluorine-assisted CVD methods, this process requires the use of very high temperatures, as does the deposition of hetero-epitaxial c-BN films on diamond substrates. However, in view of applications, a further reduction of the temperature is desirable. For the case of c-BN growth on diamond, the temperature is most likely related to the preservation of the diamond surface but not to the c-BN growth process itself; hence, one may be able to prepare c-BN films even at low temperatures directly on other suitable substrate materials that do not amorphize under ion bombardment. Aluminum nitride was found to fulfill the necessary requirements, but experiments proving that hetero-epitaxial growth is indeed possible at room temperature have yet to be performed.

List of Figures

References

[Abe04] B. Abendroth, R. Gago, A. Kolitsch, and W. Möller, *Thin Solid Films* **447**, 131 (2004).

[Alb97a] K. Albe, *Phys. Rev. B* **55**, 6203 (1997).

[Alb97b] K. Albe, W. Möller, and K.H. Heinig, *Rad. Eff. Def. Solids* **141**, 85 (1997).

[Alb98] K. Albe, Dissertation, Forschungszentrum Rossendorf (1998).

[All98] L. Allers, A.T. Collins, and J. Hiscock, *Diamond Relat. Mater.* **7**, 228 (1998).

[Ama97] S. Amagi, D. Takahashi, and T. Yoshida, *Appl. Phys. Lett.* **70**, 946 (1997).

[Bar96] A. Bartl, S. Bohr, R. Haubner, and B. Lux, *Int. J. of Refractory Metals and Hard Materials* **14**, 145 (1996).

[Bhu97] B. Bhushan and X. Li, *J. Mater. Res.* **12(1)**, 54 (1997).

[Boh95] S. Bohr, R. Haubner, and B. Lux, *Diamond Relat. Mater.* **4**, 714 (1995).

[Bou92] D. Bouchier and W. Möller, *Surf. Coat. Technol.* **51**, 190 (1992).

[Bou94] D. Bouchier, G. Sené, M.A. Djouadi, and P. Möller, *Nucl. Instrum. Meth. B* **89**, 369 (1994).

[Boy98] K.J. Boyd, D. Marton, J.W. Rabalais, S. Uhlmann, and Th. Frauenheim, *J. Vac. Sci. Technol. A* **16**, 444 (1998).

[Boy99] H.-G. Boyen, P. Widmeyer, D. Schwertberger, N. Deyneka, and P. Ziemann, *Appl. Phys. Lett.* **76**, 709 (1999).

[Bun55] F.P. Bundy, H.T. Hall, H.M. Strong, and R.H. Wentorf, *Nature* **176**, 51 (1955).

[Bun63] F.P. Bundy and R.H. Wentorf, *J. Chem. Phys.* **38**, 1144 (1963).

[Car97] G.F. Cardinale, D.L. Medlin, P.B. Mirkarimi, K.F. McCarty, and D.G. Howitt, *J. Vac. Sci. Technol. A* **15**, 196 (1997).

[Chr74] R.M. Chrenko, *Solid State Commun.* **14**, 511 (1974).

[Chr87] N.E. Christensen, S. Satpathy, and Z. Pawlowska, *Phys. Rev. B* **36**, 1032 (1987).

[Coh85] M.L. Cohen, *Phys. Rev. B* **32**, 7988 (1985).

[Coh94] M.L. Cohen, *Solid State Commun.* **45**, 45 (1994).

[Coh96] M.L. Cohen, *Mater. Sci. Eng. A* **209**, 1 (1996).

[Cor75] F.R. Corrigan and F.P. Bundy, *J. Chem. Phys.* **63**, 3812 (1975).

[Cot95] D.R. Cote, S.V. Nguyen, W.J. Cote, S.L. Pennington, A.K. Stamper, and D.V. Podlesnik, *IBM J. Res. Dev.* **39**, 437 (1995).

[Dav76] L.E. Davis, N.C. MacDonald, P.W. Palmberg, G.E. Riach, and R.E. Weber, *Handbook of Auger Electron Spectroscopy*, Physical Electronics Industries, Inc. (1976).

[Dav93] C.A. Davis, *Thin Solid Films* **226**, 30 (1993).

[Dem95] G. Demazeau, V. Gonnet, V. Solozhenko, B. Tanguy, and H. Montigaud, *C.R. Acad. Sci. Paris* **320, Serie 2**, 419 (1995).

[Des97] R.M. Desrosiers, D.W. Greve, and A.J. Gellman, *Mater. Sci. Eng. B* **46**, 84 (1997).

[Dey03] N. Deyneka, X.W. Zhang, H.-G. Boyen, P. Ziemann, W. Fukarek, O. Kruse, and W. Möller, *Diamond Relat. Mater.* **12**, 37 (2003).

[Dey04] N. Deyneka, X.W. Zhang, H.-G. Boyen, P. Ziemann, and F. Banhart, *Diamond Relat. Mater.* **13**, 473 (2004).

[Dol96] J. Dolbow and M. Gosz, *Mechanics of Mater.* **23**, 311 (1996).

[Don98] W. Donner, H. Dosch, S. Ulrich, H. Ehrhardt, and D. Abernathy, *Appl. Phys. Lett.* **73**, 777 (1998).

[Ere95] M.I. Eremets, M. Gauthier, A. Polian, J.C. Chervin, J.M. Besson, G.A. Dubitskii, and Ye.Ye. Semenova, *Phys. Rev. B* **52**, 8854 (1995).

[Eyh01] S. Eyhusen, diploma thesis, University of Göttingen (2001).

[Eyh03] S. Eyhusen, I. Gerhards, H. Hofsäss, C. Ronning, M. Blomenhofer, J. Zweck, and M. Seibt, *Diamond Relat. Mater.* **12**, 1877 (2003).

[Eyh04] S. Eyhusen, H. Hofsäss, and C. Ronning, *Thin Solid Films* **447-448**, 125 (2004).

[Eyh05] S. Eyhusen, C. Ronning, and H. Hofsäss, *Phys. Rev. B* **72**, 054126 (2005).

[Fah95] S. Fahy, *Phys. Rev. B* **51**, 12873 (1995).

[Fah96] S. Fahy, *Phys. Rev. B* **53**, 11887 (E) (1996).

[Fah97] S. Fahy, C.A. Taylor II, and R. Clarke, *Phys. Rev. B* **56**, 12573 (1997).

[Fel97] H. Feldermann, Diploma thesis, University of Konstanz (1997).

[Fel98] H. Feldermann, M. Sebastian, R. Merk, M. Restle, C. Ronning, and H. Hofsäss, *in Hard coatings based on carbides, borides and nitrides*, A. Kumar, Y.-W. Chung, R. Chia (eds.), TMS Conference Proceedings (1998), p. 143.

[Fel99] H. Feldermann, R. Merk, H. Hofsäss, C. Ronning, and T. Zheleva, *Appl. Phys. Lett.* **74**, 1552 (1999).

[Fel01] H. Feldermann, C. Ronning, H. Hofsäss, Y.L. Huang, and M. Seibt, *J. Appl. Phys.* **90**, 3248 (2001).

[Fel02] H. Feldermann, Dissertation, University of Göttingen (2002).

[Fit00] C. Fitz, W. Fukarek, A. Kolitsch, and W. Möller, *Surf. Coat. Technol.* **128-129**, 292 (2000).

[Fit01] C. Fitz, Dissertation, Forschungszentrum Rossendorf (2001).

[Fri93] T.A. Friedmann, L.J. Bernadez, K.F. McCarty, E.J. Klaus, D.K. Ottesen, H.A. Johnsen, and W.M. Clift, *Appl. Phys. Lett.* **63**, 1342 (1993).

[Fri94] T.A. Friedmann, P.B. Mirkarimi, D.L. Medlin, K.F. McCarty, E.J. Klaus, D. Boehme, H.A. Johnsen, M.J. Mills, and D.K. Ottesen, *J. Appl. Phys.* **76**, 3088 (1994).

[Fur94] J. Furthmüller, J. Hafner, and G. Kresse, *Phys. Rev. B* **50**, 15606 (1994).

[Gan94] R. Ganzetti and W. Gissler, *Mater. Manuf. Processes* **9**, 507 (1994).

[Gan96] L. Gan, B. Ben-Nissan, and A. Ben-David, *Thin Solid Films* **290**, 362 (1996).

[Gei66] R. Geick, C.H. Perry, and G. Rupprecht, *Phys. Rev.* **146**, 543 (1966).

[Gie67] P.J. Gielisse, S.S. Mitra, J.N. Plendl, R.D. Griffis, L.C. Mansur, R. Marshall, and E.A. Pascoe, *Phys. Rev.* **155**, 1039 (1967).

[Hah97] J. Hahn, F. Richter, R. Pintaske, M. Röder, E. Schneider, and T. Welzel, *Surf. Coat. Technol.* **92**, 129 (1997).

[Heb00] M. Hebbache, *Solid State Commun.* **113**, 427 (2000).

[Her95] R.W. Hertzberg, *"Deformation and fracture mechanics of engineering materials"*, Wiley, New York, 4th edn. (1995).

[Hes96] P. Hess, *Appl. Surf. Science* **106**, 429 (1996).

[Hof94] H. Hofsäss, H. Binder, T. Klumpp, and E. Recknagel, *Diamond Relat. Mater.* **3**, 137 (1994).

[Hof95] H. Hofsäss, C. Ronning, U. Griesmeier, M. Gross, S. Reinke, and M. Kuhr, *Appl. Phys. Lett.* **67**, 46 (1995).

[Hof96] H. Hofsäss and C. Ronning, *in 2nd Internat. Conf. Beam Processing of Advanced Materials*, J. Singh, S.M. Copley, and J. Mazumder (eds.), ASM Int., Materials Park (1996), p. 29.

[Hof97] H. Hofsäss, H. Feldermann, M. Sebastian, and C. Ronning, *Phys. Rev. B* **55**, 13230 (1997).

[Hof98] H. Hofsäss, H. Feldermann, R. Merk, M. Sebastian, and C. Ronning, *Appl. Phys. A* **66**, 153 (1998).

[Hof02] H. Hofsäss, H. Feldermann, S. Eyhusen, and C. Ronning, *Phys. Rev. B* **65**, 115410 (2002).

[Hof04a] H. Hofsäss, *AIP Conf. Proc.* **740**, 101 (2004).

[Hof04b] H. Hofsäss, S. Eyhusen, and C. Ronning, *Diamond Relat. Mater.* **13**, 1103 (2004).

[Ich94] T. Ichiki, T. Momose, and T. Yoshida, *J. Appl. Phys.* **75**, 1330 (1994).

[Ina87] K. Inagawa, K. Watanabe, H. Ohsone, K. Saitoh, and A. Itoh, *J. Vac. Sci. Technol. A* **5**, 2696 (1987).

[Kal98] W. Kalss, R. Haubner, and B. Lux, *Diamond Relat. Mater.* **7**, 369 (1998).

[Kas88] S.R. Kasi, H. Kang, and J.W. Rabalais, *J. Chem. Phys.* **88**, 5914 (1988).

[Ker99] G. Kern, G. Kresse, and J. Hafner, *Phys. Rev. B* **59**, 8551 (1999).

[Kes87] G. Kessler, K.D. Bauer, W. Pompe, and J.J. Scheibe, *Thin Solid Films* **147**, L45 (1987).

[Kes92] D.J. Kester and R. Messier, *J. Appl. Phys.* **72**, 504 (1992).

[Kes93] D.J. Kester, K.S. Ailey, R.F. Davis, and K.L. More, *J. Mater. Res.* **8**, 1213 (1993).

[Kes94a] D.J. Kester, K.S. Ailey, and R.F. Davis, *Diamond Relat. Mater.* **3**, 332 (1994).

[Kes94b] D.J. Kester, K.S. Ailey, D.J. Lichtenwalner, and R.F. Davis, *J. Vac. Sci. Technol. A* **12**, 3074 (1994).

[Khi01] S. Khizroev and D. Litvinov, *Appl. Phys. Lett.* **79**, 353 (2001).

[Kim96] Min Tae Kim, *Thin Solid Films* **283**, 12 (1996).

[Kim99] K. Kimura, A. Agarwal, H. Toyofuku, K. Nakajima, and H.J. Gossmann, *Nucl. Instrum. Meth. B* **252**, 284 (1999).

[Kle99] A. Klett, R. Freudenstein, M.F. Plass, and W. Kulisch, *Surf. Coat. Technol.* **116-119**, 86 (1999).

[Klo98] T. Klotzbücher and E.W. Kreutz, *Diamond Relat. Mater.* **7**, 1219 (1998).

[Kon99] I. Konyashin, F. Aldinger, V. Babaev, V. Khvostov, M. Guseva, A. Bregadze, K.-M. Baumgärtner, and E. Räuchle, *Thin Solid Films* **355-356**, 96 (1999).

[Kuh95] M. Kuhr, R. Freudenstein, S. Reinke, and W. Kulisch, *in Diamond Materials IV*, P. Ravi, J. Dismukes (eds.), The Electrochemical Society Proc, 95-4, Pennington (1995).

[Kul00] W. Kulisch, *Phys. Stat. Sol. (a)* **177**, 63 (2000).

[Kul03] W. Kulisch and S. Ulrich, *Thin Solid Films* **423**, 183 (2003).

[Kur96] A.V. Kurdyumov, V.F. Britun, and I.A. Petrusha, *Diamond Relat. Mater.* **5**, 1229 (1996).

[Li93] Z. Li, L. Wang, T. Suzuki, A. Argoitia, P. Pirouz, and J.C. Angus, *J. Appl. Phys.* **73**, 711 (1993).

[Lif89] Y. Lifshitz, S.R. Kasi, and J.W. Rabalais, *Phys. Rev. Lett.* **62**, 1290 (1989).

[Lif90] Y. Lifshitz, S.R. Kasi, and J.W. Rabalais, *Phys. Rev. B* **41**, 10468 (1990).

[Lin90] W.L. Lin, Z. Xia, Y.L. Liu, and Y.C. Fen, *Mater. Sci. Eng. B* **7**, 107 (1990).

[Lit97] D. Litvinov and R. Clarke, *Appl. Phys. Lett.* **71**, 1969 (1997).

[Lit99] D. Litvinov and R. Clarke, *Appl. Phys. Lett.* **74**, 955 (1999).

[Liu89] A.Y. Liu and M.L. Cohen, *Science* **245**, 841 (1989).

[Liu95] J. Liu, Y.K. Vohra, J.T. Tarvin, and S.S. Vagarali, *Phys. Rev. B* **51**, 8591 (1995).

[Lu94] Ming Lu, A. Bousetta, R. Sukach, A. Bensaoula, K. Walters, K. Eipers-Smith, and A. Schultz, *Appl. Phys. Lett.* **64**, 1514 (1994).

[Lue95] H. Luethje, K. Bewilogua, S. Daaud, M. Johansson, and L. Hultman, *Thin Solid Films* **257**, 40 (1995).

[Lux99] B. Lux, W. Kalss, R. Haubner, and T. Taniguchi, *Diamond Relat. Mater.* **8**, 415 (1999).

[Mad91] O. Madelung and R. Poerschke (eds.), *Data in Science and Technology, Semiconductors, Group IV elements and III-V compounds*, Springer, Berlin (1991), p. 5-10.

[Mar98] D. Marton, K.J. Boyd, J.W. Rabalais, and Y. Lifshitz, *J. Vac. Sci. Technol. A* **16**, 455 (1998).

[Mat00] S. Matsumoto and W. Zhang, *Jpn. J. Appl. Phys.* **39**, 442 (2000).

[Mat01] S. Matsumoto and W.J. Zhang, *Diamond Relat. Mater.* **10**, 1868 (2001).

[McC96] K.F. McCarty, P.B. Mirkarimi, D.L. Medlin, and T.A. Friedmann, *Diamond Relat. Mater.* **5**, 1519 (1996).

[McC97] K.F. McCarty and D.L. Medlin, *Diamond Relat. Mater.* **6**, 1219 (1997).

[McK91] D.R. McKenzie, D. Muller, and B.A. Pailthorpe, *Phys. Rev. Lett.* **67**, 773 (1991).

[McK93] D.R. McKenzie, W.D. McFall, W.G. Sainty, C.A. Davis, and R.E. Collins, *Diamond Relat. Mater.* **2**, 970 (1993).

[McK95] D.R. McKenzie, W.D. McFall, H. Smith, B. Higgins, R.W. Boswell, A. Durandet, B.W. James, and I.S. Falconer, *Nucl. Instrum. Meth. B* **106**, 90 (1995).

[McK96] D.R. McKenzie, W.D. McFall, S. Reisch, B.W. James, I.S. Falconer, R.W. Boswell, H. Persing, A.J. Perry, and A. Durandet, *Surf. Coat. Technol.* **78**, 255 (1996).

[Med94] D.L. Medlin, T.A. Friedmann, P.B. Mirkarimi, P. Rez, M.J. Mills, and K.F. McCarty, *J. Appl. Phys.* **76**, 295 (1994).

[Med96] D.L. Medlin, T.A. Friedmann, P.B. Mirkarimi, G.F. Cardinale, and K.F. McCarty, *J. Appl. Phys.* **79**, 3567 (1996).

[Mir94] P.B. Mirkarimi, K.F. McCarty, D.L. Medlin, W.G. Wolfer, T.A. Friedmann, E.J. Klaus, G.F. Cardinale, and D.G. Howitt, *J. Mater. Res.* **9**, 2925 (1994).

[Mir95] P.B. Mirkarimi, D.L. Medlin, K.F. McCarty, and J.C. Barbour, *Appl. Phys. Lett.* **66**, 2813 (1995).

[Mir96] P.B. Mirkarimi, K.F. McCarty, G.F. Cardinale, D.L. Medlin, D.K. Ottesen, and H.A. Johnsen, *J. Vac. Sci. Technol. A* **14**, 251 (1996).

[Mir97a] P.B. Mirkarimi, K.F. McCarty, and D.L. Medlin, *Mater. Sci. Eng.* **R 21**, 47 (1997).

[Mir97b] P.B. Mirkarimi, D.L. Medlin, K.F. McCarty, D.C. Dibble, W.M. Clift, J.A. Knapp, and J.C. Barbour, *J. Appl. Phys.* **82**, 1617 (1997).

[Mis87] O. Mishima, J. Tanaka, S. Yamada, and O. Fukunaga, *Science* **238**, 181 (1987).

[Mis88] O. Mishima, K. Era, J. Tanaka, and S. Yamaoka, *Appl. Phys. Lett.* **53**, 962 (1988).

[Mis90] O. Mishima, *in: Synthesis and Properties of Boron Nitride*, J.J. Pouch, S.A. Alterovitz (eds.), Materials Science Forum, Vol. 54/55, Trans Tech Publications, Brookfield (1990), p. 313.

[Mur90] M. Murakawa and S. Watanabe, *Surf. Coat. Technol.* **43**, 1 (1990).

[Nag74] H.M. Naguib and R. Kelly, *Radiat. Eff.* **25**, 1 (1974).

[Nas79] K. Nassau and J. Nassau, *J. Cryst. Growth* **46**, 157 (1979).

[Nie00] W. Niessner, Dissertation, University of Giessen (2000).

[Nie01] E. Niehuis and T. Grehl, *in: ToF-SIMS, Surface Analysis by Mass Spectrometry*, edited by J.C. Vickerman and D. Briggs, IM Publications and SurfaceSpectra Limited (2001), p. 759.

[Ore01] W. Orellana and H. Chacham, *Phys. Rev. B* **63**, 125205 (2001).

[Pai93] M.J. Paisley, L.P. Bourget, and R.F. Davis, *Thin Solid Films* **235**, 30 (1993).

[Par97] K.S. Park, D.Y. Lee, K.J. Kim, and D.W. Moon, *Appl. Phys. Lett.* **70**, 315 (1997).

[Qui96] H. Quintel, K. Baruth-Ram, H. Hofsäss, M. Restle, and C. Ronning, *Nucl. Instrum. Meth. B* **118**, 72 (1996).

[Rei94] S. Reinke, M. Kuhr, and W. Kulisch, *Diamond Relat. Mater.* **3**, 341 (1994).

[Rei95] S. Reinke, M. Kuhr, W. Kulisch, and R. Kassing, *Diamond Relat. Mater.* **4**, 272 (1995).

[Rei96a] P. Reinke, G. Francz, P. Oelhafen, and J. Ullmann, *Phys. Rev. B* **54**, 7067 (1996).

[Rei96b] S. Reinke, M. Kuhr, and W. Kulisch, *Diamond Relat. Mater.* **5**, 508 (1996).

[Rei97] S. Reinke and W. Kulisch, *Surf. Coat. Technol.* **97**, 23 (1997).

[Rob93] J. Robertson, *Diamond Relat. Mater.* **2**, 984 (1993).

[Rob94] J. Robertson, *Diamond Relat. Mater.* **3**, 361 (1994).

[Rob96] J. Robertson, *Diamond Relat. Mater.* **5**, 519 (1996).

[Ron97a] C. Ronning, E. Dreher, H. Feldermann, M. Gross, M. Sebastian, and H. Hofsäss, *Diamond Relat. Mater.* **6**, 1129 (1997).

[Ron97b] C. Ronning, E. Dreher, J.-U. Thiele, P. Oelhafen, and H. Hofsäss, *Diamond Relat. Mater.* **6**, 830 (1997).

[Ron98] C. Ronning, H. Feldermann, R. Merk, H. Hofsäss, P. Reinke, and J.-U. Thiele, *Phys. Rev. B* **58**, 2207 (1998).

[Sac97] H. Sachdev, R. Haubner, H. Nöth, and B. Lux, *Diamond Relat. Mater.* **6**, 286 (1997).

[San83] J.A. Sanjurjo, E. López-Cruz, P. Vogl, and M. Cardona, *Phys. Rev. B* **28**, 4579 (1983).

[Sch96] A. Schütze, K. Bewilogua, H. Lüthje, and S. Kouptsidis, *Diamond Relat. Mater.* **5**, 1130 (1996).

[Sch02] P. Scheible, Dissertation, University of Stuttgart (2002).

[Sei54] F. Seitz and J.S. Koehler, *in Progress in Solid State Physics*, Academic Press, New York (1954), vol. 2, p. 30.

[Sei56] F. Seitz and J.S. Koehler, *Solid State Phys.* **2**, 305 (1956).

[Sht00] D.V. Shtansky, O. Tsuda, Y. Ikuhara, and T. Yoshida, *Acta mater.* **48**, 3745 (2000).

[Sin95] B.P. Singh, G. Nover, and G. Will, *J. Cryst. Growth* **152**, 143 (1995).

[Sol88] V.L. Solozhenko, *Dok. Phys. Chem.* **301**, 592 (1988).

[Sol93] V.L. Solozhenko, *Thermochim. Acta* **218**, 221 (1993).

[Sol94] V.L. Solozhenko, *Diamond Relat. Mater.* **4**, 1 (1994).

[Sol00] V.L. Solozhenko, D. Andrault, G. Fiquet, M. Mezouar, and D.C. Rubie, *Appl. Phys. Lett.* **78**, 1385 (2000).

[Sri90] G.P. Srivastava, *The Physics of Phonons*, Adam Hilger, Bristol (1990).

[Sta99] D. Starikov, N. Badi, I. Berishev, N. Medelci, O. Kameli, M. Sayhi, V. Zomorrodian, and A. Bensaoula, *J. Vac. Sci. Technol. A* **17**, 1235 (1999).

[Tan92] N. Tanabe, T. Hayashi, and M. Iwaki, *Diamond Relat. Mater.* **1**, 151 (1992).

[Tan01] T. Taniguchi and S. Yamaoka, *J. Cryst. Growth* **222**, 549 (2001).

[Tan04] T. Taniguchi, K. Watanabe, and S. Koizumi, *Phys. Stat. Sol. (a)* **201**, 2573 (2004).

[Tar88] J.D. Targove and H.A. Macleod, *Appl. Opt.* **27**, 3779 (1988).

[Teg79] E. Tegeler, N. Kosuch, G. Wiech, and A. Fässler, *Phys. Stat. Sol. (b)* **91**, 223 (1979).

[Tet98] D.M. Teter, *MRS Bull.* **23**, 22 (1998).

[Tho63] J. Thomas, N.E. Weston, and T.E. O'Connor, *J. Am. Chem. Soc.* **84**, 4619 (1963).

[Tok85] H. Tokutaka, K.N. Nishimori, and H. Hayashi, *Surf. Sci.* **149**, 349 (1985).

[Ull98] J. Ullmann, J.E.E. Baglin, and A.J. Kellock, *J. Appl. Phys.* **83**, 2980 (1998).

[Ull99] J. Ullmann, A.J. Kellock, and J.E.E. Baglin, *Thin Solid Films* **341**, 238 (1999).

[Ulr96] S. Ulrich, J. Schwan, W. Donner, and H. Ehrhardt, *Diamond Relat. Mater.* **5**, 548 (1996).

[Vel91] L. Vel, G. Demazeau, and J. Etourneau, *Mater. Sci. Eng. B* **10**, 149 (1991).

[Vep99] S. Veprek, *J. Vac. Sci. Technol. A* **17**, 2401 (1999).

[Vin76] G.H. Vineyard, *Radiat. Eff.* **29**, 245 (1976).

[Wah97] U. Wahl and ISOLDE Collaboration, *Phys. Reports* **280**, 145 (1997).

[Wat95] S. Watanabe, S. Miyake, W. Zhou, Y. Ikuhara, T. Suzuki, and M. Murakawa, *Appl. Phys. Lett.* **66**, 1478 (1995).

[Wei81] C. Weissmantel, *J. Vac. Sci. Technol. A* **18**, 179 (1981).

[Wen57] R.H. Wentorf, *J. Chem. Phys.* **26**, 956 (1957).

[Wen59] R.H. Wentorf, *J. Phys. Chem.* **63**, 1934 (1959).

[Wen61a] R.H. Wentorf, *J. Chem. Phys.* **34**, 809 (1961).

[Wen61b] R.H. Wentorf, *Chem. Eng.* **68**, 177 (1961).

[Wen62] R.H. Wentorf, *J. Chem. Phys.* **36**, 1990 (1962).

[Wid97] P. Widmeyer, P. Ziemann, S. Ulrich, and H. Ehrhardt, *Diamond Relat. Mater.* **6**, 621 (1997).

[Wid98] P. Widmayer, P. Ziemann, and H.-G. Boyen, *Diamond Relat. Mater.* **7**, 385 (1998).

[Wid99] P. Widmayer, H.-G. Boyen, P. Ziemann, P. Reinke, and P. Oelhafen, *Phys. Rev. B* **59**, 5233 (1999).

[Wil00] G. Will, G. Nover, and J. von der Gönna, *J. Solid State Chem.* **154**, 280 (2000).

[Win87] H. Windischmann, *J. Appl. Phys.* **62**, 1800 (1987).

[Win91] H. Windischmann, *J. Vac. Sci. Technol. A* **9**, 2431 (1991).

[Xu91] Y.-N. Xu and W.Y. Ching, *Phys. Rev. B* **44**, 7787 (1991).

[Yan95] P.X. Yan, S.Z. Yang, B. Li, and X.S. Chen, *J. Cryst. Growth* **148**, 232 (1995).

[Yan03] H. Yang, C. Iwamoto, and T. Yoshida, *J. Appl. Phys.* **94**, 1248 (2003).

[Ye98] J. Ye, U. Rothhaar, and H. Oechsner, *Surf. Coat. Technol.* **105**, 159 (1998).

[Ye00] J. Ye, Dissertation, University of Kaiserslautern (2000).

[Yos96] T. Yoshida, *Diamond Relat. Mater.* **5**, 501 (1996).

[YT02] Y. Yamada-Takamura and T. Yoshida, *J. Vac. Sci. Technol. B* **20**, 936 (2002).

[Zha00] W.J. Zhang and S. Matsumoto, *Chem. Phys. Lett.* **330**, 243 (2000).

[Zha03] X.W. Zhang, H.-G. Boyen, N. Deyneka, P. Ziemann, F. Banhart, and M. Schreck, *Nat. Mater.* **2**, 312 (2003).

[Zha04a] W.J. Zhang, I. Bello, Y. Lifshitz, K.M. Chan, Y. Wu, C.Y. Chan, X.M. Meng, and S.T. Lee, *Appl. Phys. Lett.* **85**, 1344 (2004).

[Zha04b] X.W. Zhang, H.-G. Boyen, P. Ziemann, M. Ozawa, F. Banhart, and M. Schreck, *Diamond Relat. Mater.* **13**, 1144 (2004).

[Zha05] X.W. Zhang, H. Yin, H.-G. Boyen, P. Ziemann, and M. Ozawa, *Diamond Relat. Mater.* **14**, 1482 (2005).

[Zho95a] W.-L. Zhou, Y. Ikuhara, M. Murakawa, S. Watanabe, and T. Suzuki, *Appl. Phys. Lett.* **66**, 2490 (1995).

[Zho95b] W.-L. Zhou, Y. Ikuhara, and T. Suzuki, *Appl. Phys. Lett.* **67**, 3551 (1995).

[Zie99] J.F. Ziegler, J.P. Biersack, and U. Littmark, *The Stopping and Range of Ions in Solids*, Pergamon Press, New York (1999), see also: http://www.srim.org.

Appendix

List of publications

Parts of this thesis have been published within the following articles:

- S. Eyhusen, C. Ronning, and H. Hofsäß, "Cubic boron nitride thin film growth by boron and nitrogen ion implantation", *Phys. Rev. B* **72**, 054126 (2005).
- H. Hofsäß, S. Eyhusen, and C. Ronning, "On the mechanisms of cubic boron nitride film growth", *Diamond Relat. Mater.* **13**, 1103 (2004).
- S. Eyhusen, H. Hofsäß, and C. Ronning, "Role of the ion energy on the growth of cubic boron nitride thin films", *Thin Solid Films* **447-448**, 125 (2004).
- S. Eyhusen, I. Gerhards, H. Hofsäß, C. Ronning, M. Blomenhofer, J. Zweck, M. Seibt, "Ion energy thresholds and stability of cubic boron nitride", *Diamond Relat. Mater.* **12**, 1877 (2003).
- H. Hofsäß, H. Feldermann, S. Eyhusen, and C. Ronning, "The fundamental role of ion bombardement for the synthesis of cubic boron nitride films", *Phys. Rev. B* **65**, 115410 (2002).

Additional publications not related to this thesis:

- C.Y. Chan, S. Eyhusen, X.M. Meng, I. Bello, S.T. Lee, C. Ronning, and H. Hofsäß, "The effect of substrate surface roughness on the nucleation of cubic boron nitride films", *Diamond Relat. Mater.*, in press.
- P. Reinke, S. Eyhusen, M. Büttner, and P. Oelhafen, "Interaction of Fe^+ with the C60 surface: A study about the feasibility of endohedral doping", *Appl. Phys. Lett.* **84**, 4373 (2004).

- S. Eyhusen, C. Ronning, and H. Hofsäß, "Phase formation of boron nitride thin films under the influence of impurity atoms", *Diamond Relat. Mater.* **12**, 1173 (2003).
- C. Ronning, D. Schwen, S. Eyhusen, U. Vetter, and H. Hofsäß, "Ion beam synthesis of boron carbide thin films", *Surf. Coat. Technol.* **158**, 382 (2002).

Danksagung

Ich möchte mich zunächst ganz herzlich bei meinem Doktorvater Herrn Prof. Hans Hofsäß für seine Unterstützung und Betreuung wärend der Promotionszeit bedanken. Ein besonderes Dankeschön dafür, daß seine Tür immer geöffnet ist und er Zeit für wissenschaftliche Diskussionen findet, obwohl das Telefon wärend dieser Zeit selten still steht. Allerdings wird es mal wieder Zeit für eine Wette... :-)

Herrn PD Dr. Christian Jooß danke ich für die spontane Bereitschaft, diese Arbeit zu begutachten.

Danke auch an Herrn PD Dr. Carsten Ronning für seine große Hilfe in technischen als auch wissenschaftlichen Fragen und ganz besonders für das Durchlesen und Korrigieren dieser Arbeit.

Daniel Schwen möchte ich danken für die Zeit, in der ich das große Glück hatte, ein Büro mit ihm teilen zu dürfen. Danke für viele Gespräche und Diskussionen, wissenschaftlich und privat, und dafür, daß er mich süchtig gemacht hat nach 24, Alias, Lost und Battlestar Galactica. You're the best roommate ever. Pitcher ?

Danke an Gregor Oehl und meinem dritten Zimmergenossen Daniel Stichtenoth, die beide sehr zu der tollen Atmosphäre beigetragen haben.

Frau Inga Gerhards, Herrn PD Dr. Michael Seibt, Frau Melanie Blomenhofer und Herrn Prof. Josef Zweck sei gedankt für die vielen Stunden der TEM-Präparation und die Untersuchungen am Elektronenmikroskop.

Danke an Herrn Dr. Ulrich Schmitt vom Institut für Physikalische Chemie für seine große Geduld und seine wiederholte Hilfe bei den FTIR-Messungen.

Herrn Dr. Peter-Joachim Wilbrandt danke ich für die SIMS-Untersuchungen und für seine Hilfe und Erklärungen bei der Auswertung der Daten.

Vielen Dank auch an Herrn Dr. Ulrich Vetter für die vielen wertvollen Tipps zum Promotionsverfahren.

Ein besonderer Dank gebührt den Werkstätten des 2. Physikalischen Institutes für die Hilfe und Freundlichkeit, stellvertretend seien hier die Werkstattleiter Herr Klaus Arndt und Herr Kurt Schemmerling genannt. Danke auch an Herrn Herwig Schultz und unsere Sekretärin Frau Christa Wohlfarth sowie an alle anderen Mitarbeiter und Mitglieder der 2. Physik, die zum Gelingen dieser Arbeit beigetragen haben.

Schließlich danke ich von ganzem Herzen meinen Eltern, meinen Großeltern und meiner ganzen Familie für die uneingeschränkte Unterstützung, die Hilfe und das Vertrauen während des gesamten Studiums.

Curriculum Vitae

Persönliche Daten:

Name	Sören Eyhusen
Geburtstag	5. März 1976
Geburtsort	Karlsruhe, Deutschland
Nationalität	Deutsch
Familienstand	Ledig

Bildungsweg:

1982–1992	Grund- und Realschule Wiesmoor
1992–1995	IGS Aurich-West, *Abitur*
1996–2001	Studium der Physik an der Universität Göttingen *Vordiplom 1998* *Diplom November 2001 ("Wachstum und Dotierung von kubischen Bornitrid-Schichten")*
2001–2005	Wissenschaftlicher Angestellter, 2. Physikalisches Institut, Universität Göttingen